

Title	Charge State of Pd Nanoparticles on Al ₂ O ₃ /NiAl(110) Surface by Atomic Force Microscopy and Kelvin Probe Force Microscopy
Author(s)	Zou, Shanrong
Citation	大阪大学, 2022, 博士論文
Version Type	VoR
URL	https://doi.org/10.18910/91781
rights	
Note	

Osaka University Knowledge Archive : OUKA

<https://ir.library.osaka-u.ac.jp/>

Osaka University

Doctoral Dissertation

Charge State of Pd Nanoparticles on Al₂O₃/NiAl(110)
Surface by Atomic Force Microscopy and Kelvin
Probe Force Microscopy

ZOU SHANRONG

January 6, 2022

Graduate School of Engineering,
Osaka University

Abstract

In heterogeneous catalysis, catalytic properties of transition metal nanoparticles on oxide film support have stimulated extensive research activities, and contribute to improving the rate of catalytic reaction essentially. A catalyst system model in well arrangement, palladium metal nanoparticles (NPs) supported on $\text{Al}_2\text{O}_3/\text{NiAl}(110)$, is necessary for understanding the CO oxidation catalytic mechanism, which had been test high catalytic activity. Non-reducible oxide-support ($\text{Al}_2\text{O}_3/\text{NiAl}(110)$) affect electronic properties by altering the chemical state of the adsorbed NPs. Dispersed NPs on support can provide or withdraw electrons from the reactant that depend on the nature of the reaction. However, issues such as the how to extract the charge of Pd NPs on $\text{Al}_2\text{O}_3/\text{NiAl}(110)$, the role of Pd NPs size and morphology in deducing the charge state, and charge transfer between reactants (CO , O_2) and Pd NPs remain fiercely debated, calling for a deep understanding experimentally and theoretically.

In my research, I focused on investigating the charge state of Pd NPs on $\text{Al}_2\text{O}_3/\text{NiAl}(110)$ on catalyzed oxidation of CO by noncontact atomic force microscopy (AFM) and Kelvin probe force microscopy (KPFM) at room temperature (RT). The KPFM detects electrostatic forces between tip and surface and compensates them by applying a dc bias voltage that is adjusted by feedback control. KPFM images could give the charge landscape of the Pd NPs on $\text{Al}_2\text{O}_3/\text{NiAl}(110)$ with high accuracy. The classical electrostatic theory is combined with KPFM to extract the charge state of the Pd NPs in this catalytic system.

Firstly, we deduced the size dependence of charge state of the Pd NPs by measuring the local contact potential difference (LCPD) of Pd NPs on the Al_2O_3 (alumina) surface through KPFM and classical electrostatic model for the spheres. The Pd NPs are negatively charged on the $\text{Al}_2\text{O}_3/\text{NiAl}(110)$ surface, which is not attainable in previous study. The charge state of Pd NPs is increased with increasing the size, and these charges are transferred from surface to Pd NPs.

Secondly, we deduced the size dependence of the charge state of the CO molecule on Pd NPs by measuring the LCPD of Pd NPs on the alumina surface through KPFM with atomic resolution. The general charge state of CO molecule on Pd NPs decreased compared with the charge state of

Pd NPs. In addition, we found that the charge state decreases on the Pd NPs site and it increases on the CO site, which could be attributed to the CO bond with Pd NPs accompanying the electron transfer from Pd NPs to the CO molecule, therefore reorganizing the local charge landscape. Furthermore, by comparing with Pd nanocluster (NC) of the line defects, we found that CO molecules are more stable on Pd NC of the terrace. And the size of Pd NCs becomes small with CO adsorption, while it becomes large due to cohesion. Combining experimental results with DFT calculations, we concluded that the adsorption sites of CO molecules on Pd NC of the terrace are preferred on top, step₁₁₀, and step₁₁₁ sites. This result revealed that the electronic and geometric properties of Pd NCs and CO molecules are expected to provide insight into the mechanism of Pd-based heterogeneous catalysis.

Thirdly, we investigated that charge state evolution of the Pd NPs is studied during exposure of molecular oxygen. We speculated that the Pd NPs could be oxidized by oxygen molecules, leading to Pd_xO_y, which shows a positive charge on the alumina surface.

Our results can provide a good starting point for understanding size sensitive for a catalytic reaction by investigating size related electronic and geometric properties of the Pd NPs or Pd NPs with CO and O₂ in the nanoscale.

Contents

Chapter 1 Introduction.....	1
1.1 Background	1
1.1.1 Catalysis.....	1
1.1.2 Modeling catalyst system.....	1
1.1.3 Research by AFM/KPFM	4
1.2 Purpose of this research	6
1.3 Thesis outline	7
Chapter 2 Principles of non-contact atomic force microscopy	9
2.1 Introduction.....	9
2.2 The interaction force between tip and sample.....	9
2.3 Principle of operation of AFM.....	12
2.3.1 Operation modes	12
2.3.2 Detection of frequency shift.....	13
2.3.3 Formalism of force.....	16
2.3.4 Stability conditions for cantilever vibration.....	18
2.4 Principle of KPFM	19
2.4.1 Work function	19
2.4.2 Contact potential difference	21
2.4.3 KPFM with voltage feedback	21
2.4.4 Minimum detectable CPD by KPFM.....	23
2.4.5 Origin of the LCPD.....	24
2.5 Conclusion.....	26
Chapter 3 Setup of room temperature UHV AFM	27
3.1 Introduction.....	27
3.2 Equipment of UHV nc-AFM	27

3.3 AFM unit.....	29
3.3.1 Sample stage and cantilever stage.....	30
3.3.2 Deflection detection system.....	32
3.4 Sample and cantilever preparation method	34
3.4.1 Sample fix method	34
3.4.2 Sample preparation method	34
3.4.3 Cantilever preparation method.....	37
3.5 Operation circuit.....	38
3.5.1 AGC circuit.....	38
3.5.2 PLL circuit	38
3.5.3 FM-AFM/FM-KPFM circuit.....	39
3.6 Electron beam evaporator.....	39
3.6.1 Principle of the evaporator	39
3.6.2 Process of the evaporation	40
3.7 Conclusion.....	41

Chapter 4 Research about Pd NPs on alumina thin film..... 42

4.1 Introduction.....	42
4.2 Al ₂ O ₃ /NiAl(110) surface	42
4.2.1 Unit cell of alumina	42
4.2.2 Structure of surface defect	44
4.3 Investigations of charge state of metal NPs on Al ₂ O ₃ /NiAl(110) surface.....	46
4.3.1 Pd/Au atoms on Al ₂ O ₃ /NiAl(110) surface	46
4.3.2 Metal NPs on Al ₂ O ₃ /NiAl(110) surface.....	47
4.4 Investigations of CO reactivity on the metal NPs	49
4.4.1 CO molecule Lewis structure and MO diagram	49
4.4.2 CO bonding with transitions metals.....	49
4.5 Investigations of oxygen reactivity on Pd NPs	52

4.6 Conclusion.....	53
Chapter 5 Investigation of charge state of Pd nanoparticles on Al₂O₃/NiAl(110) surface by NC-AFM/KPFM.....	54
5.1 Introduction.....	54
5.2 Methods.....	55
5.2.1 AFM/KPFM method.....	55
5.2.2 Charge state by classical electrostatic model.....	56
5.2.3 Strategies to control the size and adsorption site of Pd NPs.....	57
5.3 Experimental results and discussion.....	58
5.3.1 Clarification of size and adsorption sites of Pd NPs.....	58
5.3.2 Characterization of charge state Pd NPs by AFM/KPFM.....	60
5.3.3 Size dependence of charge state of Pd NPs.....	62
5.3.4 Effect of tip polarization on KPFM measurement.....	64
5.5 Conclusion.....	68
Chapter 6 Charge state of CO molecule on Pd NPs/Al₂O₃/ NiAl(110) by NC-AFM /KPFM	69
6.1 Introduction.....	69
6.2 Methods.....	70
6.3 Results and discussion.....	71
6.3.1 Identification of CO molecule by force spectroscopy.....	71
6.3.2 Investigations of charge transfer of CO molecule on Pd NPs by KPFM.....	72
6.3.3 CO molecules adsorption on Pd NCs with atomic resolution.....	76
6.4 Conclusion.....	81
Chapter 7 Oxygen-adsorption-induced Charge State Change of Pd NCs on Al₂O₃/NiAl(110) Surface	83
7.1 Introduction.....	83

7.2 Methods.....	84
7.3 Results.....	85
7.3.1 Investigation of oxygen-adsorption-induced sintering.....	85
7.3.2 Oxygen-adsorption-induced charge state change.....	87
7.4 Discussion	91
7.5 Conclusion.....	93
Chapter 8 Summary and outlook	94
8.1 Summary	94
8.2 Outlook.....	95
References	96
Publications.....	112
Presentations.....	113
Acknowledgment.....	114

Chapter 1 Introduction

1.1 Background

1.1.1 Catalysis

Catalysis is the process of modifying the rate of a chemical reaction by adding catalysts and have been widely used in many fields such as chemical industry, global energy sources, and environmental protection [1, 2]. The use of gasoline fueled vehicles leads to increased emissions of molecules that are harmful to human health (e.g. CO, HC and NO_x). Reducing toxic gas emissions requires replacing fossil fuels with electric or solar energy, in combination with using energy storage devices, capturing and sequestering CO₂, or both [3]. However, the electric and hybrid vehicles are not competitive because their technology is still evolving when considering electric cars' pros and cons [4]. Therefore, efficiently converting toxic emissions to benign molecules such as H₂O, N₂ or CO₂ by catalysis is still central for gasoline fueled vehicles industry.

A three-way catalyst (TWC) is used in the vehicles to oxidize the toxic exhaust gas pollutants both hydrocarbons (HC) and carbon monoxide (CO) - and reduces nitrogen oxides (NO_x) into the harmless components water (H₂O), nitrogen (N₂) and carbon dioxide (CO₂). Depending on the operating conditions of the engine and the exhaust gas composition, conversion rates upwards of 98% can be achieved at close to stoichiometric conditions [5]. To further promote the conversion rate, the study of the catalytic mechanism of nanoparticles still remains a challenge.

The supported commercial catalyst is very difficult to study because of its complexity, with a large number of different components present in one catalyst, such as Pt, Rh, Al₂O₃, CeO₂, BaO, etc. [8-10]. It is therefore often simpler to study the model systems, such as Pt/Al₂O₃ or Rh/CeO₂. If certain surface-science techniques are to be used, the 'catalyst' under study has to be even simpler-a particular face of a metal single crystal. The development in the catalyst model systems involves the combination of materials science, computational science, and inorganic chemistry.

1.1.2 Modeling catalyst system

In the TWC, Pt/Pd or Pt/Rh oxidation catalysts were developed to limit hydrocarbon and carbon

monoxide emissions and later developed into ternary catalysts (TWC) that also convert NO_x emissions. Pt or Pd is used as the active oxidation catalyst, which facilitates the conversion of CO to N_2 . Dispersed Pt NPs on could provide larger reaction area and diversity of adsorption sites for reactants. However, the catalytic properties of the Pd NPs are in lack. To model the reactivity of the Pd NPs, we evaporate the Pd NPs on $\text{Al}_2\text{O}_3/\text{NiAl}(110)$ support.

Since the formation of a well-ordered Al_2O_3 over-layer (5.3 Å) by oxidation of $\text{NiAl}(110)$ was first reported [11], the $\text{Al}_2\text{O}_3/\text{NiAl}(110)$ system has been widely employed as a model catalyst support. The reasons are described as follow. At first, we choose the $\text{NiAl}(110)$ instead of $\text{NiAl}(100)$ as a substrate because the $\text{NiAl}(110)$ exhibits unimpeded oxide film growth over substrate steps. Therefore, the oxidation rate is not limited by the motion of surface steps, when we crystallize the $\text{NiAl}(110)$. At second, the well-ordered Al_2O_3 is an insulating thin film that can avoid charging problems when using electron spectroscopic methods. This alumina thin film also has advantages, such as high surface area and good thermal stability. Compared with other phase ($\gamma\text{-Al}_2\text{O}_3$), alumina thin film has attracted much more research interest because of their superior mechanical, chemical and electrical properties.

As reported, the reactivity of oxide-supported metal nanoparticle catalysts is traditionally understood by using the d-band model. The metal nanoparticle catalysts were regarded as extended metal surfaces [12]. However, such a picture of interpretation cannot depict the entire reactivity of oxide-supported metal nanoparticle catalysts because the effect from the size related electronic properties, adsorption sites dependence of the complexes and interface. In this regard, Pd NPs on $\text{Al}_2\text{O}_3/\text{NiAl}(110)$ system still remains issues such as the how to extract the charge of Pd NPs on $\text{Al}_2\text{O}_3/\text{NiAl}(110)$, the role of Pd NPs size and morphology in deducing the charge state, and charge transfer between reactants (CO , O_2) and Pd NPs remain fiercely debated, calling for a deep understanding experimentally and theoretically, which are vital for understanding of the catalytic mechanism at the ultimate spatial limit. We take a list in below:

- **Characterization of electronic properties of Pd NPs.**

Adsorption sites, size-dependent geometric and electronic effects of the metal NPs on the alumina thin film support have a significant effect on the catalytic activity. So that, tremendous experimental works have been performed.

In the study of gold supported on the oxide surface, it is reported that a higher chemical activity

exhibits from single atom to nanoparticles. It is clarified that Au bond weakly to the top of Al_s sites in the alumina/NiAl(110) [13]. STM (Scanning tunneling microscopy) and DFT (Density functional theory) calculations show that the excess electrons are located in the Au adatom. In addition, it is also clarified that Au aggregates to chains (1-10 atoms) on alumina films at 10 K. The direction of the Au chains influenced by the substrate and the charge state are negatively charged as analyzed by STS (Scanning tunneling spectroscopy) and DFT [14].

Pd-alumina catalysts have been studied experimentally and theoretically for decades since the pioneering works about the CO adsorption on Pd aggregates of varying size and order by H.-J. Freund [15]. The electronic properties of single Pd atom have been investigated on different sites of the alumina surface at 10 K, which is demonstrated that line defects influence the bonding between metal and oxide surface. In addition, whether it is desirable for the nucleation of Pd atoms on line defects of the alumina surface, it is reported when the thermal energy is sufficiently high, the line defects dominate the nucleation sites of Pd and Rh at 300 K [16]. Furthermore, it has been reported that alumina-supported Pt clusters play an important role in the activation of the catalyst by affecting the charge state [17].

Regardless of the above interesting results, but optimal catalytic size of the Pd NPs in this system have not attainable so far. So that, size sensitivity in the electronic properties at nanoscale are calling in experiment.

- **Characterization of CO molecule adsorption**

The adsorption of a single CO molecule on transition metals clusters is characterized by a variety of averaging techniques. It is demonstrated by infrared multiple photon dissociation (IR-MPD) spectroscopy that CO molecule only show top binding of both nickel and platinum, while, palladium clusters exhibit a variety of binding sites. By using STM technique, the adsorption sites and manipulation processes can be investigated, which enables addressing of individual visualization CO molecules [18,19]. Non-contact atomic force microscopy (NC-AFM) has been applied to quantify the force performance required to move CO laterally, the interaction between CO molecule and adatom or another CO molecule, and manipulation of its tilting [20-23].

Furthermore, some new insights have been illustrated the CO adsorption on the metal surface from molecular orbital principles in the aspect of DFT or on a single Pd-Fe₃O₄ catalyst by STM in real-time [24]. More recently, CO-terminated tips have been used to probe chemical binding forces on single Fe

atoms to elucidate individual atoms' chemical reactivity within flat Fe clusters depends on the coordination number of the investigated atom [25].

As the CO molecule could be activated at room temperature with the Pd NPs participation, up to now, spatial visualization CO molecule adsorption on the NPs is a big challenge for AFM. The AFM imaging difficulty comes from the complex short- and long-range interaction between tip apex and cluster on the surface, let alone the dynamic behavior detection such as charge transfer. There are no experiments to clarify the charge state of the CO molecule bond with Pd NPs at the nanoscale level, and as a function of the size of the Pd NPs, which is important to understand the size sensitive catalytic mechanism.

- **O₂ activation by metal surfaces: implications for bonding and reactivity on heterogeneous catalysts**

The coarsen, structure evolution and reduction/oxidation of catalytically active metal clusters are often accelerated by the presence of gases [26-28]. In a previous study, it was shown that the enhanced sintering of alumina-supported Pt clusters in an oxidizing atmosphere could be explained by a thermodynamic preference for the detachment of the PtO₂ volatile oxide instead of Pt atoms [29]. The CO-induced coalescence of Pd adatom supported on the Fe₃O₄(001) surface at room temperature has been fully investigated using a real-time-scale scanning tunnelling microscope, and Pd-carbonyl species have been found to be responsible for mobility [24].

It is difficult to investigate the charge state evolution of the Pd NPs after exposure of the oxygen molecule, because of the forming of the volatile oxide and coalescence property of the NPs. While, at the nanoscale level, no experimental works have been performed to clarify the charge transfer behaviour, which is important for understanding the CO oxidation reaction pathway.

1.1.3 Research by AFM/KPFM

Various technical methods have been adapted to investigate the catalytic reaction mechanism, such as XPS, IR, STM, AFM, KPFM, SEM and TEM. Among them, the AFM and KPFM have leading advantages for the characterizing catalytic mechanism due to its atomic resolution and high sensitivity.

Unlike STM, it can only be applied to conductive substrates, AFM can be applied to insulators and semiconductors. It can detect the various interactions when the tip is brought into contact with the sample down to 1 nm, including the van der Waals interaction (intermolecular force), the electrostatic interaction, the chemical interaction force based on the Morse potential, and the interaction force

between electric dipoles. With updating the operation mode, the non-contact AFM (NC-AFM) has been widely used in many researches. As an important AFM based apparatus, KPFM can measure a contact potential difference (CPD) between the tip and the sample. As the averaging effect, the CPD is strongly affected by tip sample distance, especially, short-range forces between the tip and the sample. For the high resolution KPFM, the local contact potential difference (LCPD) is introduced when the CPD associated with short-range force. Therefore, it is important to know how CPD or LCPD correspond to the physical properties of the surface. For example, for ionic solids, the atomic LCPD contrast originates from the ionic bonding force (dipole interactions) between the surface atom and the tip apex atom [30]. If the semiconductor surfaces, the force is attributed to a covalent bonding interaction [31]. Therefore, the origin of the LCPD contrast is dependent on the not only the sample but also tip apex.

For high-resolution KPFM, the preparation and selection of an atomically sharp and conducting AFM tip is also important. Because it related to how to interpret the physical properties of the imaging surface. The most commonly used AFM tip is the heavily doped Si cantilever, which should be heat treatment followed by Ar ion sputtering to remove the oxide layer and other contamination [32]. This tip can produce the high resolution KPFM images, but the tip is easier to pick up atom from surface or rearrangement of the tip apex atoms. Additionally, the interpretation of the LCPD by Si tip apex is difficult to exclude the Si induced dipole moment, which maybe the main force for the LCPD contrast [33]. The second type of tip apex is made of, for example, Pt/Ir-coated Si cantilevers, Au or Cr coating of Si cantilevers, which could also produce sub-nanometer resolution KPFM images [34]. This tip can produce the high resolution KPFM images, and the tip apex is relatively stable. Obtaining the best spatial resolution requires optimization of the tip coating film thickness. There are also other types of the cantilever, which is prepared for different measurement requirement [35, 36].

An important application of KPFM is the to electrical property analysis of nanostructures. At first, the KPFM provided the work function signal present more details about surface topography. For example, the small features, difficult to observe in the topographic image due to a large topography, are distinguishable by KPFM. From KPFM result, we could know the surface potential differences between surface defects, step edge and terrace on various surface. The distinguished charged defects are considered to be the preferable nucleation sites for the nanostructure. For example, Barth et al. have investigated Au nanostructures on alkali halide (001) surfaces using KPFM to study whether metal

nanostructures will screen defect charges or become charged [37]. The charge transfer will significantly affect the surface and nanostructure properties, hence govern the catalyst system reactivity. Therefore, KPFM is a powerful tool to investigate the charging factor for catalytic processes.

Besides the characterization of the charge transfer in the nano-catalyst system, AFM and KPFM also an efficient tool to do the manipulation with single-atom or single-electron level precision. Both a q-Plus non-contact AFM/KPFM system or OBD non-contact AFM/KPFM could probe single atoms on the surface [38]. They got some great results, such as allowing single atoms to be imaged, detecting the charge state of a single atom on thin insulating films. They explained the nanometer resolution of nanostructure, molecules on the supporting insulating surface were a function of the local surface potential and the local dipole moment. In a further extension, charges can be added or removed at specific sites in molecules, adatoms. The entire molecule or molecular network can then be characterized by KPFM or KPFS to study charge transport. KPFM has also enabled the experimental determination of the effect of quantum size on the electronic properties of metallic nanostructures.

In total, the introduction of nc-AFM/KPFM has revolutionized the characterization and investigation of catalytic reaction mechanism. Based on nc-AFM, new characterization and analysis methods such as KPFM have been developed, and multi-channel imaging techniques based on nc-AFM can provide additional more physical information about surface properties as well as atomic forces. The nc-AFM and KPFM open up an unprecedented research area for surface science, especially for the investigation of heterogeneous catalysis.

1.2 Purpose of this research

In this doctoral dissertation our fundamental concern is to investigate the size dependence of charge state of Pd NPs on $\text{Al}_2\text{O}_3/\text{NiAl}(110)$ on catalyzed oxidation of CO at room temperature (RT). First, we investigate that how to deduce the charge state of Pd NPs by measuring the local contact potential difference (LCPD) and classical electrostatic model for the Pd NPs. The size related electronic and geometric properties will be presented. Second, we extract the charge state of the CO-Pd NPs to provide access to discuss the charge transfer effect in the different size of Pd NPs. Finally, we give a starting point to investigate the charge state of the Pd NPs after oxygen dissociation, which provide access to discuss the catalytic reaction pathway in the different size of Pd NPs.

1.3 Thesis outline

The dissertation is organized as follows:

■ In chapter 1, we firstly introduce the demand for the catalytic research in the vehicles to oxidize the toxic gas, followed by the realistic and scientific reason to model the Pd nanoparticles $\text{Al}_2\text{O}_3/\text{NiAl}(110)$ catalytic system. In detail, the previous related researches are clarified, problems present in the searching optimal catalytic size for CO oxidation reaction and demand for size related electronic and geometric properties are discussed in details. The purpose of the dissertation is ambiguously described.

■ In chapter 2, we discuss the principle of the nc-AFM. Firstly, the different interaction between tip and sample. Secondly, the operation method of atomic force microscope and noise level. Thirdly, the principle of KPFM measurements is introduced briefly.

■ In chapter 3, the experimental setup of the home-built scanning probe microscopy system is described in detail. Firstly, the UHV AFM equipment at room temperature. Then, sample and cantilever stages, the deflection detection system, the tube scanner and feedback system are presented. The electron beam evaporator principle and Pd NPs deposition method are described in the detail.

■ In chapter 4, we systematically reviewed and discussed the past researches on $\text{Al}_2\text{O}_3/\text{NiAl}(110)$ surface, including the atomic structure of surface and line defects, which are necessary steps for catalytic mechanism. Additionally, the physical property of the Pd NPs and CO molecule, especially the CO-metal bonding mechanism. Finally, the adsorption of the oxygen and the theoretical works about the charge states of the Pd nanoclusters.

■ In chapter 5, we deduce the size dependence of charge state of the Pd NPs by measuring the local contact potential difference (LCPD) of Pd NPs on the alumina surface through KPFM and classical electrostatic model for the spheres. The charge state of Pd NPs on the $\text{Al}_2\text{O}_3/\text{NiAl}(110)$ surface will be presented and discussed.

■ In chapter 6, we present and discuss the size dependence of the charge state of the CO molecule on Pd NPs by measuring the local contact potential difference (LCPD) of Pd NPs on the alumina surface through KPFM and classical electrostatic model for the spheres. In addition, a complete atomic understanding of variation in reactant molecule adsorption sites on metal nanoclusters (NCs) is presented.

- In chapter 7, we present and discuss the charge state evolution of the Pd NPs is studied during exposure of molecular oxygen.

- In chapter 8, we summarize the importance of research. Finally, we give a future work.

Chapter 2 Principles of non-contact atomic force microscopy

2.1 Introduction

In this chapter, the principle of Atomic Force Microscopy (AFM) is described. In sections 2.2, the interactions between the probe and the sample are described. In sections 2.3, the principle of AFM has explained: the operating modes, the detection of the frequency shift of the cantilever, and the stability conditions for the cantilever vibration. In sections 2.4, the principle of Kelvin probe force microscopy (KPFM) is explained, starting from definition of work function and contact potential difference, followed by describing KPFM with feedback and minimum detectable CPD. Furthermore, the origin of the local contact potential difference is explained using examples from various previous studies. Finally, we summarize this chapter.

2.2 The interaction force between tip and sample

AFM could detect the various interactions F_{ts} when the tip is brought near to sample down to nano scale. The main interactions between the tip and the sample includes the van der Waals interaction F_{vdw} (intermolecular force), the electrostatic interaction F_{ele} , the chemical interaction force based on the Morse potential F_{chem} , and the interaction force between electric dipoles F_{dip} . [1]

$$F_{ts} = F_{vdw} + F_{ele} + F_{chem} + F_{dip} \quad (2.1)$$

In the above, the van der Waals interaction F_{vdw} and electrostatic interaction F_{ele} are the dominant long-range force, whereas the electrostatic interaction F_{ele} and electric dipoles F_{dip} dominant short-range force. The total interaction force can be characterized by the following model of the tip-sample relationship, see the Figure 2.1.

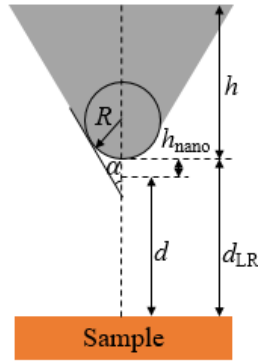


Figure 2.1 Model diagram of a nanotip with a height h_{nano} . d is the distance between the tip and the sample, d_{LR} is the distance between the macroscopic cantilever and the sample, R , α is the radius and angle of curvature of the tip, and h is the height of the conical part.

(1) Van der Waals interaction

Van der Waals force includes attraction and repulsion between atoms, molecules, and surfaces, as well as other intermolecular forces. Van der Waals and electrostatic interaction forces are the dominant forces when the tip and sample are separated more than 1 nm. Van der Waals forces can be interpreted in terms of quantum mechanics as follows. If we have two positive charged atoms with negative electron cloud surrounded, they are nonpolar at far distance. The atom, getting near to another atom, could be polarized with the negative at the near site and positive at the opposite site, which could be called as temporary dipole. The temporary dipole could induce the dipole of the nearby atom, therefore, the interaction between the temp dipole and induced dipole is called Van der Waals force, see the Figure 2.2.

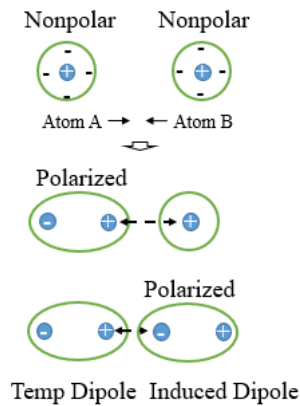


Figure 2.2 Interpretation model of Van der Waals force.

The van der Waals interaction force between the tip and the sample, according to Argento's group [2], can be expressed by the following equation:

$$F_{\text{vdw}} = \frac{HR^2(1 - \sin \alpha)(R \sin \alpha - d_{\text{LR}} \sin \alpha - R - z_0)}{6d_{\text{LR}}^2(d_{\text{LR}} + R - R \sin \alpha)^2} - \frac{H \tan \alpha (d_{\text{LR}} \sin \alpha + R \sin \alpha + R \cos(2\alpha))}{6 \cos \alpha (d_{\text{LR}} + R - R \sin \alpha)^2} \quad (2.2)$$

(2) Electrostatic interaction

The electrostatic interaction force is the force of attraction or repulsion between two charged particles, which like same charges repel and opposite charges attract. The electrostatic force between two charged particles can be quantified by Coulomb's law. In the AFM, the tip and the sample have different charges and thus different potential energies. The contact potential difference of tip and sample originates from local charges or multipoles. In addition, a bias voltage is introduced to apply and compensate the contact potential difference between tip and sample. Various approximations have been introduced for the electrostatic interaction force between the tip and the sample, here, we introduce an approximation by Hudlet's group [3]. In the model shown in Figure 2.1, which assumes a hemispherical tip, the electrostatic interaction force can be described by the following equation:

$$F_{\text{ele}} = \pi \varepsilon_0 \left[\frac{R^2}{d_{\text{LR}}(d_{\text{LR}} + R)} \right] V^2 \quad (2.3)$$

Taking into the sharpness of the tip apex, the equation is written as follow:

$$F_{\text{ele}} = \pi \varepsilon_0 R^2 \frac{(1 - \sin \alpha)}{z[z + R(1 - \sin \alpha)]} V^2 \quad (2.4)$$

(3) Chemical interaction

When tip approaches the sample, the distance of less than 1 nm, a short-range chemical interaction is generated, which depends exponentially on the distance. The tip-sample chemical interaction bonds can be explained by the quantum theory. In practice, a simplified description is used to predict the bonding strength and polarity. This chemical interaction attributes to the atomic or subatomic resolution of the surface in AFM. The chemical interaction is described by many different theoretical models. Here, we describe the Morse potential [4].

$$U_{\text{chem}} = U_0 \left[\exp\left(-2 \frac{d - d_0}{\lambda}\right) - 2 \exp\left(-\frac{d - d_0}{\lambda}\right) \right] \quad (2.5)$$

d_0 is the position at the minimum of the potential, U_0 is the minimum of the potential and λ determines the extent of the interaction force due to covalent bond.

Derivative from the Morse potential equation (2.5), the chemical force is shown as follow:

$$F_{\text{chem}} = \frac{2U_0}{\lambda} \left[\exp\left(-2\frac{d-d_0}{\lambda}\right) - 2\exp\left(-\frac{d-d_0}{\lambda}\right) \right] \quad (2.6)$$

2.3 Principle of operation of AFM

2.3.1 Operation modes

According to the operation mode, AFM can be divided into three types.

1. The contact mode, in which the cantilever is brought into contact with the sample and the surface topography is measured from the displacement of the cantilever.

2. The tapping mode, in which the cantilever is periodically brought into contact with the sample and the surface profile is measured from the displacement of the cantilever vibration amplitude.

3. The non-contact mode, where the cantilever is not in contact with the sample and the surface topography is measured from the change in vibration frequency (or amplitude) of the cantilever.

In the previous AFM, the contact method is mainly used, but it is difficult to achieve high resolution because the tip apex will be damaged by the constant contact of the tip apex with the sample. In the tapping method, the cantilever is periodically brought into contact with the sample, so the tip apex is also likely to be damaged. Therefore, the non-contact mode of AFM has been proposed. The non-contact mode measures the surface by detecting the change in the mechanical resonance frequency of the cantilever, and there are two methods of detecting the change: 1) amplitude modulation (AM-AFM), where the cantilever ensemble is excited at a fixed frequency, usually near or at the free resonance frequency. The oscillation amplitude is used as a feedback parameter to image the sample topography. However, it is not possible to extend the amplitude modulation mode to UHV. Because the minimum frequency shift detectable in slope detection due to thermal noise, which depends on the cantilever parameters [4]. In slope detection, increasing the Q reduces the bandwidth of the system. This makes slope detection unsuitable for most vacuum applications. Therefore, 2) frequency modulation (FM - AFM) developed by Albrecht et al [1,5]. In FM-AFM, the direct measurement of the resonance frequency of the cantilever, which modified by tip sample interaction, is used as a feedback parameter to image the sample topography. In the following, the principle of FM-AFM adopted in the experiment is described in detail below.

In Figure 2.3, the dashed blue line is the resonance characteristic when the cantilever is sufficiently far from the sample. The mechanical resonance frequency of cantilever is

$$f_0 = \frac{1}{2\pi} \sqrt{\frac{k}{m}} \quad (2.7)$$

where k and m are the spring constant and the effective mass of the cantilever, respectively. As the tip apex is brought closer to the sample, the effective spring constant of the cantilever changes from k to $k - \partial F / \partial z$ due to the force gradient inducing by tip sample interaction. Hence the mechanical resonant frequency of the cantilever is given as

$$f_1 = \frac{1}{2\pi} \sqrt{\frac{k - \frac{\partial F}{\partial z}}{m}} \quad (2.8)$$

If the change in resonant frequency (frequency shift) is $\Delta f = f_0 - f_1$, then $k \gg \partial F / \partial z$, the force gradient of the cantilever is approximated as follows

$$\frac{\partial F}{\partial z} = 2k \frac{\Delta f}{f_0} \quad (2.9)$$

Hence, the FM-AFM could be used to directly detect the force gradient or force with ultra-sensitivity, so that, even the weakest attraction between the tip and the atoms on the sample surface could be detected and measured without damage the surface. Therefore, atomic resolution of the surface can be obtained in high vacuum.

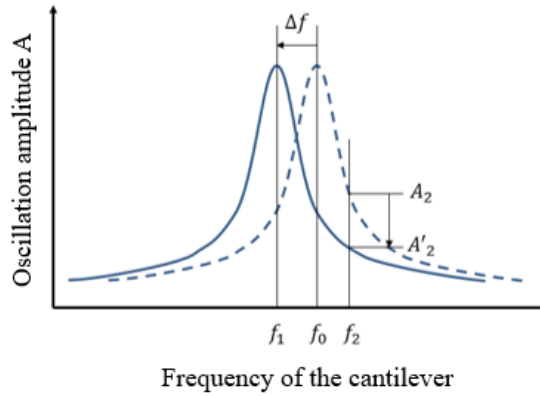


Figure 2.3 Principle of non-contact force measurement. The dashed blue line is when the tip is very far away from the sample and the solid line is when the probe is close to the sample.

2.3.2 Detection of frequency shift

As mentioned in last section, the detection of frequency shift is essential in FM-AFM. The frequency shift is obtained by solving the equation of motion of the cantilever, which is expressed by the following

equation,

$$m\ddot{z}(t) + \frac{m\omega_0}{Q}\dot{z}(t) + kz(t) = kA_{\text{exc}}\cos\omega t + F_{\text{ts}}[z_{\text{const.}} + z(t)] \quad (2.10)$$

where $z(t)$, m , Q , ω_0 , k is the displacement, effective mass, quality factor, resonant frequency and spring constant of the cantilever, respectively. A_{exc} is the amplitude of the excitation signal, F_{ts} is the interaction force, and $z_{\text{const.}}$ is the distance between the tip and sample when the displacement of the cantilever is zero. Substituting $\omega_0 = \sqrt{(k/m)}$ into equation (2.10), we could obtain

$$\ddot{z}(t) + \frac{\omega_0}{Q}\dot{z}(t) + \omega_0^2 z(t) = \omega_0^2 A_{\text{exc}}\cos\omega t + \frac{\omega_0^2}{k} F_{\text{ts}}[z_{\text{const.}} + z(t)] \quad (2.11)$$

The solution of this equation of motion is assumed to be the following equation

$$z(t) \approx A\cos(\omega t - \phi) \quad (2.12)$$

A represents the amplitude of the cantilever. The schematic diagram of the vibration of the cantilever under the above conditions is shown in Figure 2.4. Substituting equation (2.12) into equation (2.11), we obtain

$$\begin{aligned} \frac{\omega_0^2 - \omega^2}{\omega_0^2} A\cos(\omega t - \phi) - \frac{\omega A}{Q\omega_0} \sin(\omega t - \phi) - A_{\text{exc}}\cos\omega t \\ = \frac{1}{k} F_{\text{ts}}[z_{\text{const.}} + z(t)] \end{aligned} \quad (2.13)$$

by multiplying $\cos(\omega t - \phi)$ with equation (2.13) and integrating it in one cycle, then transforming the variables to $\theta = \omega t$ and rearranging the equation, we obtain the following equation

$$\cos\phi = \frac{\omega_0^2 - \omega^2}{\omega_0^2} \frac{A}{A_{\text{exc}}} - \frac{1}{\pi k A_{\text{exc}}} \int_0^{2\pi} F_{\text{ts}}[z_{\text{const.}} + z(t)] \cos\theta d\theta \quad (2.14)$$

Also, by multiplying equation (3.13) by $\sin(\omega t - \phi)$ and integrating over one cycle, we obtain the following equation

$$\sin\phi = \frac{\omega}{Q\omega_0} \frac{A}{A_{\text{exc}}} - \frac{1}{\pi k A_{\text{exc}}} \int_0^{2\pi} F_{\text{ts}}[z_{\text{const.}} + z(t)] \sin\theta d\theta \quad (2.15)$$

If we substitute $F_{\text{ts}}=0$, when there is no interaction force between the tip and sample, then $\sin\phi$ and $\cos\phi$ are

$$\cos\phi = \frac{\omega_0^2 - \omega^2}{\omega_0^2} \frac{A}{A_{\text{exc}}} \quad (2.16)$$

$$\sin\phi = \frac{\omega}{Q\omega_0} \frac{A}{A_{\text{exc}}} \quad (2.17)$$

Substituting equations (2.16) and (2.17) into $\cos^2\phi + \sin^2\phi = 1$, the amplitude A and phase ϕ are shown as following:

$$A = \frac{A_{\text{exc}}Q}{\sqrt{\left(1 - \frac{f^2}{f_0^2}\right)^2 Q^2 + \frac{f^2}{f_0^2}}} \quad (2.18)$$

$$\tan\phi = \frac{f_0 f}{(f_0^2 - f^2)Q} \quad (2.19)$$

Now, we rewrite $\omega_0 = f_0$ and $\omega = f$. When $f = f_0$, from equations (2.18) and (2.19)

$$A = A_{\text{exc}}Q \quad (2.20)$$

$$\tan\phi = -\frac{\pi}{2} \quad (2.21)$$

It can be seen that the response signal of the cantilever is delayed in phase by 90° when the cantilever is excited at its resonant frequency.

Next, we consider the case when there is an interaction force between the tip and sample, i.e. $F_{\text{ts}} \neq 0$.

In this case, we transform equation (2.13) as follows

$$\frac{\omega_0^2 - \omega^2}{\omega_0^2} = \frac{A_{\text{ext}}}{A} \cos\phi + \frac{1}{\pi k A} \int_0^{2\pi} F_{\text{ts}}[z_{\text{const.}} + z(t)] \cos\theta d\theta \quad (2.22)$$

Then, we substitute the following approximation into equation (2.22)

$$\frac{\omega_0^2 - \omega^2}{\omega_0^2} \approx -2 \frac{\Delta f}{f_0} \quad (2.23)$$

Then the frequency shift Δf is expressed by the following equation

$$\Delta f = -\frac{f_0 A}{2A_{\text{exc}}} \cos\phi - \frac{f_0}{2\pi k A} \int_0^{2\pi} F_{\text{ts}}[z_{\text{const.}} + z(t)] \cos\theta d\theta \quad (2.24)$$

The cantilever is excited at its resonant frequency and is therefore 90° out of phase. The first term in equation (2.24) is zero and the frequency shift is

$$\Delta f = -\frac{f_0}{2\pi k A} \int_0^{2\pi} F_{\text{ts}}[z_{\text{const.}} + z(t)] \cos\theta d\theta \quad (2.25)$$

From equation (2.25), it can be seen that the frequency shift of the cantilever is proportional to the sum of the interaction forces between the tip and sample detected in one cycle by the cantilever excited at the resonance frequency. As shown in Figure 2.1, if we set $z_{\text{const.}} = d + A$ and transform the variables as $z(t) = \cos(\omega t - \phi) = \cos\theta = u$, the equation (2.25) is expressed as

$$\Delta f = -\frac{f_0}{\pi k A} \int_{-1}^1 F_{\text{ts}}[d + A(1 + u)] \frac{u}{\sqrt{1 - u^2}} du \quad (2.26)$$

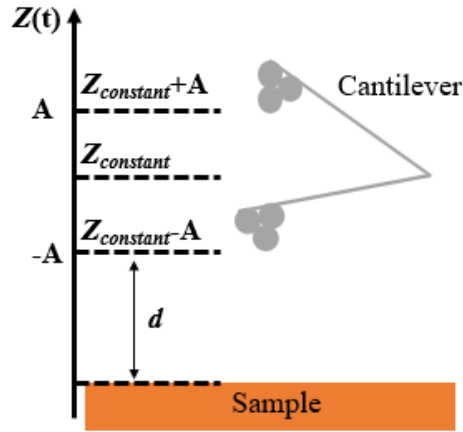


Figure 2.4 Schematic diagram of cantilever vibrations.

2.3.3 Formalism of force

In general, if the vibration amplitude of cantilever is very large or small, so that the force gradient cannot be considered as constant simply. Even the huge demand for force expression, a general expression for arbitrary oscillation amplitudes was unknown. As proposed by Sadler Jarvis, a force deconvolution method using Laplace transformation and a Bessel function which can be better fit for the arbitrary oscillation amplitude [6].

The interaction $F_{ts}(z)$ between tip and sample can be written as an $A(\lambda)$, which is the inverse Laplace transformation of $F_{ts}(z)$ as follow:

$$F_{ts}(z) = \int_0^{\infty} A(\lambda) \exp(-\lambda z) d\lambda \quad (2.27)$$

substituting to expression (2.26), we could obtain frequency shift as follow:

$$\Delta f = -\frac{f_0}{kA} \int_{-1}^1 \int_0^{\infty} A(\lambda) \exp(-\lambda z - \lambda A(1+u)) \frac{u}{\sqrt{1-u^2}} dz du \quad (2.28)$$

If we exchange the integration as follow:

$$\Delta f = -\frac{f_0}{kA} \int_0^{\infty} \int_{-1}^1 A(\lambda) \exp(-\lambda z - \lambda A(1+u)) \frac{u}{\sqrt{1-u^2}} du dz \quad (2.29)$$

Then, we use the transformed Bessel function, which defined as:

$$I_n(z) = \frac{1}{\pi} \int_0^{\pi} e^{z \cos \theta} \cos(n\theta) d\theta \quad (2.30)$$

when $n=1$, the equation could be expressed as:

$$I_1(z) = \frac{1}{\pi} \int_0^{\pi} e^{z \cos \theta} \cos \theta d\theta \quad (2.31)$$

substituting $u = \cos\theta$ and $I_1(z) = -I_1(-z)$, the above could be expressed as:

$$I_1(z) = -\frac{1}{\pi} \int_{-1}^1 e^{-zu} \frac{u}{\sqrt{1-u^2}} du \quad (2.32)$$

When $T(x) = I_1(x)e^{-x}$, then the equation (2.29) could be expressed as:

$$\frac{\Delta f}{f_0} = \frac{1}{kA} \int_0^\infty A(\lambda) T(\lambda A) e^{-\lambda z} d\lambda \quad (2.33)$$

Using the inverse Laplace transformation (2.34) to both sides of (2.33)

$$\mathcal{L}[Y(\lambda)] = \int_0^\infty Y(\lambda) \exp(-\lambda z) dz \quad (2.34)$$

substituting following

$$A(\lambda) = \frac{kA}{T(\lambda A)} \mathcal{L}^{-1} \left[\frac{\Delta f}{f_0} \right] \quad (2.35)$$

$$F_{ts}(z) = \mathcal{L}[A(\lambda)] \quad (2.36)$$

Substituting equation (2.35) to (2.36), then interaction between tip and sample could be expressed as follow:

$$F_{ts}(z) = \mathcal{L} \left[\frac{kA}{T(\lambda A)} \mathcal{L}^{-1} \left[\frac{\Delta f}{f_0} \right] \right] \quad (2.37)$$

The analytical approximation of $T(x)$ is

$$T(x) = \frac{x}{2} \left(1 + \frac{1}{8} x^2 + \sqrt{\frac{\pi}{2}} x^{\frac{3}{2}} \right)^{-1} \quad (2.38)$$

Substituting equation (2.38) to (2.37), then interaction between tip and sample could be expressed as follow:

$$F_{ts}(z) = 2k \left\{ \mathcal{L} \left[\lambda^{-1} \mathcal{L}^{-1} \left[\frac{\Delta f}{f_0} \right] \right] + \frac{1}{8} A^{\frac{1}{2}} \mathcal{L} \left[\lambda^{-\frac{1}{2}} \mathcal{L}^{-1} \left[\frac{\Delta f}{f_0} \right] \right] + \sqrt{\frac{\pi}{2}} A^{\frac{3}{2}} \mathcal{L} \left[\lambda^{\frac{1}{2}} \mathcal{L}^{-1} \left[\frac{\Delta f}{f_0} \right] \right] \right\} \quad (2.39)$$

$\mathcal{L}^{-1}[\Delta f/f_0]$ is the function of λ .

Now, substituting (2.40), (2.41), (2.42) and (2.43)

$$\mathcal{L}[\lambda^{-\alpha} Y(\lambda)] = I^\alpha \mathcal{L}[Y(\lambda)] \quad (2.40)$$

$$\mathcal{L}[\lambda^\alpha Y(\lambda)] = D^\alpha \mathcal{L}[Y(\lambda)] \quad (2.41)$$

$$I^\alpha \varphi(\lambda) = \frac{1}{\Gamma(\alpha)} \int_\lambda^\infty Y(\lambda) \frac{\varphi(t)}{(t-\lambda)^{1-\alpha}} dt \quad (2.42)$$

$$D^\alpha \varphi(\lambda) = \frac{(-1)^n}{\Gamma(n-\alpha)} \frac{d^n}{d\lambda^n} \int_\lambda^\infty \frac{\varphi(t)}{(t-\lambda)^{\alpha-n+1}} dt \quad (2.43)$$

to (2.39), we could get the expression as the follow:

$$F_{ts}(z) = 2k \int_z^\infty \left[\left(1 + \frac{A^{\frac{1}{2}}}{8\sqrt{\pi(t-z)}} \right) \Omega(t) - \frac{A^{\frac{3}{2}}}{\sqrt{2(t-z)}} \frac{d\Omega(t)}{dz} \right] dt \quad (2.44)$$

while $\Delta f/f_0 = \Omega(z)$. Here, we could analytically derive the tip sample interaction $F_{ts}(z)$ using Δf . The first term includes the small amplitude contribution and the second term include the large amplitude contribution. For the wide range of amplitude, the Sadler Jarvis method converge to the analytical determinable exact solutions and gives an errorless than 5% in all cases. However, this formula is only valid for the constant oscillation amplitude and experimental realization is important.

The interaction potential can be derived as follows

$$U_{ts}(z) = 2k \int_z^\infty \Omega(t) \left((t-z) + \frac{A^{\frac{1}{2}}}{4} \sqrt{\frac{t-z}{\pi}} + \frac{A^{\frac{3}{2}}}{\sqrt{2(t-z)}} \right) dt \quad (2.45)$$

2.3.4 Stability conditions for cantilever vibration

In FM-AFM, the cantilever must be excited stably at its resonant frequency. When the cantilever is brought close to the sample to a certain distance, the interaction force increases and a phenomenon called jump-to-contact occurs, where the probe is pulled into the sample.[2] In order to avoid jump-to-contact, the spring constant of the cantilever must be as follows

$$k > \max \left(-\frac{\partial F_{ts}}{\partial z} \right) = k_{ts}^{\max} \quad (2.46)$$

Furthermore, considering that the cantilever is periodically excited with amplitude A , the following conditions are also necessary

$$kA > \max (-F_{ts}) \quad (2.47)$$

F_{ts} satisfying these conditions will allow stable measurements without causing jump-to-contact.

When the cantilever is excited, non-conservative forces are generated between the tip and sample due to thermal factors and surface interactions. In order to detect the interaction force F_{ts} between the tip while maintaining a constant vibration amplitude of the cantilever, energy must be applied to the cantilever to compensate for the energy dissipation ΔE_{ts} caused by these non-conservative forces. When the energy dissipation exceeds the internal dissipation of the cantilever, the vibration amplitude of the cantilever cannot be kept constant and the FM-AFM cannot keep stable measurements. Therefore, the following conditions are required to keep the vibration amplitude of the cantilever constant.[2]

$$\frac{k}{2} A^2 \geq \Delta E_{ts} \frac{Q}{2\pi} \quad (2.48)$$

2.4 Principle of KPFM

2.4.1 Work function

The work function is defined as the energy required to remove one electron from the surface of a material into a vacuum. The energy required to remove one electron from a solid containing N electron into an infinite distance (vacuum) is given by the base energy as E_N

$$\Phi = -(E_N - E_{N-1} - E_{vac}) = -\frac{\partial E_N}{\partial N} + E_{vac} = -\mu + E_{vac} \quad (2.49)$$

where μ is the chemical potential of the solid and E_{vac} is the vacuum level. In the case of metals, this corresponds to the Fermi level. This means that for metals, the work function is the difference between the vacuum level and the Fermi level.

The work function is a value that is strongly influenced by the structure of the material at the atomic level, its surface orientation and the adsorption of other atoms. This means that the work function is determined by the electronic state of the valence electrons near the outermost surface layer. Therefore, the electronic structure theory is necessary to discuss the work function value quantitatively. In this paper, we present the results of the Jellium model of the work function [7]. The Jellium model is a system in which the charge in the metal is assumed to be uniformly distributed. In other words, it consists of a background positive charge ρ^+ , which is obtained by uniformly averaging the ionic centers, and a density of free electrons ρ that neutralizes the background charge as a whole. The electron density distribution of the Jellium model was calculated by Lang, Kohn et al. and is shown in Figure 2.5.

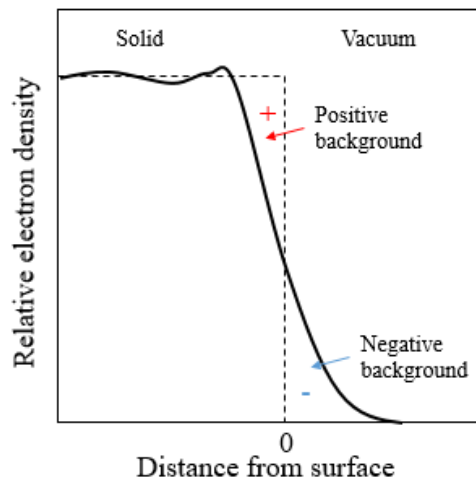


Figure 2.5 Electron density distribution on a Jellium surface [7].

At the surface, the background positive charge is assumed to be a staircase function. However, they are ejected from the surface to the vacuum side ($z > 0$) due to the kinetic energy of the electrons, while inside the surface they oscillate and approach the mean value (bulk charge density) asymptotically. This phenomenon causes the charge distribution on the surface to be negative at the outermost surface, but positive at the very inner surface of the Jellium, forming an electric double layer. The electric double layer deepens the potential of the electrons inside the surface. Its size is

$$\Delta\phi = -4\pi \int_{-\infty}^{+\infty} z(\rho(z) - \rho_+\theta(-z))dz \quad (2.50)$$

where $\theta(z)$ is a staircase function.

The electrons deep below the surface are affected by the exchange and correlation potential V_{XC} in addition to this electrostatic potential, so that the total potential is

$$V_{\text{eff}}(z) = V_{\text{eff}}(-\infty) = \phi(-\infty) + V_{XC}(\rho_+) \quad (2.51)$$

the difference in depth of the potential well from the vacuum to the interior of the metal is

$$\Delta V_{\text{eff}} = V_{\text{eff}}(+\infty) - V_{\text{eff}}(-\infty) = \Delta\phi - V_{XC}(\rho_+) \quad (2.52)$$

The work function is the difference between the vacuum level and the Fermi level, as shown in Figure 2.6. Since the work function is the difference between the vacuum level and the Fermi level, it is equal to ΔV_{eff} minus the kinetic energy $\hbar^2 k_F^2 / 2m$ corresponding to the Fermi level. Hence the work function Φ is

$$\Phi = \Delta\phi + \left\{ |V_{XC}(\rho_+)| - \frac{\hbar^2}{2m} (3\pi^2 \rho_+)^{2/3} \right\} \quad (2.53)$$

The first term on the right-hand side of equation (2.53) is determined by the charge distribution near the surface and is called the surface term Φ_s . On the other hand, the second term on the right-hand side is determined only by the bulk properties and is called the bulk term Φ_B . In the Jellium model, it is a function of the background positive charge density only.

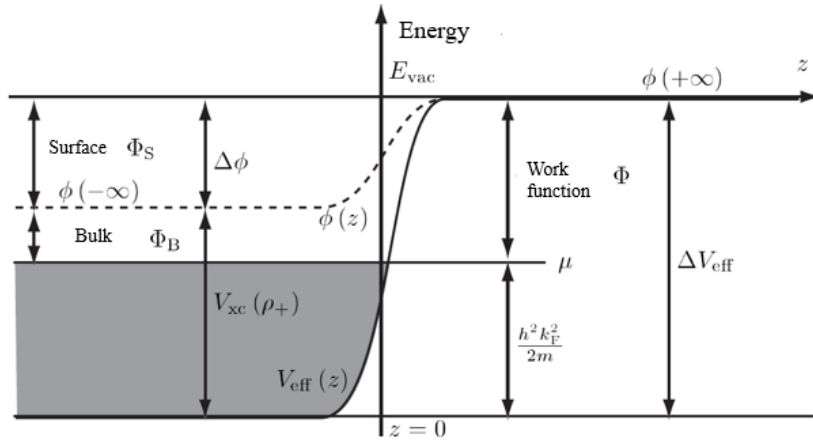


Figure 2.6 Relationship between potential and work function at a surface [8].

2.4.2 Contact potential difference

The contact potential difference is the potential difference that occurs when two conductors with different work functions are brought into electrical contact. The work functions of the two conductors are Φ_A and Φ_B respectively (Figure 2.7(a)). When these conductors are brought into contact with each other electrically (Figure 2.7(b)) the electrons flow to the object with a lower chemical potential in order to become energetically stable. As soon as the chemical potentials μ_A and μ_B of the two electrons coincide, a contact potential difference $V_{CPD} = \Delta\Phi/e$ due to the work function difference $\Delta\Phi = \Phi_A - \Phi_B$ is generated between the two conductors.

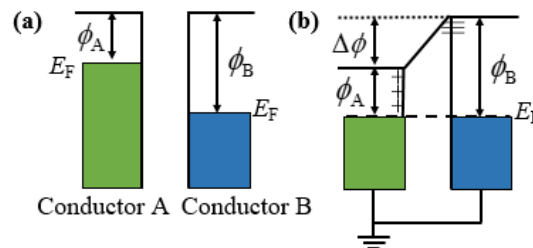


Figure 2.7 Schematic diagram of contact potential difference (a) before contact (b) after contact, when contact potential difference occurs.

2.4.3 KPFM with voltage feedback

KPFM with voltage feedback has been developed as an application of non-contact atomic force microscopy. The principle of KPFM with voltage feedback is described in the following.

The electrostatic interaction force between the tip and the sample in non-contact atomic force

microscopy can be expressed by the following equation [9],

$$F_{\text{ele}} = -\frac{1}{2} \frac{dC}{dz} (V_{\text{bias}} - V_{\text{CPD}})^2 \quad (2.54),$$

where C is the capacitance between the tip and samples, V_{bias} is the voltage applied between the tip and samples and V_{CPD} is the contact potential difference between the tip and sample. When $V_{\text{bias}} = V_{\text{DC}} + V_{\text{AC}} \cos \omega t$, which is the DC voltage V_{DC} plus the AC voltage $V_{\text{AC}} \cos \omega t$, is applied to the sample, equation (2.54) becomes

$$F_{\text{ele}} = -\frac{1}{2} \frac{dC}{dz} (V_{\text{DC}} + V_{\text{AC}} \cos \omega t - V_{\text{CPD}})^2 \quad (2.55)$$

Expanding equation (2.55), we obtain

$$F_{\text{ele}} = -\frac{1}{2} \frac{dC}{dz} \left\{ (V_{\text{DC}} - V_{\text{CPD}})^2 + \frac{V_{\text{AC}}^2}{2} \right\} - \frac{dC}{dz} (V_{\text{DC}} - V_{\text{CPD}}) V_{\text{AC}} \cos \omega t + \frac{1}{4} \frac{dC}{dz} V_{\text{AC}}^2 \cos 2\omega t \quad (2.56)$$

The first term on the right-hand side of equation (2.56) is the electrostatic interaction force due to the DC component, the second term is the electrostatic interaction force with a component of modulation frequency ω , and the third term is the electrostatic interaction force with a component of modulation frequency 2ω . In KPFM with voltage feedback, the modulation frequency ω component of the electrostatic interaction force is detected by a lock-in amplifier and the sample surface is scanned with feedback applied so that this component is zero, i.e. the DC voltage V_{DC} is $V_{\text{DC}} = V_{\text{CPD}}$. By mapping the V_{DC} , the contact potential difference image of the surface can be obtained. The interpretation model of KPFM measurement is shown in the Figure 2.8.

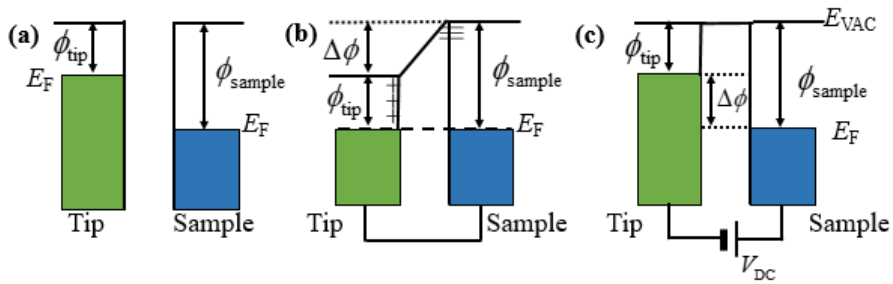


Figure 2.8 Energy levels of the AFM tip and sample: (a) tip and sample are separated by distance d with no electrical contact, (b) tip and sample are in electrical contact, and (c) a bias voltage (V_{DC}) is applied between tip and sample to compensate the CPD and the electrostatic force. E_v is the vacuum energy level. E_{Fs} and E_{Ft} are Fermi energy levels of the sample and tip, respectively.

2.4.4 Minimum detectable CPD by KPFM

In AFM measurement, a frequency shift (Δf) and an amplitude variation (ΔA) of the cantilever vibration due to the energy dissipation are given by

$$\Delta f = -\frac{f_0 F_c}{2kA} \quad (2.57)$$

$$\Delta A = -\frac{Q F_d}{k}, \quad (2.58)$$

where f_0 , k , Q and A are the resonant frequency, the spring constant, the quality factor and the oscillation amplitude of the cantilever, respectively. F_c and F_d are the tip-sample conservative interactions and dissipative interactions, respectively.

Therefore, the minimum detectable force for conservative interaction and that for dissipative interaction are given by

$$\delta F_c = -\frac{2kA\delta f}{f_0} \quad (2.59)$$

$$\delta F_d = \frac{k\delta A}{Q} \quad (2.60)$$

Here, δf and δA are the minimum detectable frequency and amplitude, respectively.

For typical AFM measurements in UHV, the δf and δA are given by [24]

$$\delta f = \frac{\sqrt{12f_m n_{ds} \sqrt{B}}}{\pi A} \quad (2.61)$$

$$\delta A = n_{ds} \sqrt{B}, \quad (2.62)$$

here the n_{ds} , B , f_m are the deflection sensor noise, bandwidth of the lock in amplifier and the modulation frequency, respectively. Therefore, δF_c and δF_d are obtained as:

$$\delta F_c = \frac{4\sqrt{3}f_m n_{ds} \sqrt{B}}{\pi f_1} \quad (2.63)$$

$$\delta F_d = \frac{kn_{ds} \sqrt{B}}{Q} \quad (2.64)$$

The conservative electrostatic force (F_{esc}) is given by

$$\delta F_d = \frac{kn_{ds} \sqrt{B}}{Q} \quad (2.65)$$

$$F_{esc} = \frac{\pi \epsilon_0 R A}{z_{t0}^2} V_{ts}^2, \quad (2.66)$$

while the dissipative electrostatic force (F_{esc}) is zero.

The ω_m component of the frequency shift (Δf_m) induced by the electrostatic interaction is given by

$$\Delta f_m = \frac{\pi \varepsilon_0 R f_0 V_{ac}}{k z_{t0}^2} V_{AC} V_{DC}, \quad (2.67)$$

from equation $\Delta f = -f_0 F_{esc} / (2kA)$, minimum detectable CPD in FM-KPFM can be described [10],

$$\delta V_{CPD-FM} = \frac{2\sqrt{6} k_1 z_{t0}^2}{\pi^2 \varepsilon_0 R A V_{AC}} \frac{f_m}{f_{01}} n_{ds} \sqrt{B} \quad (2.68)$$

2.4.5 Origin of the LCPD

It has been a long time since KPFM made it possible to measure the contact potential difference (CPD) between tip and sample so that to observe the potential of various surfaces. The CPD is a physical quantity defined by the macroscopic work function, but in recent years, changes in the contact potential difference at the atomic level (microscopic) have been observed and clarified on semiconductor surfaces [11], insulator surfaces [12], metal atoms (clusters) [13-15], polar molecules [16,17] and charge transfer complexes [18]. The origin of this local contact potential difference (LCPD) is still not well understood and is being investigated by many researchers. In this section, we will introduce the mentioned origins of LCPD.

1. Charge transfer effects

■ Charge transfer from subsurface

When metal atoms (clusters) or molecules are adsorbed on a semiconductor or metal surface covered with an insulating film, charge transfer occurs between the surface and the adsorbed material through the insulating film. It is known that charge transfer could induce the change of work function of the sample.

As shown in Figure 2.9, when the charge is transferred from the adsorbate to the surface (when the charge in the adsorbate is insufficient), an electric dipole moment is generated in the direction from the surface to the adsorbate. This dipole moment decreases the work function of the sample. On the other hand, when the charge moves from the surface to the adsorbent (when there is excess charge in the adsorbent), an electric dipole moment is generated in the direction from the adsorbent to the surface, and the work function increases. Therefore, when the adsorbent is positively charged, the contact potential difference decreases. On the other hand, when the adsorbate is negatively charged, the contact potential difference increases.

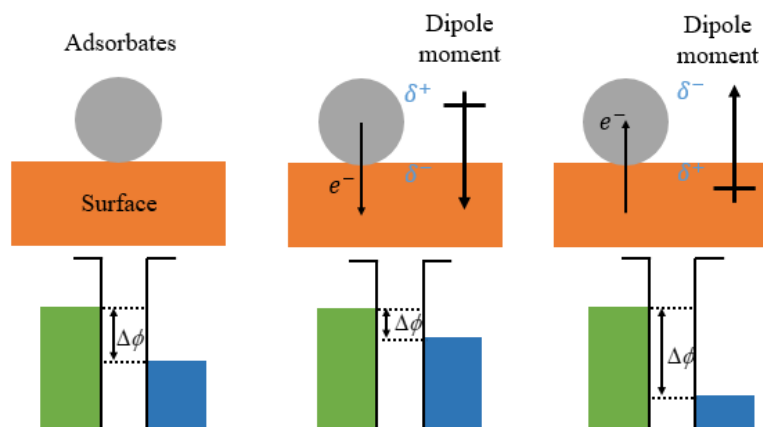


Figure 2.9 Model of change in contact potential difference due to charge transfer between adsorbates and surface.

■ Charge transfer from tip apex

L.Gross and his group have distinguished positively charged, neutral, and negatively charged Au atoms by LCPD shifted. The single electron charging or discharging of gold atom could be induced by increasing the force on the AFM tip by few piconewtons. In addition, charging the oxygen adatom by the single electron charge by applied electric field on the TiO₂ surface.

2. The effect of charge redistribution caused by the approach of the tip

When an active tip apex is brought into contact with the surface, the strong overlap of the electron wave function between the tip apex atom and the surface atoms results in the generation of polarization charges. This charge redistribution on the surface side is induced by the tip apex and is treated as an induced dipole moment. The presence of this polarization charge is thought to enhance the contrast in LCPD. Meanwhile, the existence of the induced dipole moment has been reported by S. Sadewasser's group as an example of a local chemical potential change observed as LCPD. [20] However, the LCPD change of the surface could not be attributed to the dipole moment only, because the Si dangling bond in the tip apex is active.

3. Effects of permanent dipole and multipole moments in molecules

Recently, charge transfer complexes and organometallic complexes have been investigated due to the increasing demand for organic molecular electronics. Schuler et al. and Bing Kai et al. have reported the observation of LCPD of these molecules by KPFM [16,18].

Schuler and co-workers have investigated the LCPD in an electron-donating and an electron-

accepting molecule as shown in Figure 2.12. It has been reported that the LCPD has a distance dependence. In the long range, the LCPD reflects the effect of the dipole moment between the donor and acceptor in the molecule. However, at distances similar to the size of the molecule, the tip is expected to reflect not only the rough charge distribution but also the three-dimensional charge distribution in the molecule and the electric field influenced by higher-order multipoles due to the charge in each atom of the molecule. At near distances, it could reflect the effect of Pauli's repulsion (see below).

LCPD images of metal phthalocyanines (MPcs), which form a variety of organometallic complexes, have also been observed by BingKai et al. MPcs is not a planar molecule, but has a structure in which the metal and oxygen atoms are ejected, and therefore has a permanent dipole moment as shown in Figure 2.12. This permanent dipole moment is thought to change the work function of the surface, which is observed by LCPD contrast. When the permanent dipole moment is toward the surface, LCPD increases (work function increases), while when the permanent dipole moment is toward the vacuum, the LCPD decreases (work function decreases).

It can be noticed that the LCPD could reflect the charge distribution inside the molecule.

2.5 Conclusion

In this section, we describe the principle of AFM. Firstly, the various interaction forces between the tip and the sample are described in section 2.2, the working principle of AFM is explained in section 2.3, and the principle of KPFM is described in section 2.4. Finally, the origin of the LCPD was clarified by various previous studies.

Chapter 3 Setup of room temperature UHV AFM

3.1 Introduction

In this chapter, we introduce the equipment and circuit configuration of the room temperature AFM used in this study. In section 3.2, the equipment of Ultra high vacuum (UHV) including the three vacuum chambers and the vacuum pump will be described. In section 3.3, we describe the design and mechanism of the AFM unit including stages and deflection detection part. In section 3.4, we describe the preparation method of sample and cantilever that need to be transferred into observation main chamber. In section 3.5, the operation circuit for detection of frequency shift are presented. In section 3.6, we show principle of electron beam evaporator and process of evaporation. Finally, we summarized this chapter.

3.2 Equipment of UHV nc-AFM

In the follow, we present our home-built construction of AFM. It mainly assembled by the three vacuum chambers with gate break to separate the vacuum chamber from each other, which could be seen picture in the Figure 3.1 and schematic diagram correspondingly in the Figure 3.2.

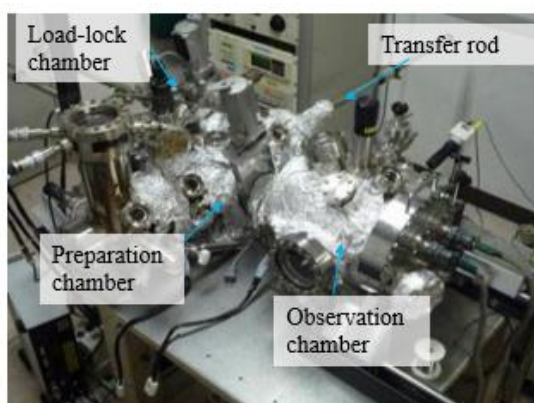


Figure 3.1 Room temperature UHV nc-AFM system.

Load-lock chamber

The load-lock chamber is used to install a new sample or cantilever into the ultra-high vacuum preparation chamber and main observation chambers step further. The load-lock chamber is separated

from the preparation chamber by a gate break, which allows the introduction of samples and cantilevers without decreasing the vacuum level in the preparation chamber. After increasing vacuum level of the load-lock chamber by turbo molecular pump, rotary pump combined with baking, we could transfer the samples and cantilevers to the preparation chamber by the transfer rod under high vacuum. A high vacuum of 10^{-10} to 10^{-11} Torr can be maintained by combination of a rotary pump and a turbo molecular pump.

Sample preparation chamber

The preparation chamber is equipped to clean the sample and the tip apex as required. An electric current feeder is installed in chamber, which allows annealing, flashing and degassing for samples and tip apex. An argon ion gun is installed, in which the argon ion is ionized by bombarding it with hot electrons and then bombarded with a voltage to the target to remove the impurities from tip apex and sample surface, such as oxide film. In order to oxidized the surface, especially alumina thin film in this study, an oxygen gas cylinder is installed on the chamber. For the investigation of the nanoparticle properties, the electron beam evaporator is also installed on the chamber, which designed for evaporation from rods. Finally, the sample and tip processed in the preparation room can be transferred to the observation main chamber in vacuum by the transfer rod. A combination ion pump and titanium sublimation pump are installed at the bottom of the preparation chamber to maintain an ultra-high vacuum in the 10^{-11} Torr level.

Observation main chamber

The main chamber is equipped with an AFM unit for measurements in the center. The unit is installed by a two-stage spring-loaded vibration-isolation system with different spring constants and a magnetic vibration-isolation system to reduce the noise caused by floor and acoustic vibrations during measurements. In addition, a carbon monoxide gas cylinder is installed in the chamber, allowing free exposure of CO gas during the measurement to elucidate the catalytic mechanism. A gate break between the preparation chamber and the observation main chamber prevents the gas coming from sample and tip preparations. Finally, the observation chamber could be maintained ultra-high vacuum in 10^{-11} Torr level by equipped with ion pump and titanium sublimation pump. Because of the CO molecule exposure during scanning, a turbo molecular pump combined with a rotary pump are also installed in the chamber.

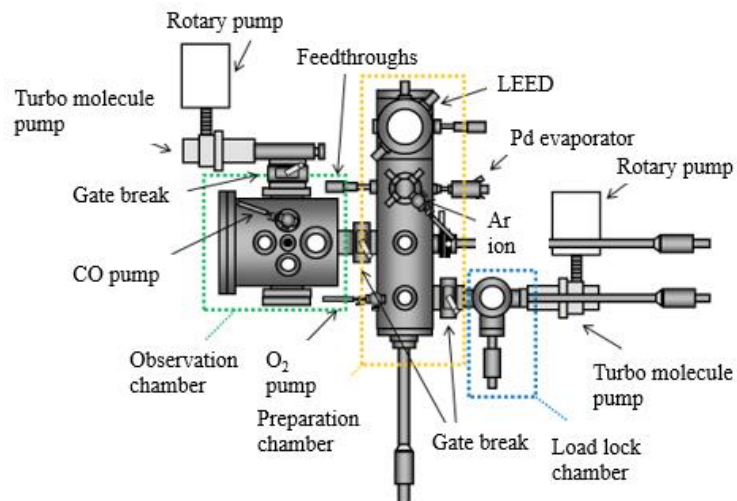


Figure 3.2 Schematic diagram of the room-temperature AFM (top view).

The UHV pumping system is described below. In order to observe the atomic structure of surface in a stable manner, it is necessary to keep the sample surface and tip clean. Therefore, the pumping system is very important. Firstly, a rotary pump and a turbo-molecular pump (pumping rate: 50 l/sec) in the load lock chamber are used for roughing pumping. The evacuation to ultra-high vacuum is carried out by baking for several days (120°C in the observation main chamber and 150-200°C in the other chamber) to reach a high vacuum state of 10^{-9} to 10^{-10} Torr. After that, the UHV is maintained by a combination pump (ion pump with a displacement of 70 l/sec and a titanium sublimation pump with a displacement of 1600 l/sec) that located under the observation main and preparation chamber. The UHV achieved in this pumping system reaches less than 3×10^{-11} Torr.

3.3 AFM unit

Top view of the picture and schematic diagram of the AFM unit in the Figure 3.3 used in this study. The AFM unit consists of the sample stage, cantilever stage and the detection system.

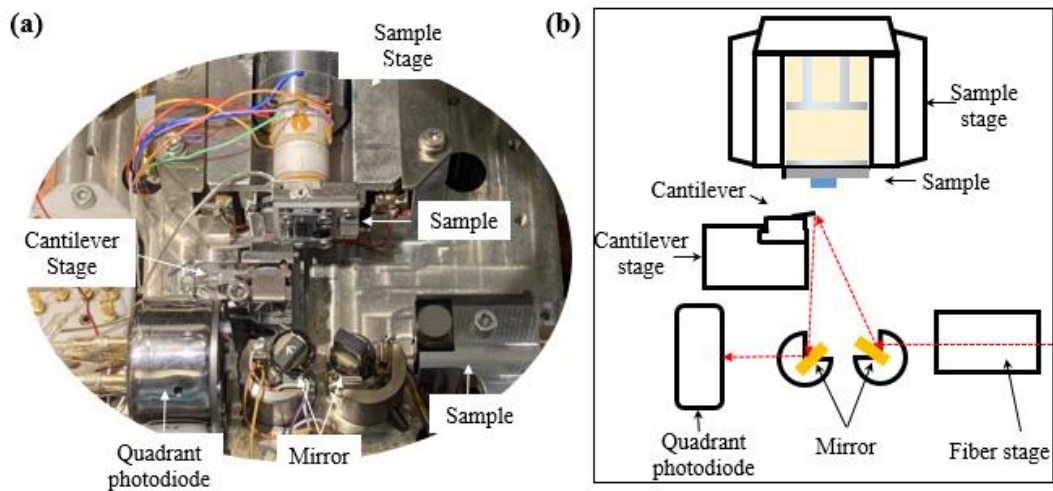


Figure 3.3 Top view of the AFM unit picture (a) and schematic diagram (b).

3.3.1 Sample stage and cantilever stage

● Sample stage

The sample could be introduced stably in the approaching stage by the magnitude. The approaching stage motion are designed with stick-slip actuation technology [1]. The stage with a sapphire sticked is mounted on top of the shear piezoelectric element with a ruby ball for isolation, as shown in the Figure 3.4 (a). When the voltage is gradually applied to the piezo, the static frictional force between the stage and the piezo piezoelectric element is sufficiently high so that the piezo is distorted and the stage moves accordingly. This is called stick. Then, when the voltage is decreased rapidly so that the piezo piezoelectric element returns to its original shape, the stage comes to stay in the position it has moved because of the slippage between the stage and the piezo piezoelectric element. This is called slip. By repeating this stick-slip operation, it is possible to move the stage with high precision. The stage will move forward or backward as the input of the saw tooth voltage.

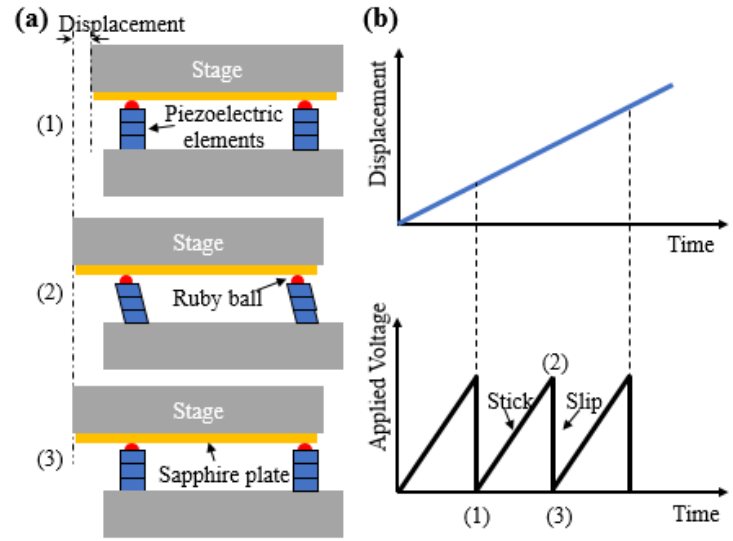


Figure 3.4 Operating mechanism of the stick-slip actuator. (a) The schematic of stick-slip setup. (b) The stage displacement dependent on the applied voltage vs time.

Schematic structure of piezoelectric tube is shown in Figure 3.5(a) top view and (b) cutaway view. The piezo (gray) are attached by the inner and outer electrodes (yellow), including +x, -x, +y, -y that opposite to each other on the outer and inner -z and outer +z. The inner continuous electrode is connected to the ground and the bias voltage is applied to the outside +z electrode, so that electric field direction goes from inside to outside, which could induce the polarization. The piezo in z direction extend, therefore tube could be retracted or approached shown in Figure 3.5 (c). For the x-y direction motion, one side of the tube expands, and the opposite side shrink, resulting in bending motion shown in Figure 3.5 (d). Because the outer electrodes are connected to bias voltages with opposite polarity.

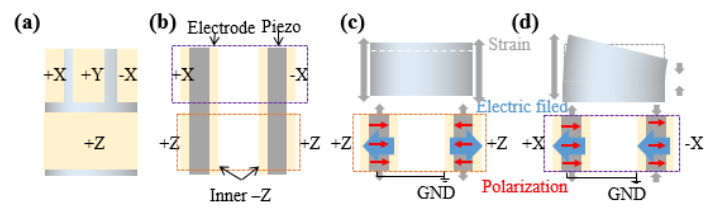


Figure 3.5 Schematic of the tube scanner, (a) top view, (b) cutaway view. Actuation and sensing (c) in the z and (d) in the x direction of the piezoelectric tube.

The laser module, photodiode and mirror used for optical alignment can be moved freely by means of a piezoelectric sliding oscillator. The laser module and the photodiode are inertially driven, as is the sample stage. The mirror has three sliding crystals in contact with the mirror ball, and the angle of the

mirror can be freely adjusted by applying a voltage to the three crystals.

● Cantilever stage

The cantilever stage has a piezoelectric transducer to resonate the cantilever, as shown in Figure 3.6. The piezoelectric transducer is fixed using an insulation epoxy adhesive. To fix the cantilever, a steel plate is placed on top of the cantilever and fixed with screws, and also graphite paste is used. There is also a terminal consisting of three wire electrodes, two of which are used to excite the cantilever and the other for the voltage signal.

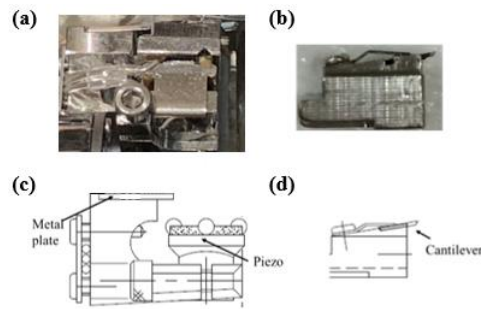


Figure 3.6 (a) Picture and (c) schematic diagram of the cantilever stage and cantilever holder (b) and (d).

3.3.2 Deflection detection system

■ Theory of optical beam deflection detection

A wide variety of deflection detection methods of the cantilever have been used, such as piezoelectric force sensor [2,3], optical beam deflection detection (OBD) [4] and optical interferometer detection [5]. In the follow, we describe the theory of the optical beam deflection detection system as shown in the Figure 3.7 [6,7]. The displacement of cantilever could be related with the cantilever deflection angle as follow

$$\Delta\theta = \frac{3}{2} \frac{\Delta z}{l} \quad (3.1),$$

where l is the length of the cantilever. The cantilever deflection angle gives rise to displacement of laser spot on the photodiode, the equation is shown as follow

$$\Delta a = 2\Delta\theta * s \quad (3.2),$$

substituting the equation 3.1 into 3.2, the expression is written as below

$$\Delta a = 3 \frac{s}{l} \Delta z \quad (3.3),$$

here, parameter s is the distance from the laser point on the second mirror to the photodiode. The laser point position on the photodiode induces different photocurrent, if the laser spot assumed as a square, the difference of the photocurrents could be expressed as

$$\Delta i_1 = P\eta \frac{2}{a} \Delta\alpha \quad (3.4),$$

here, η , P , and a are efficiency of the light-to-current conversion for the photodiode, total power of the laser beam irradiated onto the photodiode, and diameter of the laser spot on the photodiode, respectively.

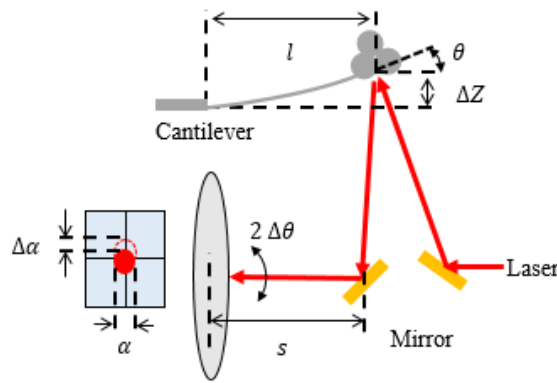


Figure 3.7 Schematic diagram of the optical beam deflection detection method.

■ Detection system circuit

The optical beam deflection detection system used in this study consists of laser beam with a wavelength of 550 nm, a mirror to propagate the laser light, a quadruple photodiode for detection of the light, and an I/V converter to convert the photodiode current into the voltage. The schematic diagram is shown in Figure 3.8. The laser beam transferred though fiber is reflected by the mirror on the laser side, and reach to the back of the cantilever. The quadruple photodiode determines the amount of laser by each photodiode (P1, P2, P3, P4). The amount of light detected at the upper photodiode is $A(P1+P2)$ and the amount of light detected at the lower photodiode is $B(P3+P4)$, then, the deflection of the cantilever is detected as a displacement signal $A-B$ [4,8].

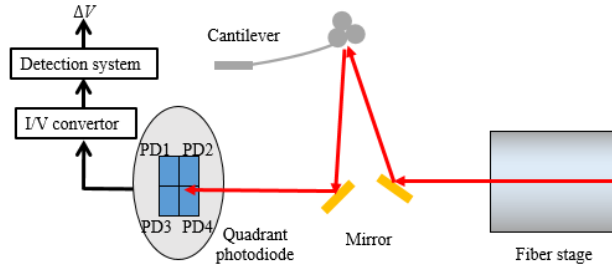


Figure 3.8 Schematic diagram of the optical beam deflection detection method.

3.4 Sample and cantilever preparation method

3.4.1 Sample fix method

The sample fix method depends on the different heat treatment. Usually, the sample could be sandwiched between a tantalum (Ta) plate on the lower side and a molybdenum (Mo) plate on the upper side, such as the conductive Si specimens. However, the direct electric heating causes variation in the current value when the sample is annealed at the same temperature. Therefore, we adapt indirect current heating method, shown in the Figure 3.9. In this case, the tantalum foil covered with insulating sheet (PBN) used as a heating part. Before installing the sample, another PBN is placed on the bottom to isolate each other. In order to insulate the molybdenum plate and the sample, one PBN is placed on one side of the sample surface, so that it is possible to measure the bias on the surface. According to the size of sample holder, we use the size of the sample is $10.5 \times 2.5 \times 0.5 \text{ mm}^3$ and the total height of the holder is around 0.5 mm.

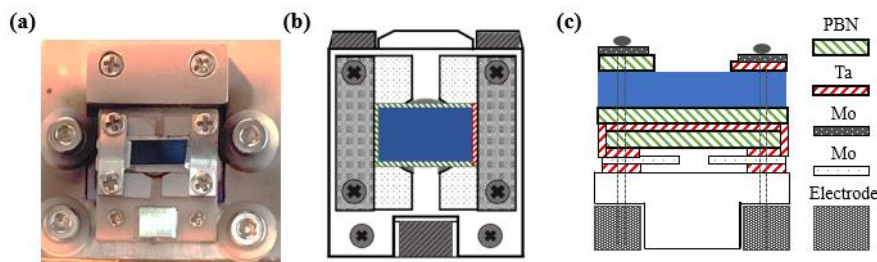


Figure 3.9 (a) Photo and (b, c) schematic representation of the sample holder in top view and side view. Blue: NiAl(110) sample.

3.4.2 Sample preparation method

We can obtain the alumina thin films by oxidizing the clean NiAl(110) surface. In the follow, the

preparation procedures are presented.

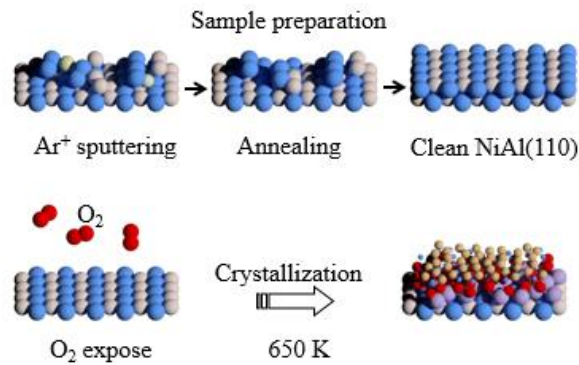


Figure 3.10 Preparation method of alumina thin film on NiAl(110) surface.

1. Clean NiAl(110) surface

Since the NiAl(110) surface has been stored in air, impurities such as oxygen and nitrogen are deposited on the surface, so it is necessary to do degas. The temperature is slowly raised to 1000°C, keeping the vacuum does not exceed 1.0×10^{-8} torr and annealing for 2 hours after reaching 1000°C. Then clean surface can be got by repeating the cycle of Ar⁺ sputtering (2.0×10^{-6} torr) and annealing respectively, the parameter is shown as follow:

Ar⁺ sputtering: emission = 20 mA, ion energy = 1.2 or 2.5 keV, time = 20 min

Annealing: temperature = 1000 °C, time = 20 min

The ion energy of Ar⁺ sputtering is set to 2.5 keV for the first 5 cycles followed by 2 keV for 10 cycles.

Figure 3.11 shows the AFM images of NiAl(110) surface according to the number of cycles. In Figure 3.11(a), after 5 cycles, a flat NiAl(110) surface could not be obtained, and in Figure 3.11(b), after 8 cycles, the flat NiAl(110) surface and the step structure could be confirmed for the first time. Therefore, a minimum of 15 cycles of Ar⁺ sputtering and annealing is required for a new sample treatment.

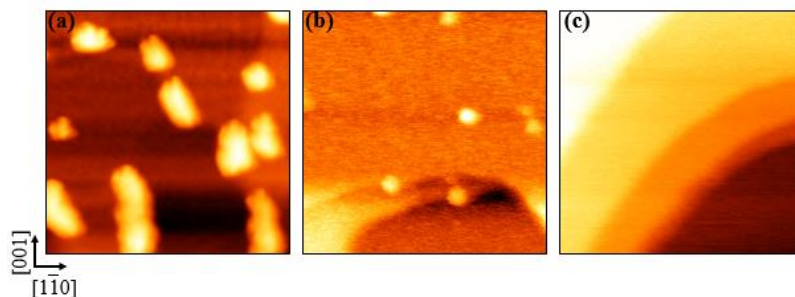


Figure 3.11 AFM images of NiAl(110) surface. Images after (a) 5 cycles, (b) 8 cycles and (c) 12

cycles. $f_0 = 1.13$ MHz, $Q = 2900$, $A = 800$ pm, $V = 0$ V, size of 100×50 nm².

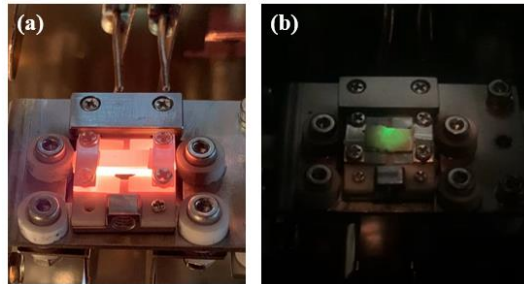


Figure 3.12 (a) Photo of the surface when annealing. (b) Photo of the Ar⁺ sputtering on the fluorescent plate.

In our experiment, the Ar ion-sputtering system is used to prepare the clean tip and sample surface, which is schematically presented in Figure 3.13.

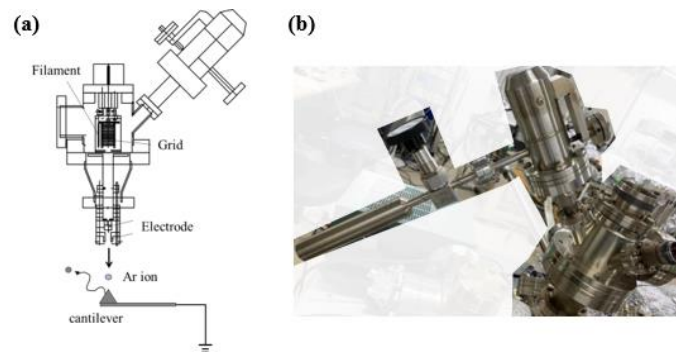


Figure 3.13 (a) Sketch of sputtering ion gun. (b) Photo of ion gun with argon.

2. Grow alumina thin film on NiAl(110) surface

Once the cleaned NiAl(110) surface has been obtained, we have to deal with the surface before next experiments. Usually, three cycles of Ar⁺ sputtering and annealing are carried out again under the conditions: ion energy = 2.5 keV for the first sputtering only, then ion energy = 2 keV. After the third annealing cycle, the temperature is continuously lowered to 400°C and the sample is exposed to oxygen gas. The oxygen gas exposure volume is 1200 L, $P_{\text{oxygen}} = 2.0 \times 10^{-6}$ Torr for 10 minutes. After the exposure, the temperature of the sample is raised to 880 °C that sub-annealed for 4 minutes, and then dropped to 0 °C to produce alumina thin film [9]. It is important that the temperature is changed at a rate of 1°C/1sec. To get clean surface, sputter energy is very important in this study. The large area of

alumina surface is shown in the Figure 3.14, including the various line defects.

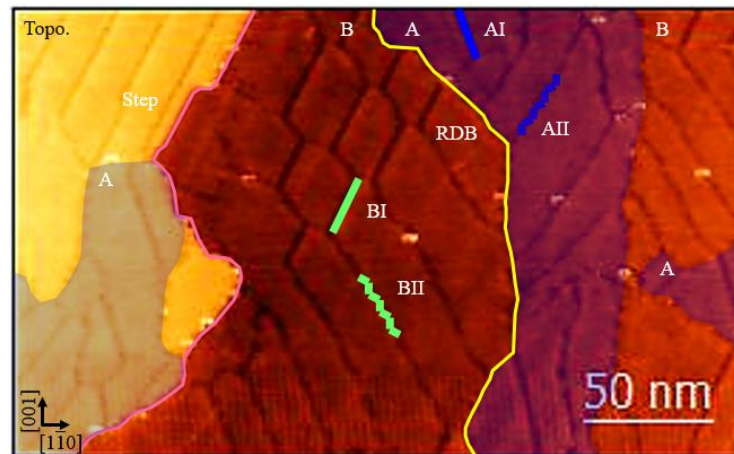


Figure 3.14 Large area of AFM images of alumina (Al₂O₃) on NiAl(110) surface.

3.4.3 Cantilever preparation method

As an AFM sensor, a commercially available Ir-coated cantilever (Nano sensors SD-T10L100, $f_0 \sim 800$ kHz and 1.13 MHz) was used. The cantilever is fixed to a silicon support chip which can be seen in the sketch of the AFM probe assembly shown in the Figure 3.15 (a). The support chip as an integral part of the probe is designed for manipulating the probe and fixing it to the cantilever holder. Figure 3.15 (b) show the TEM images of the cantilever and tip apex. The diameter of the tip apex is about 5 nm.

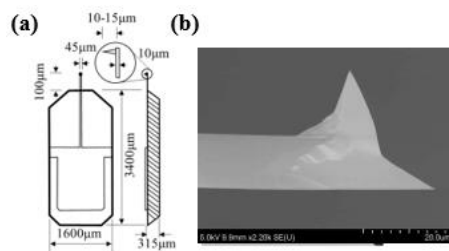


Figure 3.15 (a) The sketch of the AFM probe assembly and (b) the TEM image of the part of cantilever and tip apex.

Before the AFM measurements, the Si cantilever is cleaned by annealing and Ar ion sputtering at room temperature to remove the contaminants. For the metal coated cantilever, there is no need for the above preparation, because the sharp tip apex could be got by the manipulations on the surface.

3.5 Operation circuit

The circuit configuration of the FM-AFM/FM-KPFM with feedback used in this study is shown in Figure 3.16. The displacement of the cantilever is detected by a photodiode, and the AGC (Auto Gain Control) and PLL (Phase Locked Loop) circuits are used to control the excitation and detect the frequency shift. In this study, OC4 is used by NANONIS for FM detection circuit. In the following, we briefly describe the circuits used in this study.

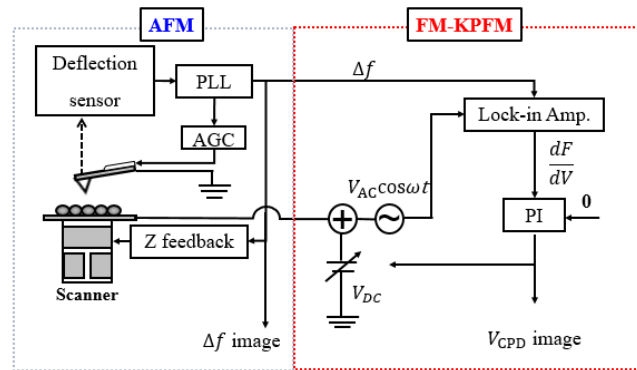


Figure 3.16 Circuit configuration of FM-AFM and FM-KPFM with feedback.

3.5.1 AGC circuit

The AGC circuit is a feedback circuit which is necessary to keep the vibration amplitude of the cantilever constant. The AC signal detected from the photodiode is input to the lock-in amplifier in the PLL circuit, and the amplitude detected by the lock-in amplifier is used as the vibration amplitude signal of the cantilever, and the feedback control is performed to make this signal equal to the amplitude (set point) to be vibrated by PI control. The vibration amplitude of the cantilever is controlled by PI control.

3.5.2 PLL circuit

The PLL circuit detects the frequency shift from the AC signal output from the photodiode and optimizes the vibration frequency of the cantilever to the resonance frequency. The signal from the photodiode is used for two purposes by the lock-in amplifier in the PLL circuit. When the cantilever is excited at its resonant frequency, one of the signal is input to the NCO (Numerical Controlled Oscillator) to optimise the vibration frequency of the cantilever to its resonant frequency, as the vibration signal is 90° out of phase with the excitation signal. The resonant frequency is then optimised by making sure that the difference between the phase of the cantilever vibration signal and the phase of the excitation

signal is always -90° . The other signal matches the frequency shift, so it is output to the feedback operation circuit and the FM-KPFM circuit.

3.5.3 FM-AFM/FM-KPFM circuit

The red line in Figure 3.16 shows the FM-KPFM circuit. As our KPFM setup applies an AC voltage (V_{AC}) at frequency ω as well as a DC voltage (V_{DC}) to the sample, V_{DC} nullifies the f_{AC} component of oscillating electrical forces, providing V_{CPD} between the tip and the sample surface. In our case, the local contact potential difference (LCPD) voltage can be determined with a feedback loop using KPFM.

3.6 Electron beam evaporator

3.6.1 Principle of the evaporator

The evaporation system used in this study is an EFM 3 manufactured by Omicron [10]. The principle of operation of the vacuum deposition source is described below.

The schematic diagram of the evaporation source is shown in Figure 3.17. A high voltage (600 V in this case) is applied to the evaporation material side, and the thermal electrons generated from the filament body collide with the heated evaporation material. This causes the temperature of the evaporation material to rise and evaporate. The evaporated material reaches the substrate and forms a thin film. A part of the evaporated material is ionized and reaches the flux monitor shown in Figure 3.17. The amount of evaporated material can be estimated from the value of the flux monitor because the weak current flowing at this time is proportional to the amount of evaporated material. During the evaporation process, the gas released from the wall is suppressed by water-cooling, which makes it possible to evaporate in an ultra-high vacuum.

In this study, the crucible deposition method is used. The vacuum deposition theory of crucible deposition is briefly explained below. We consider a model in which the evaporation source is made of a cylindrical object such as a crucible, and evaporated molecules are ejected from a hole in the top of the crucible. The total mass evaporated in a certain time is Me , and the evaporated mass contained in the solid angle $d\omega$ in the direction of the angle φ with the plane normal of the hole is

$$dMe = Me \cos\varphi d\omega/\pi, \quad (3.5)$$

where the evaporated mass attached per unit area of a surface at a distance r from the evaporation source and with the direction of the evaporated molecules and the normal inclined by θ is

$$md = sMe \cos \varphi \cos \theta / \pi r^2 \quad (3.6),$$

and is given by where s is the proportion of particles that adhere to the substrate out of the particles evaporated and ejected, which is called the adhesion coefficient.

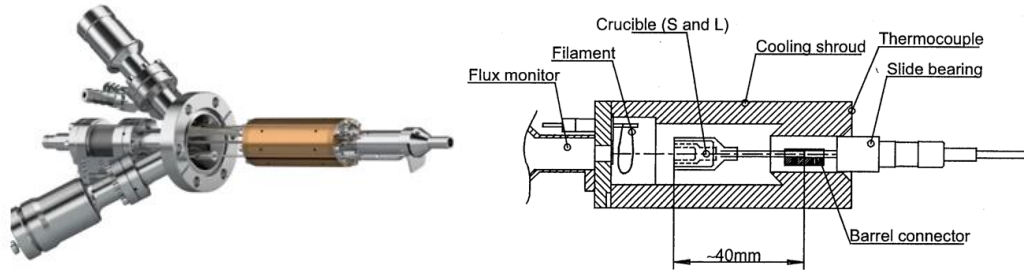


Figure 3.17 Photo and schematic diagram of the deposition source (EFM 3).

3.6.2 Process of the evaporation

Degas with evaporant heating:

- Turn the high voltage to about 200 V.
- Gradually increase the current until emission starts typically at 1.8 A filament current). Set to an emission current of about 5 mA (1 W heating power).
- The temperature of the cooling shroud will rise faster during degassing than without a crucible.
- Degas the evaporator until the desired shroud temperature is reached. The overheat protection of the EVCs will switch of the heating power, when exceeding the over temperature (preset 300°C for all EVC)

After sufficient degassing start with evaporation:

- Turn on the water cooling.
- Set the HV to about 600 V to 800 V and the filament current to about 1.5 A.
- Slowly increase the filament current until emission starts and the flux monitor indicates an ion flux (positive polarity) in the 1 nA range.

The general parameters on the controller for the deposition source were:

emission = 40 mA, flux = 0.02 nA, voltage = 600 V, temperature = 20-50 °C, time = 1-3 min.

The large area of alumina surface with Pd nanoparticles is shown in the Figure 3.18. The Pd nanocluster shown as the spherical in the AFM images.

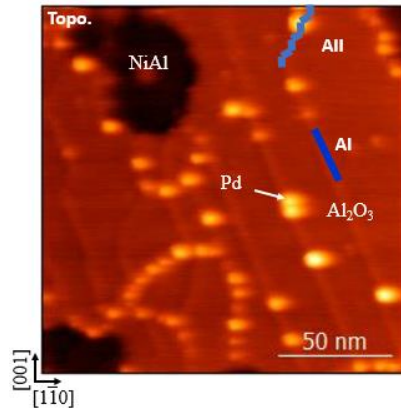


Figure 3.18 The large area of AFM image of Pd nanoparticles on $\text{Al}_2\text{O}_3/\text{NiAl}(110)$ surface.

3.7 Conclusion

In this chapter, we introduced the equipment of UHV nc-AFM in detail. Next, the presentation of the AFM unit including sample and cantilever stage, and the deflection system. Furthermore, the sample fix method depending on sample type is explained, and the NiAl(110), alumina surface and cantilever preparation method is also introduced. Followed by presentation of the operation circuit, especially the FM-AFM and FM-KPFM circuit. Finally, the evaporation principle and process are clarified.

Chapter 4 Research about Pd NPs on alumina thin film

4.1 Introduction

In this chapter, we generally introduce the basic physical properties of the alumina thin films used in this study, including the unit cell and line defect structure properties. In section 4.3, we clarify the investigations about the charge state of metal atom and NPs on $\text{Al}_2\text{O}_3/\text{NiAl}(110)$ surface. In section 4.4, investigation of CO reactivity on the metal NPs is described, additionally, the correlation of the CO Lewis structure and orbital interaction diagram. In section 4.4, we describe the structure of oxygen and its complex formation with transition metals. In section 4.5, we introduce the investigations of oxygen reactivity on Pd NPs. In the final, we give the summary.

4.2 $\text{Al}_2\text{O}_3/\text{NiAl}(110)$ surface

Alumina thin films are obtained by oxidation of NiAl(110) surfaces. In this section we describe in detail the structure and properties of alumina thin films combined experiments and calculation.

4.2.1 Unit cell of alumina

The alumina film is formed on the NiAl(110) surface, where the NiAl single crystal has the body-centered cubic type structure shown in Figure 4.1(a) and the NiAl(110) surface has the structure shown in Figure 4.1(b).

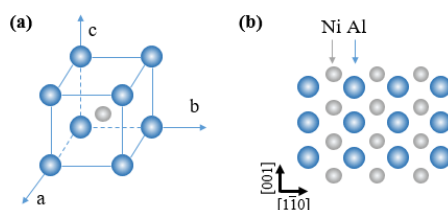


Figure 4.1 Body-centered cubic type structure shown in (a) and the NiAl(110) surface in (b).

In the alumina crystal structure, O atoms are arranged in hexagonal close-packed planes, and the Al atoms occupy two out of three octahedral interstitial sites between the oxygen planes, forming a buckled honeycomb lattice.

In general alumina, the Al atom forms a hexagonal close-packed structure, but the Al_i atom shares

one electron with the Ni atom, so it loses one valence electron to bond with the O_i atom, so the Al_i atom has two valence electrons (Al^{+2}). This means that the Al_i atom cannot form a hexagonal close-packed structure and forms a pentagonal or heptagonal structure as shown above. This means that the chemical formula of the alumina thin film is $Al_4O_6Al_6O_7$, as opposed to Al_2O_3 , which is the usual formula for alumina, and if the 16 unit cells on the NiAl(110) surface are covered and the number of valence electrons of each atom in the alumina thin film is also described, the overall stoichiometry is $4(Al^{+24}O^{-26}Al^{+36}O^{-27})$ [1].

Bulk alumina, which is an insulating material, cannot be used for experiments using electrons, such as STM and TEM. However, the thickness of the alumina film is about 5 Å [2], which can be used for the above experiments because of electron tunneling properties.

The specific picked up of the tip apex affect the AFM image contrast, as reported in previous research. In the oxygen mode, the oxygen atom of the alumina is bright in the case of a positive tip apex. As shown in the AFM images, the red spot indicates the structure of the oxygen that consistent with the model proposed by Kresse group [2]. In addition, in the aluminum mode, the aluminum atom of the alumina is bright in the case of a negative tip apex used for scanning. As shown in the AFM images, the green and blue spot indicate the structure of the aluminum atom that the model proposed by our group [3].

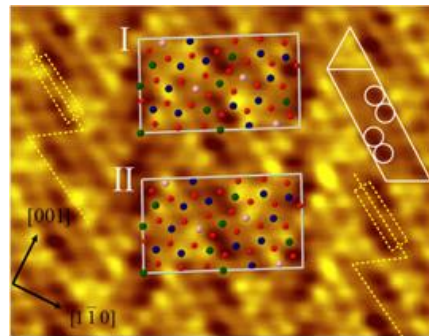

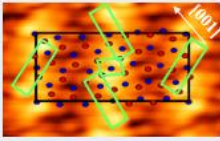

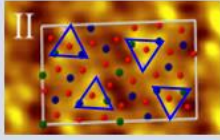


Figure 4.2 NC-AFM image of alumina-NiAl(110) surface with two possible interpretations (I and II) based on an atomic model [2] for more details see the text. The salient protrusions and depressions are highlighted in white and yellow. Only oxygen and aluminum atoms are shown [3].

In our group, both oxygen and aluminum atoms as the protrusion contrast can be obtained in our system. We clarify the atomic resolution of well-ordered alumina film with different tip apex as following table. It is concluded that we can distinguish the surface and tip apex condition by the AFM images.

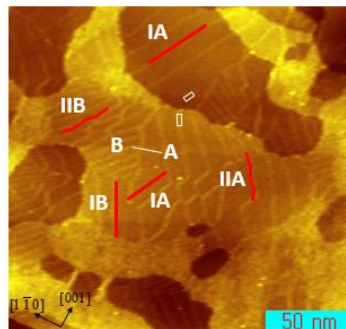
Table 4.1 AFM images contrast of the alumina thin film surface with different tip apex.

Mode	Tip apex	AFM image
		Unit
O: bright Al: dark		 <i>T. König, Nanotechnol. 2, 1–14 (2011)</i>
O: dark Al: bright		 <i>Li, Y. J. Nanotechnology 2015, 26, 505704</i>

4.2.2 Structure of surface defect

Alumina thin films contain a very characteristic defect structure. It has been reported that metal particles can be adsorbed on these defects and are thought to play an important role in catalytic reactions [4]. In this section, we clarify and describe the defect structure of alumina thin film.

As shown in Figure 4.3, two domains are formed in the alumina thin film in the direction of $\pm 24^\circ$ inclined to [1-10] of NiAl(110) surface. Line defects are introduced to solve the mismatch between the thin film and the substrate, which produced by the existence of two mirrored domains and the distortion of the growth direction with NiAl(110). The line defects are named antiphase domain boundaries (APDBs) and reflection domain boundaries (RDBs) [2,3]. One type of the APDBs is named as straight line defect, which inserted parallel to the unit cell of the alumina thin film, another is named as zig-zag line defect, which inserted against the diagonal of the unit cell. In the following, straight line defect structure will be explained in detail.



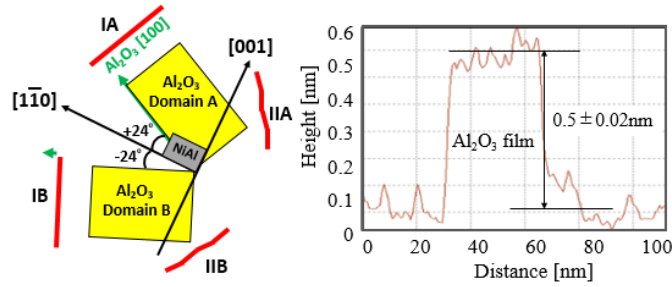


Figure 4.3 Growth direction of domains and APDB direction and structure in alumina thin films. IA and IB are linear defects, while IIA and IIB are zigzag defects from [3].

Straight line defect can be recognized by a space of 3.0 \AA inserted in the middle of the original unit cell of the alumina thin film, where the atoms forming the defect structure are inserted. This unit cell is large enough to cover 23 NiAl unit cells. Since the valence numbers of Al_i and Al_s are +2 and +3 respectively, the overall valence of the alumina film is $2 \times 19 + 3 \times 28 - 2 \times 60 = +2$. This means that one oxygen atom is missing [1,5], which represents the oxygen-deficiency structure.

The two electrons produced by the oxygen-deficiency structure should be incorporated into the $3p$ orbital (F center) of the Al atom, but in this case, they are transferred to the substrate, and the electron defect remains on the alumina surface. It has been demonstrated by the PDOS on the domain obtained by DFT calculations, and the PDOS on the alumina film containing APDB. Although the insertion of the defect would normally result in a very large change in the PDOS, the PDOS of the thin film containing the defect structure is only about 1 eV lower in the valence and conduction bands than the PDOS on the domain. It is concluded that the two electrons are transferred into NiAl(110) [5].

The stoichiometry of the straight line defect is $(\text{NiAl})_{\text{substrate}}^{2-} (\text{Al}_{19}\text{O}_{28}\text{Al}_{28}\text{O}_{32})^{2+}$, which is able to supply electrons from the NiAl(110) substrate, thus facilitating the adsorption of negatively charged atoms and clusters. The removal of electrons from the NiAl(110) substrate facilitates the adsorption of negatively charged atoms and clusters, and the adsorption of palladium particles on defects has been observed by STM [5].

Another defect structures also fascinate lots of research group. The step structure with a height of 0.2 nm, which is also found in alumina thin films. In the following, the step structure of the alumina thin film is described with reference by Heinke et al. [6]. The step structure of alumina thin films is formed during the oxidation and annealing of the NiAl(110) surface. In the step structure, the NiAl(110) surface is covered with a carpet-like oxide film as shown in reference [6]. Heinke group also show the contact

potential difference on the step of the alumina film is little bit lower than that on the surface, which suggests that electronic defects also exist on the step. Therefore, the adsorption of atoms and clusters is likely to occur even on the step.

Although there are lots of interesting results has been obtained, we still have curiosity on the different type of line defects, especially the various interaction with adsorbates.

4.3 Investigations of charge state of metal NPs on Al₂O₃/NiAl(110) surface

Metal oxide interfaces, dispersed metals on oxide supports play an essential part in many technological areas. It is clarified that defects and steps in the alumina thin film facilitate the adsorption of atoms and particles, which is active sites for the catalytic reaction. Nevertheless, there is still a lack of fundamental knowledge about the crucial properties of thin metal and small metal particles on oxide supports. However, a deeper understanding could help to improve the electronic, mechanical or catalytic performance of such systems. In this section the investigations of the metal atoms and nanoparticles on the insulating film are clarified.

4.3.1 Pd/Au atoms on Al₂O₃/NiAl(110) surface

Electronic properties of single Pd atoms, deposited on Al₂O₃/NiAl(110), have been characterized by scanning tunneling spectroscopy at 12 K and 50 K. Most of the Pd atoms adsorbed on the line defects sites at deposition temperature 50 K than 12 K. The conductivity spectra signature obviously reflects Pd atom binding properties at different adsorption sites on the thin film, correspondingly. According to the conductivity resonances, Pd atoms on large oxide domains show the peak around 3.0 V mainly. For the Pd atoms near domain boundaries, the spectra peak present around 2.5 V [4].

It is illustrated that defect sites provide higher binding energies, which modifies the Pd-oxide interaction and affects the electronic signature of Pd atoms. To support this assumption, they found that Pd atoms are prefer to trap on oxide defects at 50 K than at 12 K [4].

Even, they prefer to deduce defects effects on the adsorbed metal atom by comparing conductivity resonances of the Pd atoms on the thin film with Pd atoms on oxide defects. However, the shortage spectra of oxide defect are needed to compare with the spectra of Pd atoms on oxide defects.

The adsorption of Au on a thin alumina film on NiAl(110) has also been investigated experimentally and theoretically at 5-10 K. The Au monomers and dimers on alumina thin film are imaged as bright and dark contrast by the scanning tunneling microscopy. From the frontier orbitals of the monomer and

dimer, only the dimer LUMO shows up in the dI/dV spectra as a peak at 2.6 V. Although, the density-functional theory (DFT) shows the one occupied state and two occupied states for monomer and dimer Au, respectively. The occupied $s-d_{z^2}$ state comprised by the Au monomers bound to special Al_s sites, and $s-d_{z^2}$ orbitals of the two Au atoms hybridize to form the two occupied states dimer Au. The occupied states derive from the Au 6s orbital that is half filled in gas-phase Au and becomes doubly occupied on the oxide surface due to the charge transfer from the metal support. Therefore, it tends to conclude that the Au monomer, dimer and chains are negatively charged by calculation and spectroscopy results [7].

The occupied gold states are not revealed in the experiments. Therefore, the shortage of the spectroscopy is clear because the charging effects might induce an energy barrier that cannot be overcome.

Gold atom adsorbed on $Al_2O_3/NiAl(110)$ has been investigated by FM-dynamic force microscopy at low temperature. The Au atom preferable adsorption sites are present by the atomic resolution images, which show that wave trough-like depressions are preferred locations. According to the frequency shift-distance curves, the minimum value of frequency shift of Au atom and surface are different significantly, therefore, the available imaging set points lie within the ellipses [8].

4.3.2 Metal NPs on $Al_2O_3/NiAl(110)$ surface

The specific size of metal NPs show quantum effects and therefore can increase catalytic efficiency. As reported, the catalytic activities for CO oxidation at 273 K is shown as a function of Au particle size. The optimal catalytic size of Au particle on the alumina surface is around 1.5-5 nm in diameter [9].

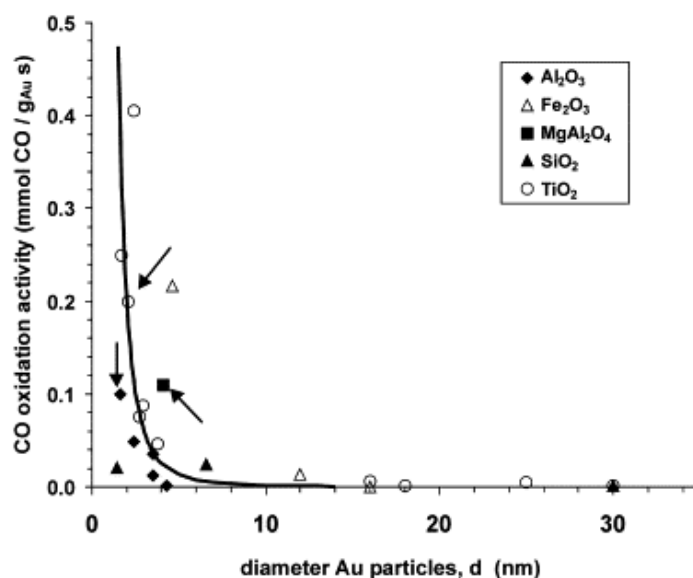


Figure 4.4 Reported catalytic activities (in $mmol/g_{Au}s$, left axis) for CO oxidation at 273 K as a

function of Au particle size (d , in nanometers) for different support materials [9].

The charge state of metal adsorbates also has an important effect on their catalytic properties, which is correlation with its size. In research on the CO oxidation activity by Infrared spectra combined with STM and calculations, it was found that as the catalyst size decreases, the cationic Pt atoms at the edges of a cluster become strongly correlated with the CO oxidation activity [10]. However, there are still a lack of the sub-atomic resolution experiments and charge state of Pt cluster illustrations.

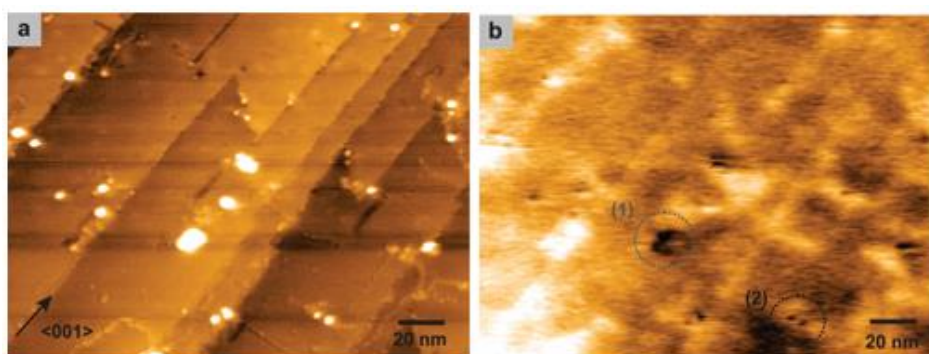


Figure 4.5 (a, b) Topographic image and Kelvin image of the Pd clusters on the MgO(001) surface [11].

In addition to characterizing the electrostatic properties, KPFM is a powerful tool for measuring charge state with atomic resolution as we discussed in the chapter 2. As shown in the Figure 5, the dark contrast of the Pd nanoclusters on the MgO(001) surface indicate it is positive charge. It is shown that the voltage difference equals the work function difference between MgO(001)/Mo and Pd. This result consistent with the MIES and UPS measurements [11].

At present, the atomic resolution of three dimensional Pd nanocluster and its electronic properties haven't been resolved by AFM experiment and KPFM at room temperature, which is important for understanding the size correlation with charge state in heterogeneous catalysis. In essence, theoretical calculations have shown that Pd nanoparticles of ~ 4 nm, the amount of edge and corner sites is the highest, resulting in a better activity. However, in the previous results, no direct experimental evidence has been proposed for the size dependence of the charge state of the Pd NPs on $\text{Al}_2\text{O}_3/\text{NiAl}(110)$. Therefore, the discussion about the mechanism of size dependent of charge state of Pd NPs and how line defects of alumina thin film affect the charge state are needed.

4.4 Investigations of CO reactivity on the metal NPs

This section describes the basic physical and chemical properties of carbon monoxide, its molecular orbitals and the characteristics of the complexes it forms with metals.

4.4.1 CO molecule Lewis structure and MO diagram

Carbon monoxide is known to have a triple bond in the Lewis structure [12]. Figure 4.6 shows the carbon monoxide orbital interaction diagram correlation with the Lewis structure. Lowest orbital of CO is the σ_s where the electron comes from 2s orbital of C and O atom, the orbital photo pictures shown in the left of diagram correspond to the each of the orbital energy levels, in which the Ψ_1 indicate the electron comes from O atom mainly. Therefore, the σ_s correspond to the lone pair of O atom in Lewis structure. The energy level Ψ_2 looks like the sp orbital, which is a covalent bond between C and O in Lewis structure. The energy level Ψ_3, Ψ_4 correspond to the π orbital, which are covalent bond between C and O in Lewis structure. The energy level Ψ_5 looks like the sp orbital, but the contribution comes from the C atom mainly, which indicate the lone pair of C atom in Lewis structure. The energy level Ψ_6, Ψ_7 correspond to the π^* orbital, and Ψ_8 correspond to the σ_p^* [13].

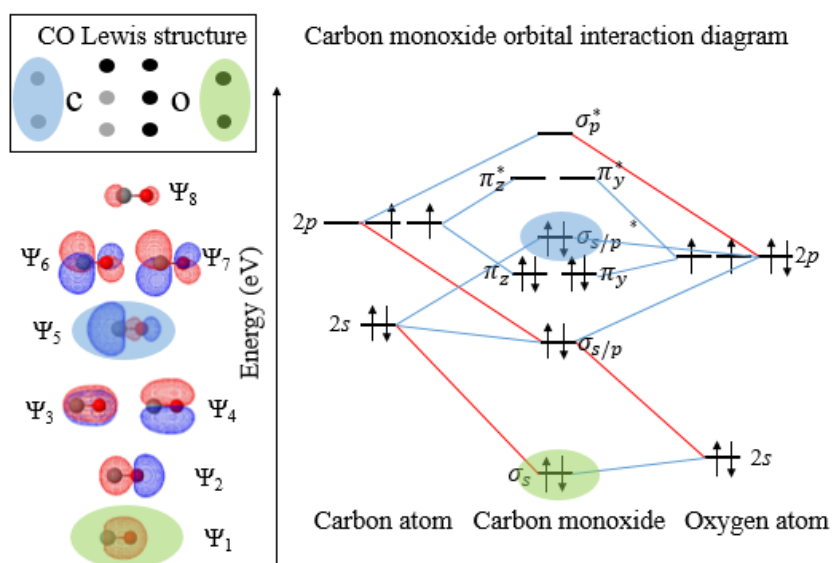


Figure 4.6 CO Lewis structure and carbon monoxide orbital interaction diagram.

4.4.2 CO bonding with transition metals

- Mechanism

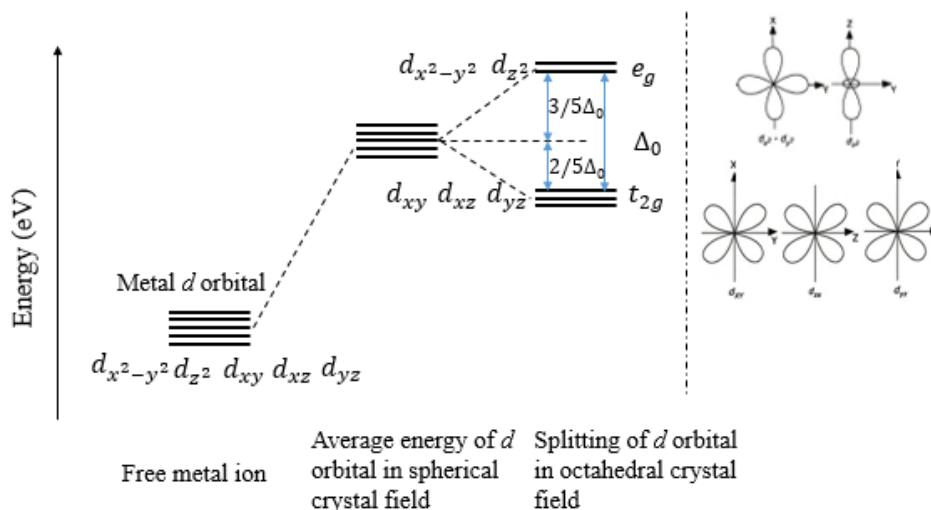


Figure 4.7 Energy splitting of d orbitals in an octahedral ligand field.

We will discuss complexes, which are formed by the bonding of a transition metal with a ligand. The crystal field theory has been introduced to explain the bonding states of complexes. The crystal field theory is based on the idea of an electrostatic field and takes into account the interaction between the point charge or point dipole of the ligand and the d electrons of the transition metal. If a negative charge surrounds this metal ion in a spherically symmetrical manner, the interaction with the positive charge of the metal ion greatly stabilizes the whole system. However, as a result of the repulsion between the electrons in the orbitals of the metal ion and this non-electric field, the energy of all the orbitals slightly increases. In metal complexes, the ligands are attached to the metal ion and the resulting field deviates significantly from spherical symmetry. If the ligands are bound in the $\pm x$, $\pm y$, $\pm z$ directions so as to form an octahedron, then the ligands interact strongly with the $d_{x^2-y^2}, d_{z^2}$ orbitals (e_g orbitals) overhanging the x , y , z directions, and the energy of these orbitals is raised due to repulsion. On the contrary, the d_{xy}, d_{yz}, d_{zx} (t_{2g} orbitals) are located in the middle region of the bonded ligands, so the repulsion between electrons is small and their energies are stabilized. As a result, the e_g and t_{2g} orbitals split, as shown in Figure 4.7. This split results in the existence of d orbitals with different energies, which also leads to the donation and back donation of electrons [13].

The two split d orbitals, the e_g orbital forms a σ bond with the HOMO of carbon monoxide to form a donation bond. On the other hand, the t_{2g} orbital forms a π bond with the LUMO of carbon monoxide, forming a back donation bond. The energy diagrams of the metal complexes formed by the bonding of the d orbitals of the transition metals with the HOMO and LUMO of carbon monoxide are shown in

Figure 4.8 below [13].

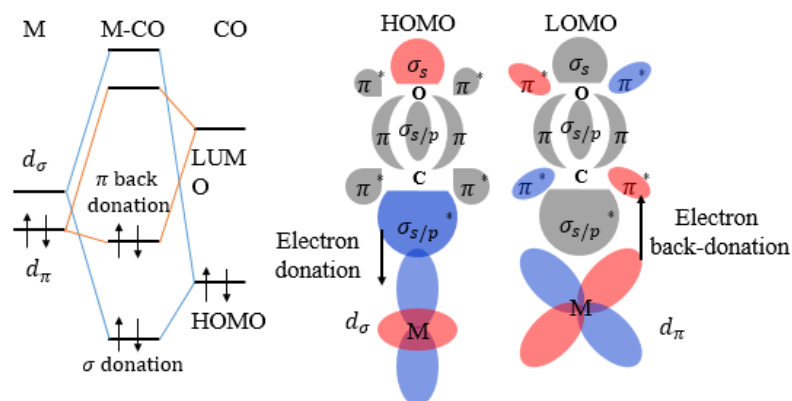


Figure 4.8 Diagram of the coupling between the d orbitals of transition metals and the HOMO and LUMO of CO molecules, and photo picture in the right correspond to diagram.

▪ Experiments

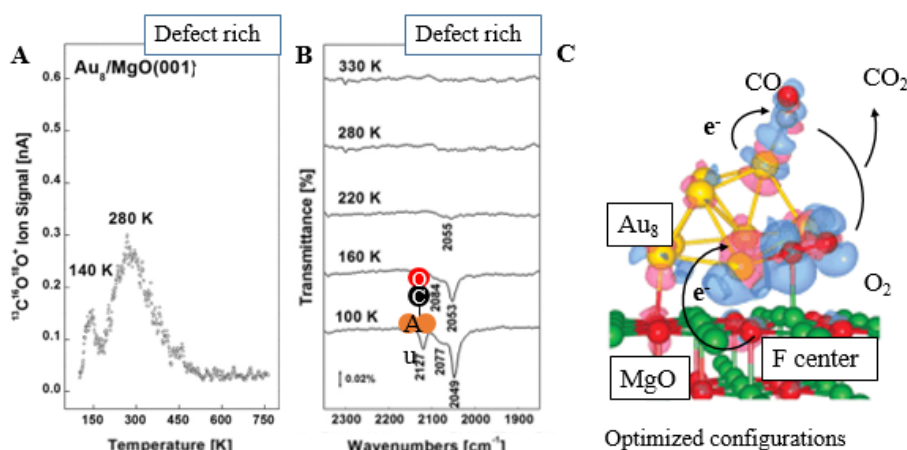


Figure 4.9 Mass spectrometric signals pertaining to the formation of CO_2 on Au_8 deposited on (A) F-center-rich. (B) Fourier-transform IR spectra measured for the same surfaces (defect-rich) and with the same CO and O_2 exposures as in (A) at various annealing temperatures. (c) Optimized configurations of Au_8 cluster anchored to a surface F center of MgO with O_2 and CO molecules adsorption [14].

Gold octamers (Au_8) bound to oxygen-vacancy F-center defects on Mg(001) catalyze the low-temperature oxidation of CO to CO_2 , which was investigated by the Infrared measurements and ab initio calculations. In the Figure 4.9(a), CO does react with O_2 on the Au cluster on the F center of MgO(001) surface. The stretch vibration of CO adsorbed Au cluster on the F center show a shift compared with perfect surface, indicating that the partial charged Au cluster affect the oxidation reaction, as shown in

the Figure 4.9(b). The configuration model was present in the Figure 4.9(c), in which the CO and O orbitals are involved in the bond with cluster. This experiment agrees with quantum ab initio calculations that CO bond with the Au though electron back-donation from Au to the CO antibonding orbital [14].

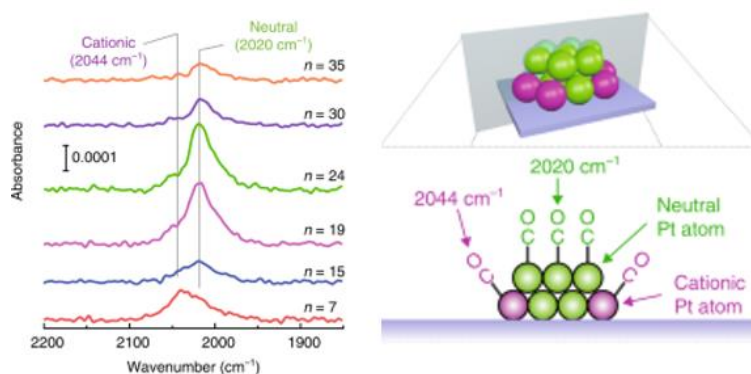


Figure 4.10 (a) Infrared reflection absorption spectroscopy (IRAS) spectra of ^{13}CO adsorbed on Pt $_n$ /Al $_2$ O $_3$. (b) Schematic diagram illustrating the adsorption of CO on a Pt cluster [10].

The CO oxidation activities of Pt nanocluster catalysts on alumina supports were investigated by Infrared reflection absorption spectroscopy (IRAS) and DFT. It is clarified the CO adsorbed on both neutral and cationic Pt atoms with the cationic Pt atoms contact with the support surface, as shown in Figure 4.10 (a, b). It demonstrated that the ratio of neutral to cationic Pt atoms in the Pt nanocluster was strongly correlated with the CO oxidation activity [10].

This research provides Infrared spectra for the CO adsorbed on the Pt clusters and reaction activity relation with the ratio of neutral and cationic, however, they didn't give the CO bonding mechanism and a lack of experimental atomic resolution of CO adsorption mechanisms upon changing the adsorption sites, which is enhance progress toward the design specific nanocatalytic systems.

4.5 Investigations of oxygen reactivity on Pd NPs

In this section, we describe the reactivity of O $_2$ on the Pd nanocluster at room temperature.

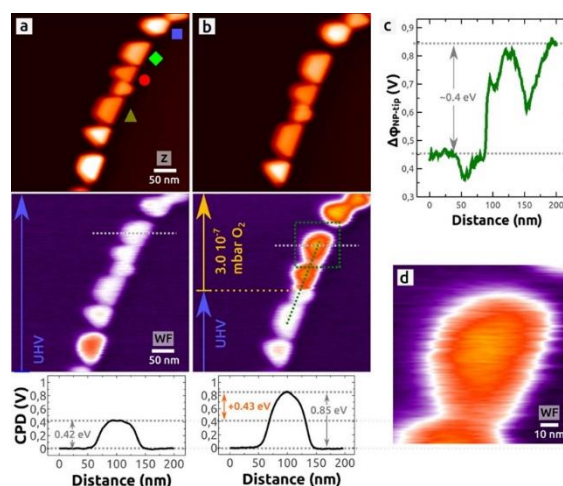


Figure 4.11 (a) As-prepared Pd NPs imaged by KPFM during an exposure of O₂ at room temperature (771 L). One KPFM experiment is represented by a vertically arranged topography (top) and WF image (bottom), with a representative WF profile underneath taken from the gray dotted line in each WF image. (c) Region of the dotted green square in the WF image in (b). (d) Atomic O with a coverage of 3/12 ML (0.25 ML) on O adsorbed on Pd(111) [15].

Oxygen adsorption and desorption on Pd NPs on highly oriented pyrolytic graphite experiments are studied by Kelvin probe force microscopy under ultrahigh vacuum (UHV) conditions. In the Figure 4.11 (a, b), the topographic and KPFM images of Pd NPs before and after exposure of oxygen molecule. It demonstrated that CPD increases 0.43 eV of Pd NPs because of work function increased. In addition, the O adsorbed on Pd(111). The atomic O with a coverage of 3/12 ML (0.25 ML) on O adsorbed on Pd(111) are calculated as shown in Figure 4.11 (c) [15].

So far, partial of the Pd clusters are exposed to O₂ molecules and become able to activate O₂ and catalyze the CO+O₂ reaction at 300K [16]. However, the experimental challenge of imaging 3D nanocluster with atomic resolution makes the interpretation the oxygen reactivity on the metal cluster difficult.

4.6 Conclusion

In summary, we generally clarified physical properties of the alumina thin films, charge state of metal atom and NPs on Al₂O₃/NiAl(110) surface, CO reactivity on the metal NPs oxygen and reactivity on Pd NPs for this study. Specifically, the unsolved physical knowledge in this catalytic system was pointed out in details in each chapter.

Chapter 5 Investigation of charge state of Pd nanoparticles on Al₂O₃/NiAl(110) surface by NC-AFM/KPFM

5.1 Introduction

Novel metal NPs are of great importance as catalysts in heterogeneous reactions such as CO oxidation which is employed to reduce toxic emissions [1-3]. The specific size of metal NPs show quantum effects and therefore can increase catalytic efficiency [4]. However, the support of the catalyst has a significant effect on the physics and chemical properties of metal NPs. Two types of support material have become of great interest: reducible oxides (e.g. TiO₂ and CeO₂) and non-reducible oxides (e.g. Al₂O₃, CaO₂ and SiO₂) [5-8]. In particular, Al₂O₃ has received attention because of its large band gap, enabling the effects of the underlying metal to be isolated, and its various surface structures [9-11]. To clarify the interaction between metal catalyst and non-reducible oxide surface quantitatively, a simple model catalysis system which palladium nanoclusters adsorbed on an alumina insulating film on NiAl(110), and micro-analytic method are required [3, 12].

The charge state of metal adsorbates has an important effect on their catalytic properties [13]. Measuring and manipulating the charge state of novel metal adsorbates supported on an insulating film substrate are of considerable fundamental interest and importance for redox reactions [14]. For instance, the charge state of metal adatoms and quantum dots has been investigated by atomic force microscopy (AFM), Kelvin probe force microscopy (KPFM) and Kelvin probe force spectroscopy (KPFS) [15,16]. In research on the CO oxidation activity, it was found that as the catalyst size decreases, the cationic Pt atoms at the edges of a cluster become strongly correlated with the CO oxidation activity [2]. Discussion about the mechanism of size dependent of charge state of Pd NPs and how line defects of alumina thin film affect the charge state are needed.

In addition to characterizing the electrostatic properties, KPFM is a powerful tool for measuring and manipulating charge state with atomic resolution [16-18]. As a complementary technique to noncontact

atomic force microscopy (NC-AFM), KPFM allows the simultaneous measurements of the topography and local contact potential difference (LCPD). KPFM has been used to measure the charge or dipole on an insulating ionic film and charged metal adsorbates, such as F^+ or F^{2+} color centers in a MgO film on a silver surface [19, 20]. However, in the previous results, no direct experimental evidence has been proposed for the size dependence of the charge state of the Pd NPs on $Al_2O_3/NiAl(110)$.

Ideally, the charge state of a single Pd/Pt atom or nanocluster on the alumina films on NiAl(110) is dependent on its size and adsorption sites. However, the interaction of the insulating ultra-thin film with a substrate electrode due to the Schottky barrier makes the study of the electronic properties of adsorbates on insulating thin film systems challenging. At present, physical fingerprint of the KPFM DC bias voltage variation effect on the thin film depletion region as the tip polarity change remains unknown. In addition, this depletion region could affect the KPFM image contrast of the adsorbates with the surface, which is not desirable for correct interpretation.

Here, we use NC-AFM and KPFM to investigate the size dependence of the LCPD of Pd NPs on an $Al_2O_3/NiAl(110)$ surface. The work function change of Pd NPs, due to electron transport, is discussed by classical electrostatic model. Specifically, different electrostatic property of different line defects is demonstrated through the performance of LCPD distance-dependent intuitively. Finally, we demonstrate the underlying mechanism of influence of line defects on the charge state variation of Pd NPs.

In contrast with previous results, we found a reversed KPFM contrast of the Pd NPs and we employed a KPFM model that includes the analysis of the blocking contact between the alumina film and the NiAl(110) substrate. This model could be used to explain how the KPFM DC bias voltage variation affects the KPFM contrast of the Pd NPs on and insulating thin film. Even when the charge state of Pd NPs was unchanged, the KPFM contrast reverse appeared as the tip polarity change.

5.2 Methods

5.2.1 AFM/KPFM method

The experiments were performed by ultrahigh vacuum NC-AFM at room temperature. The NC-AFM system was operated in the frequency modulation detection method with the cantilever oscillation amplitude kept constant [21]. All images were obtained in the constant-frequency mode. As our KPFM setup applies an AC voltage (V_{AC}) at frequency ω plus a DC voltage (V_{DC}) to the sample, the CPD is

consistent with the work function change. Electrostatic force (F_ω) between the AFM tip and sample is given by $F_\omega = -\frac{\partial C(z)}{\partial z} (V_{DC} - V_{CPD}) V_{AC} \sin(\omega t)$, where z is the direction normal to the sample surface, V_{CPD} is the potential difference and C is the capacitance between tip and sample surface separately. V_{DC} nullifies the oscillating electrical forces that originated from CPD between tip and sample surface. Detail information was described in our previous work [22].

The NiAl(110) surface was prepared by cycles of Ar ion sputtering (2.5 keV) for 20 min and annealing for 30 mins at 1000 °C. The alumina thin film was obtained by exposing NiAl(110) to 1000 L O₂ followed by annealing at 380 °C [23, 24]. Palladium was evaporated onto the alumina thin film surfaces of interest using an electron beam evaporator (Omicron) at room temperature. The Pd flux was calibrated and verified by AFM measurements on the Pd exposed NiAl(110) crystal. The evaporator deposition rate was 6.4×10^{17} atoms/(cm²·s) (about 0.13 ML/min) [25]. An Ir-coated Si cantilever (resonant frequency of 1.12 MHz) was used.

5.2.2 Charge state by classical electrostatic model

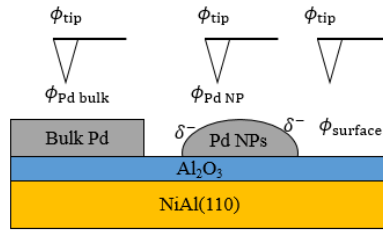


Figure 5.1 KPFM measurement model of Pd NPs on the Al₂O₃/NiAl(110) surface.

We deduce the charge state of NP by a classical electrostatic model, which is shown in the Figure 5.1. The work function ϕ difference (ΔW) between a metal NP and the corresponding bulk metal arises from a difference in image force fields (ΔW_{im}) and from the Coulomb field near the surface of the NP due to the stored charges inside (ΔW_C) [26]. The WF difference between a metal NP and the corresponding bulk metal (ΔW) is shown as follows:

$$\begin{aligned}
 \Delta W &= \phi_{Pd NP} - \phi_{Pd bulk} \\
 &= (\phi_{surface} + e\delta V_{LCPD}) - \phi_{Pd bulk} \\
 &= (4.28\text{eV} - 0.6\text{eV} + e\delta V_{LCPD}) - 5.22\text{eV} \quad (5.1) \\
 \Delta W &= \Delta W_{im} + \Delta W_C = \left(2N - \frac{1}{4}\right) \frac{1}{4\pi\epsilon_0} \frac{e^2}{2R}
 \end{aligned}$$

The first term is the difference between the image potential energy at the surface of a sphere and that of a flat metal plane. $\Delta W_{\text{im}} = -\frac{1}{8} \frac{1}{4\pi\epsilon_0} \frac{e^2}{R}$, where ϵ_0 is the vacuum permittivity, and R is the radius of the NP. The charges inside the metal NP, considered to reside at its center, induce a Coulomb potential energy at the surface, $\Delta W_{\text{C}} = N \frac{1}{4\pi\epsilon_0} \frac{e^2}{R}$, where N is the charge state of the NP, which can be either positive or negative. Combining ΔW_{im} and ΔW_{C} we get the relation as follows:

$$N = \frac{2\pi\epsilon_0}{e^2} 2H\Delta W + \frac{1}{8}$$

$$= \frac{H}{1.44\text{nm}\cdot\text{eV}} (e\delta V_{\text{LCPD}} - 1.54\text{eV}) + \frac{1}{8} \quad (5.2)$$

N is the charge state of Pd NP, and H is the height of the NP, the height of the NP is used because of the vertical convolution is smaller than the lateral for AFM tip apex.

5.2.3 Strategies to control the size and adsorption site of Pd NPs

The first strategy is to change the Pd evaporator deposition rate by setting different flux.

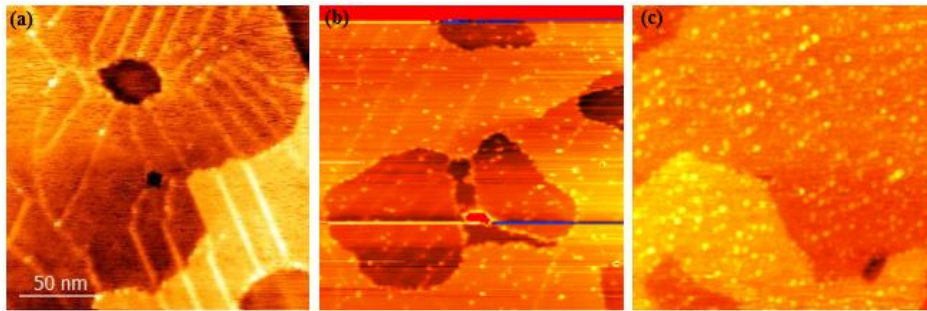


Figure 5.2 The evaporator deposition rate about (a) 0.002 ML/min, (b) 0.043 ML/min, (c) 0.125 ML/min

The second strategy is to do sub-annealing after Pd deposition on the surface.

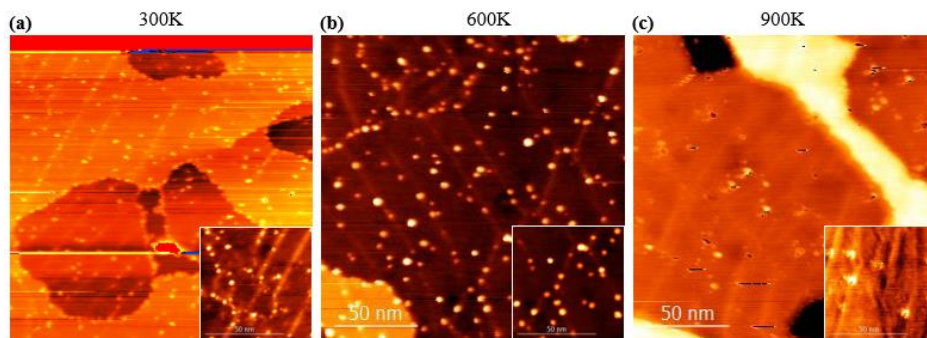


Figure 5.3 Sub-annealing after Pd deposition on the surface (a) 300 K, (b) 600 K, (c) 900 K.

The third strategy is to change the support temperature when deposition.

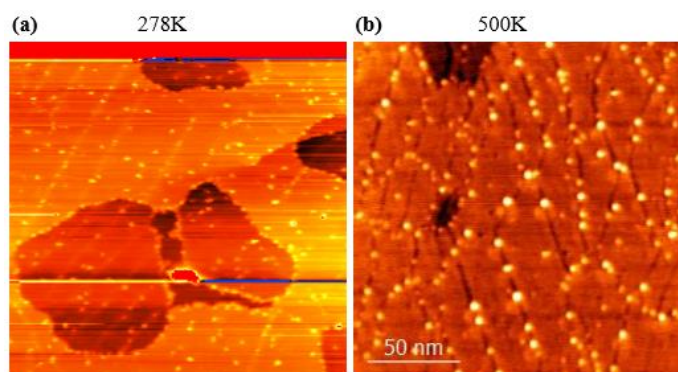


Figure 5.4 Pd NPs deposition at support temperature (a) 278 K, (b) 500 K.

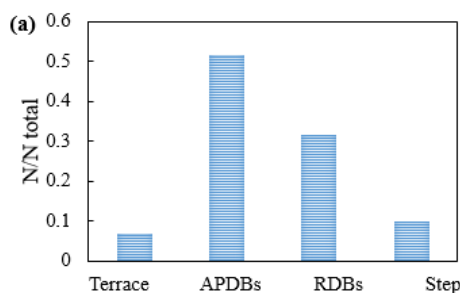
5.3 Experimental results and discussion

5.3.1 Clarification of size and adsorption sites of Pd NPs

At room temperature, we could increase the density and size of Pd by increasing evaporator deposition rate, instead of adsorption sites, as shown in Figure 5.2. In addition, we could increase the size by sub-annealing the catalytic surface, suggesting Pd NPs on the surface have the mobility due to the weak binding with the domain surface. In the Figure 5.3, the size of Pd NPs increase after sub-annealing, but decrease and desorb over 900 K. Furthermore, we could control the Pd NPs adsorption on line defects by increasing the support temperature while Pd deposition, as shown in Figure 5.4, which is further support the Pd NPs binding weakly with the alumina film. The higher temperature enables the Pd NPs diffusion on the surface and are more likely trapped on the line defects.

We select the sizes of the Pd NPs in 1-10 nm in diameter and mainly adsorbed on the line defect sites by the method above.

The correlation between the adsorption sites and their size on the alumina film is further discussed by analysis of hundred Pd NPs.



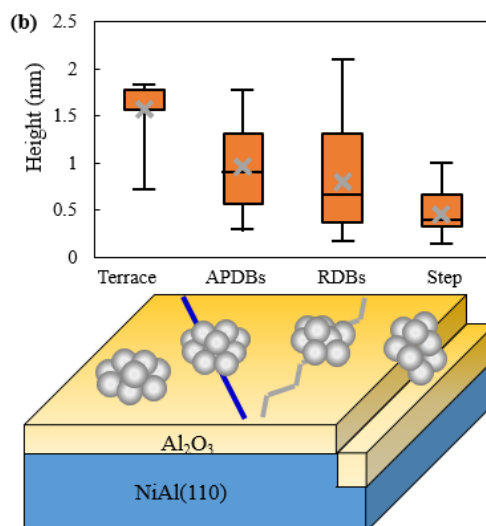


Figure 5.5 (a) Histogram of adsorption sites for 101 Pd NPs. (b) The statistics of Pd NPs heights on different adsorption sites, including terrace, APDBs, RDBs and step edge.

From the histogram in Figure 5.5 (a), it reveals the APDBs and RDBs are the preferable adsorption site for Pd NPs than step edge and surface. It was demonstrated that line defect sites provide higher binding energies, which modifies the Pd-alumina film interaction and may therefore affect the electronic of Pd NPs.

The Pd NPs height were determined by the AFM at different adsorption sites, including APDBs, RDBs, step edges and surface. The recorded height of Pd NPs at surface is largest, at step edges is smallest. We also found that the average size of Pd NPs on the APDBs is larger than on the RDBs. The variations of the heights exist because the measured signal is the real height convoluted with the tip geometry. Rarely adsorption Pd NPs on surface has the larger size, which may therefore indicate Pd NPs binding on the point defects of the surface and longer distance to migrate to the line defects.

5.3.2 Characterization of charge state Pd NPs by AFM/KPFM

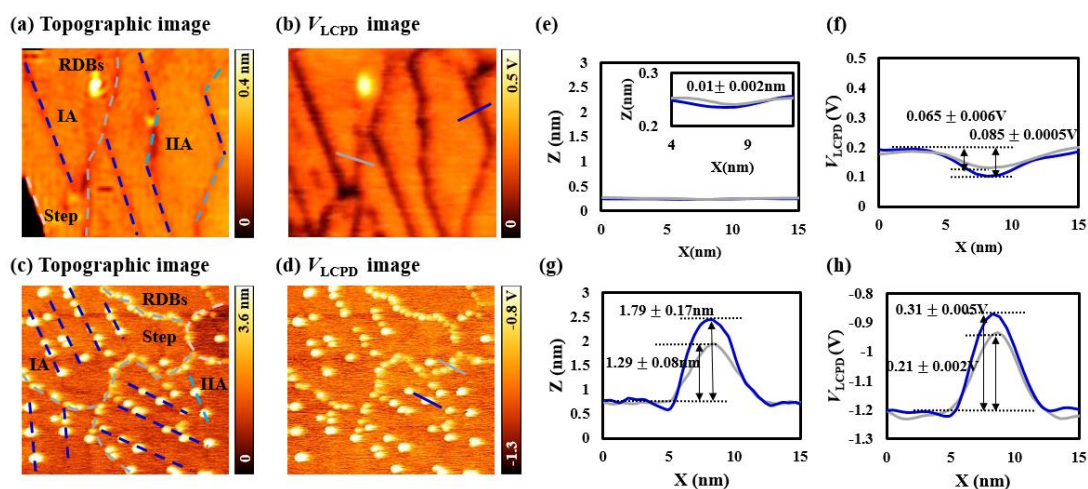


Figure 5.6 (a, b) Topographic and V_{LCPD} images of $Al_2O_3/NiAl(110)$ surface. (c, d) Topographic image and V_{LCPD} images of Pd NPs on $Al_2O_3/NiAl(110)$ surface (step edges: pink dashed line; RDBs: gray dashed line; IA: blue dashed line; IIA: light blue dashed line). (e, f) Line profiles of height and V_{LCPD} on RDBs (gray) and IA (blue) in (a) and (b), respectively. (g, h) Line profiles of height and V_{LCPD} of the Pd NPs on RDBs and IA in (c) and (d), respectively. Imaging parameters: $A_{mp} = 0.8$ nm, size = 90×70 nm², (a, b) $\Delta f = -69$ Hz, and (c, d) $\Delta f = -40$ Hz.

The correlation of the Pd NPs size and adsorption sites is further supported from analysis of electronic properties. Figure 5.6 shows a set of NC-AFM and LCPD images and corresponding line profiles of parts of an $Al_2O_3/NiAl(110)$ surface without and with Pd NPs. In Figure 5.6 (a), the line defects consist of antiphase domain boundaries (IA, IIA with different orientation), reflection domain boundaries (RDBs) and step edges, which appear as dark or bright lines depending on the exact tip apex. Similar dark-contrast line defects have been observed in atomic-resolution AFM images by the group of Simon and Freund [27,28]. However, bright-contrast line defects have been imaged by our group as reported in a previous paper [23]. We attribute the contrast reverse of the line defects to the tip apex picking up a specific atom when the tip scans the surface. In Figure 5.6 (c), the bright spots are Pd NPs that adsorbed on the line defects of the alumina surface after Pd atoms were evaporated in vacuum at room temperature. Beniya's group found that Pt_7 clusters with a planar structure are thermally immobile, and adsorbed on line defects, which is consistent with our experimental results [29].

KPFM measurements were performed during AFM imaging in the constant frequency shift mode.

The dark or bright contrast in the KPFM images was used to detect the local charge state of the surface or adsorbed metal clusters. The two KPFM images in Figure 5.6 (b) and (d) were recorded simultaneously with the images in Figure 5.6 (a) and (c). Line defects appear as dark lines in Figure 5.6 (b), indicating work function decrease. As theoretically discussed in a previous study, the absence of oxygen in the unit of alumina results in the different properties of the line defects, which contributes to a positive work function [11]. In Figure 5.6 (d), the Pd NPs appear as bright spots, indicating that they are negatively charged on the surface. The electrons in the Pd NPs can be explained by the charge transfer between the substrate and the Pd NPs as a result of the mismatch between their work functions. The distance-dependence of the LCPD was also performed to verify the charge state of the line defects and Pd NPs in case of the cross-talk and tip-apex-induced dipole moments as shown in Figure 5.7. Actually, Pd atoms on an $\text{Al}_2\text{O}_3/\text{NiAl}(110)$ surface were observed by scanning tunneling microscope (STM) by Ho's group, who suggested that the adsorption of Pd atoms on hollow sites of the surface was accompanied by electron transfer from atoms to the metal oxide.[30] Beniya's group identified neutral Pd clusters on average less than 0.1 electron was transferred in each cluster. Furthermore, the neutral or cationic Pd atoms at a cluster edge on a $\text{Al}_2\text{O}_3/\text{NiAl}(110)$ surface have been deduced [29]. In the study, we obtained the different result that Pd NPs presented as a negative charge state on a $\text{Al}_2\text{O}_3/\text{NiAl}(110)$ surface.

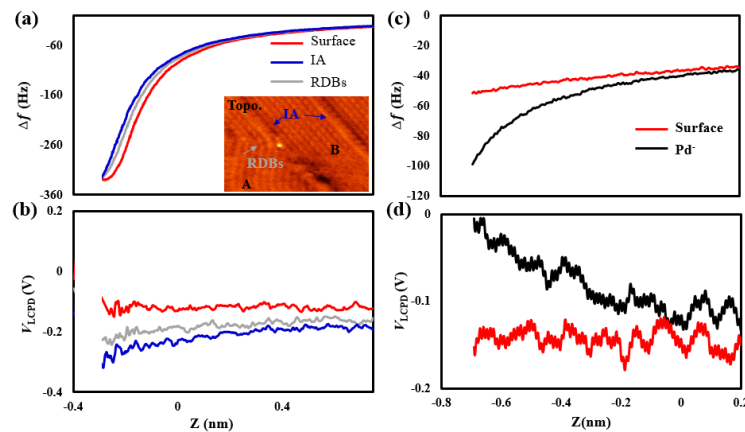


Figure 5.7 (a, b) Distance-dependent variation of the frequency shift and V_{LCPD} on top of the IA and RDBs and bare alumina surface (as shown in the inset in panel a). (c, d) Distance-dependent variation of the frequency shift and V_{LCPD} for Pd NPs and bare alumina surface.

The line profiles in Figure 5.6 (e), (f), (g) and (h) were taken through Pd NPs in Figure 5.6 (a), (b),

(c) and (d), respectively. The heights of the different line defects are almost equal, the heights of the Pd NPs vary from 1.29 to 1.79 nm and the Pd NPs on IA are larger than those on the RDBs. The V_{LCPD} of IA is always smaller than that of the RDBs. The V_{LCPD} of IA is always smaller than that of the RDBs and the change in the LCPD of the Pd NPs is related to the work function via the following equation:

$$\begin{aligned}\delta V_{\text{LCPD}} &= V_{\text{Pd NP}} - V_{\text{surface}} \\ &= \frac{\phi_{\text{Pd NP}} - \phi_{\text{surface}}}{e},\end{aligned}$$

where $\phi_{\text{Pd NP}}$ and ϕ_{surface} are the work functions of the Pd NPs and alumina/NiAl(110), respectively, and that e is the absolute value of the elementary charge. Details of the KPFM measurement model of Pd NPs on the $\text{Al}_2\text{O}_3/\text{NiAl}(110)$ is shown in the Figure 5.1. It was observed that the work function NiAl(110) decreased by 0.6 eV after well-ordered Al_2O_3 formation on it [31]. The larger the Pd NP is, the larger its V_{LCPD} has.

5.3.3 Size dependence of charge state of Pd NPs

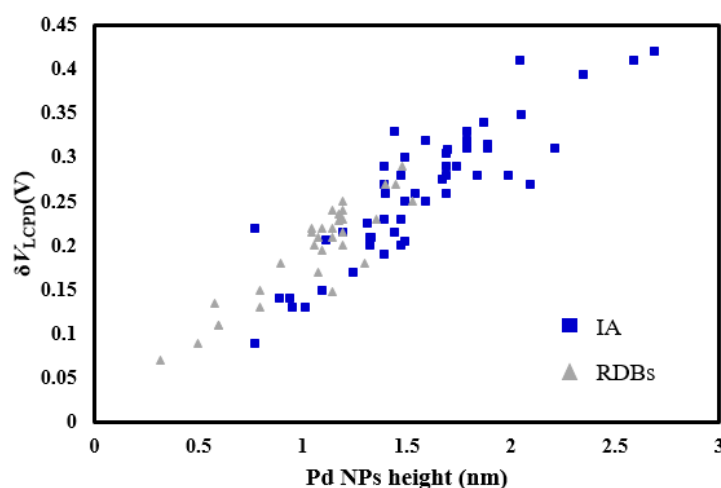


Figure 5.8 δV_{LCPD} of the Pd NPs on different line defects vs the Pd NPs height, where gray and blue symbols represent Pd NPs on the RDBs and IA, respectively.

A plot of δV_{LCPD} as a function of the Pd NPs height was carried out in Figure 5.8, which shows the δV_{LCPD} increases with the Pd NPs height. For the reason that size selected clusters containing a handful of atoms may possess noble catalytic properties different from single layer or bulk catalysts, Pd NPs heights smaller than 0.3 nm and larger than 3 nm are not included [32]. In addition, we clarify the δV_{LCPD} of all the Pd NPs on IA and RDBs because IA and IIA has similar adsorption behavior. The δV_{LCPD} fluctuation of NPs of the same size may be due to the variation in particle geometry and the

orientation of the exposed facets.

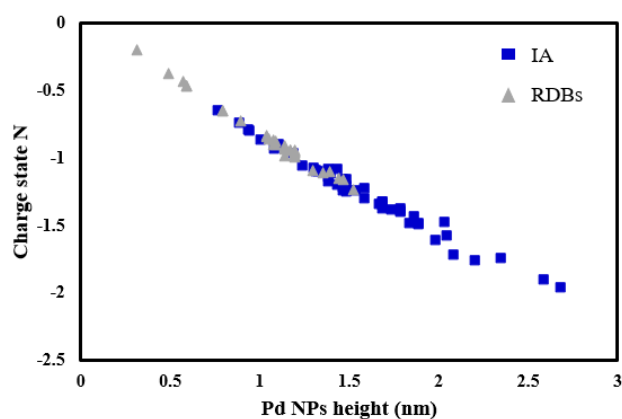


Figure 5.9 Charge state of the Pd NPs on different line defects extracted from the measured V_{LCPD} , where gray and blue symbols represent Pd NPs on the RDBs and IA, respectively.

The charge state as a function of the Pd NPs height was plotted in Figure 5.9. The Pd NPs are like electron reservoir and the number of electrons increases with the Pd NPs size. In addition, the charge inside the Pd NPs is determined by the capacitance between the NPs and substrate. The calculated charge state of the NPs shows a linear relationship with the NPs size. In our experimental results, the charge of Pd NPs is proportion to its height linearly, which is consistent to the theory. Besides, the local charge storage also reflects the effect of the ionic alumina film, especially the positively charged line defects. We found that the size and charge state variation for Pd NPs on IA is much larger than that for Pd NPs on RDBs. Similar adsorption behaviors (different size of Pd NPs on different line defects) have been observed by Freund's group for the case of Pd was exposed to the alumina surface at room temperature [33].

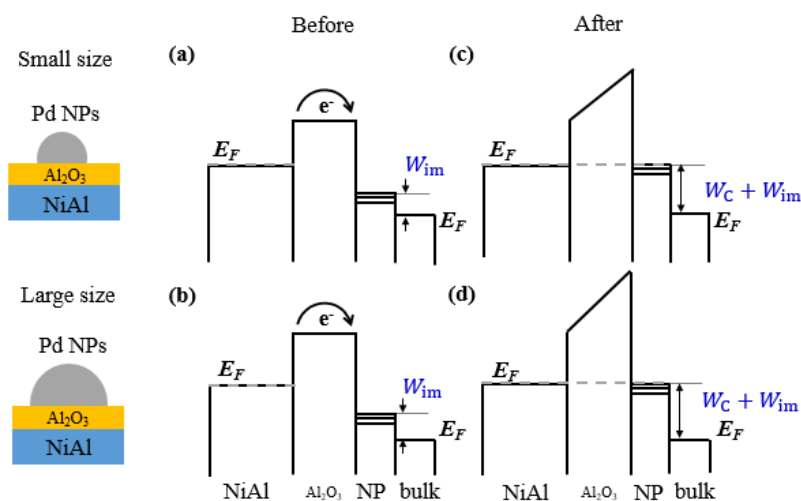


Figure 5.10 Band diagram of Pd NPs with different sizes on Al₂O₃/NiAl(110) before (a, b) and after (c, d) charge transfer.

To understand the mechanism of the size-dependent charge state and the effects of the different line defects, we consider the band diagram shown in Figure 5.10. The electron tunneling is caused by the different potentials of the substrate and Pd NPs. Note that initial image potential is different in different size of Pd NPs as shown in Figure 5.10 (a, b). After the establishment of equilibrium of the electrochemical potentials (Fermi levels) between substrate and adsorbed Pd NPs, the charge state change of Pd NPs caused by Coulomb potential and image potential is in the linear relationship with the height. Based on our experimental results, we found the work function of largest size Pd NPs is equal to the work function of substrate, which is consistent to the model analysis. Although there are lots of work focus on the quantum effects of the novel metal NPs on oxide surface, the electrostatic property of Pd NPs is similar to Pd bulk [34, 35]. In addition to the different charge state variation on the line defects, accordingly, we conclude that it caused by the size variation of the Pd NPs mainly. The size variation of Pd NPs is relatively large when it adsorbed on the IA line defects, it has the large charge state variation. Note that the different domain boundaries (IA and RDBs) show different oxygen-deficiency structure, which show the different work function as shown in the Figure 5.6 (f), hence contribute to the different size range on different line defects. As for the decreased work function of the line defects is considered to lower the effective tunneling barrier for the adsorption of Pd NPs, which maybe contribute to different charging behaviors, while the topic on the static charge state of the Pd NPs needs the further support in the future.

5.3.4 Effect of tip polarization on KPFM measurement

Kelvin probe force microscopy images contrast reverse occur on Pd NPs on ultra-thin insulating alumina on NiAl(110), as tip polarity change. This can be attribute to the work function of alumina increased in contrast to unchanged Pd NPs, because the depletion region created in alumina and substrate has a bias voltage dependence.

KPFM image contrast having tip polarity dependence are the obstacle of interpreting the charge landscape, however, this physical mechanism on the property of ultra-thin film has never been reported.

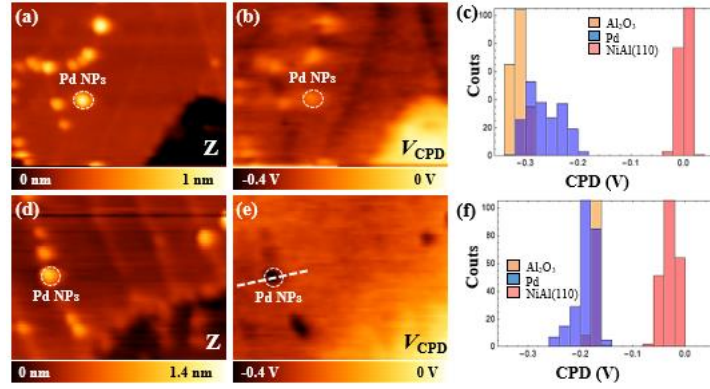


Figure 5.11 Topographic images and local surface potential images of Pd nanoclusters on Al₂O₃ thin film with NiAl(110) substrate. (a, b) Images acquired using negatively and (d, e) positively terminated tips. (c) (f) Corresponding normalized histogram of KPFM images in panel b and e. Imaging parameters: constant- Δf mode, $V_{AC} = 500$ mV, $f_{AC} = 190$ Hz, size of 66×50 nm².

Figure 5.11 (a, b) shows typical topographic and KPFM images of Al₂O₃/NiAl(110) thin films obtained simultaneously. Owing to the step edge of the alumina film in the V_{CPD} -compensated image appearing as a theoretical value, we attribute that these images obtained with a neutrally terminated tip. The observed LCPD images clearly exhibit distinct surface potentials and the charge state of Pd NPs, which are reflected by the work function of the surfaces and local charge distributions over Pd NPs sites. The work function of well-ordered Al₂O₃ formation on NiAl(110) decreased by 0.32 eV, which can be distinguished from the normalized histogram shown in Figure 5.12 (c). The adsorbed Pd NPs show a bright contrast in the KPFM images, which is caused by the metallic electronic properties as illustrated in our previous results.

After typical tip apex terminated with unknown atoms, the change-tip was moved to approach and locate at different area of the sample. Figure 5.11(d, e) show a topographic and KPFM images of the surface obtained simultaneously with this unknown terminated tip. Notably, this is an irreversible change of the tip. The step edge of the alumina film imaged by the changed tip is relatively smaller than the theoretical value. In contrast with the LCPD contrast of Pd NPs on alumina surface in Figure 5.11 (b), it is revealed that the LCPD contrast was reversed. Additionally, the CPD of the alumina thin film increased as shown in Figure 5.11 (f), which paves the way to the investigation of the effect of the tip polarity, indicating that the tip became positively charged. Note that the alumina thin film is a two-

dimensional structure, and the thickness variability of the film inducing the LCPD contrast reversal of the Pd NPs is not the case discussed here. Therefore, we focus on illustrating the dependence of the CPD variability of alumina and LCPD contrast of Pd NPs on the film on the tip polarity.

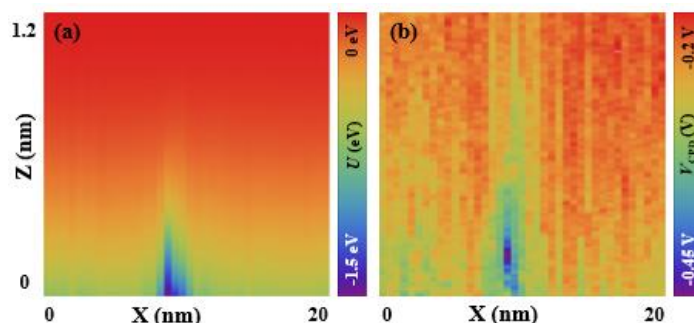


Figure 5.12 (a) $U(x, z)$ map and (b) $V_{CPD}(x, z)$ map of Ir-coated tip on top near one Pd NP adsorbed on the line defects of the alumina thin film.

We performed systematic measurements of potential U and the KPFM signal V_{CPD} with respect to the lateral X and vertical Z coordinates with a changed tip (positively charged), yielding two-dimensional Z - X slices of U and V_{CPD} data. U is the potential calculated from the frequency shift and V_{CPD} is the raw data of the compensating bias voltage. These data were recorded along a predefined line (see Figure 5.11 e) by an effective constant-height mode. Note that charge analysis is more complicated in the near tip-sample distance owing to the chemical interaction or induced dipole moment. Here, we discussed the electrostatic interaction in the larger tip sample distance (around 0.3 nm away from the surface). In this long-range force range, no distance dependence of the KPFM signal is observed on the alumina thin film, which means that the KPFM signal is determined solely by the CPD of the homogeneous tip and surface. In this hypothetical case, the observed distance dependence on the top of the Pd NPs points to the presence of additional charges in the tip sample system. To explain the additional charges, we can attribute the positive charge to the Pd NPs commonly. Alternatively, we can attribute that electron density of alumina film is increased because of the formation of a changeable interfacial dipole layer in alumina film.

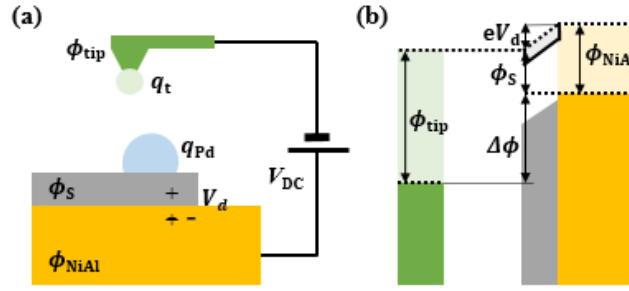


Figure 5.13 (a) Set up of the tip-sample considered in the KPFM model, consisting of the tip, thin film Al_2O_3 , and substrate $\text{NiAl}(110)$. Charge can be present both in tip apex and adsorbed Pd nanoparticles. V_d is depletion voltage induced by the interfacial dipole layer. (b) Energy diagram of the tip-sample, illustrating the contact potential difference $\Delta\phi$ between the sample and the tip.

In the follow text, a KPFM model and corresponding energy diagram shown in Figure 5.13 are employed to explain the above experimental results. In this model, it illustrates how does the depletion voltage induced by the interfacial dipole layer of alumina film attributes to the KPFM contrast reverse of the Pd NPs on alumina, as the tip apex polarity change. As shown in Figure 5.13 (a), the metal tip and sample have different work functions ϕ_{tip} and ϕ_{NiAl} leading to the contact potential difference $V_{\text{CPD}} = V_{\text{DC}}$ typically measured with KPFM on conducting samples. While blocking contact, known as Schottky barriers, formed depends on the relative work functions of the insulator ϕ_S and that of the metal contact ϕ_{NiAl} . In the case of $\phi_{\text{NiAl}} > \phi_S$, electrons flow from the insulator into the metal to establish thermal equilibrium conditions. The work function of alumina film is derived as $\phi_S = \phi_{\text{NiAl}} - eV_d$. V_d is the field induced by depletion region in the insulating film. In the condition that depletion length larger than the film thickness, once the higher negative voltage applied to the substrate, the work function of alumina film increased as ϕ_S' . In addition, assuming the work function of Pd NPs is located at a certain value between the ϕ_S and ϕ_S' , the KPFM contrast inverse of the Pd NPs could be presented.

It is proposed by this model that work function of the ultra-thin film increased by the bias dependence of the depletion area created by blocking contact between film and substrate, thereby causing the KPFM image contrast of Pd NPs on alumina film to be reversed. This work is important to elucidate the oxygen molecule and carbon monoxide chemical and physical adsorption in the catalytic process, which reflects the sequence and energy conversion of the reaction. Moreover, the change-tip apex may also be accompanied by a change in the shape, which requires further clarification.

5.5 Conclusion

In conclusion, we have clarified the size dependence of charge state of Pd NPs deposited on an $\text{Al}_2\text{O}_3/\text{NiAl}(110)$ surface by NC-AFM and KPFM at room temperature. Negatively charged Pd NPs on alumina thin film were clearly imaged by the KPFM, and the charge state extracted from the LCPD increases with increasing Pd NPs size linearly. Charge state change of Pd NPs consist of the work function difference between substrate and Pd NPs, Coulomb filed increased by the electron tunneling and size-dependent image potential. The line defects are considered to affect the size of adsorbed Pd NPs and induce increase the charge state variation of Pd NPs and enhancing the catalytic activity. Additionally, KPFM images contrast reverse occur on Pd NPs on ultra-thin insulating alumina on NiAl(110), as tip polarity change. This can be attribute to the work function of alumina increased in contrast to unchanged Pd NPs, because the depletion region created in alumina and substrate has a bias voltage dependence. Thus, this result implied that it is essential to determine the tip apex polarity to correctly interpret LCPD signals on ultra-thin film acquired by KPFM.

Chapter 6 Charge state of CO molecule on Pd NPs/Al₂O₃/ NiAl(110) by NC-AFM /KPFM

6.1 Introduction

Heterogeneous catalysts are solids that are added into gas or liquid reaction mixtures, enabling faster, large-scale production as well as effectively recovered, which is an essential consideration for industrial manufacturing processes [1,2]. In heterogeneous catalysis, the reactants adsorb onto the surface of the catalyst, and the availability of reaction active sites can limit the rate of heterogeneous reaction [3,4]. Heterogeneous catalysts are difficult to characterize precisely, and many studies have been conducted to locate active sites on various catalytic materials. Observations of the adsorption sites of reactants have shown that metal oxide interfaces are catalytically the most active, such as planar Au clusters on MgO/Ag(001) thin films and Pt clusters on graphene/Rh(111)[5, 6]. Furthermore, catalytic activity is related to the local charge state, and the catalytic activity of Au clusters on a MgO substrate can be enhanced by locally charging the substrate [7]. The ratio of neutral to cationic Pt atoms in the Pt nanocluster (NC) was found to be strongly correlated with the CO oxidation activity [8].

The Pd catalyzes to convert polluting hydrocarbons, carbon monoxide, and nitrogen oxide in the exhaust to water, carbon dioxide, and nitrogen in automobile catalytic converters (often combined with rhodium) [9]. Furthermore, Pd NP catalysts have high-performance for sustainable liquid-phase reactions [10]. So far, part of the Pd clusters are exposed to O² molecules and can activate O² and catalyze the CO+O² reaction at 300 K [11]. In addition, theoretical calculations have shown that Pd nanoparticles of ~4 nm, the highest amount of edge and corner sites, results in a good activity [12]. However, the atomic resolution of three dimensional Pd cluster hasn't be resolved in the AFM experiment at room temperature, which is vital for understanding the CO adsorption sites in heterogeneous catalysis.

CO is usually used as a probe molecule to study the electronic and geometric properties of metal catalysts [13]. A variety of averaging techniques had been used to study the CO adsorption behaviors [14,15]. Scanning tunneling microscopy (STM) has been utilized to investigate adsorption sites and

manipulation processes, which enables to address of individual molecules [16, 17]. Non-contact atomic force microscopy (NC-AFM) has been applied to quantify the force performance required to move CO laterally, the interaction between CO molecule and adatom or another CO molecule, and manipulation of its tilting [18-21]. Furthermore, some new insights have been illustrated the CO adsorption on the metal surface from molecular orbital principles in the aspect of DFT or on a single Pd-Fe₃O₄ catalyst by STM in real-time. More recently, CO-terminated tips have been used to probe chemical binding forces on single Fe atoms to elucidate individual atom chemical reactivity within flat Fe clusters depends on the coordination number of the investigated atom [22]. However, CO adsorption properties on nano-catalyst haven't been investigated by atomic resolution. Additionally, the nano-catalyst of adsorption sites effects on the charging mechanism of CO molecule are still lacking, which calls for the high resolution of the KPFM method, even at cryogenic temperatures. Therefore, a complete atomic understanding of local charge transfer in the catalyzed CO oxidation reaction remains elusive.

6.2 Methods

The experiments were performed using a home-built combined NC-AFM and KPFM under ultrahigh vacuum at room temperature (RT). The NC-AFM system was operated in the frequency-modulation detection method with constant oscillation amplitude (800 pm). All images were obtained in the constant-frequency mode. As our KPFM setup applies an AC voltage (V_{AC}) at frequency ω as well as a DC voltage (V_{DC}) to the sample, V_{DC} nullifies the f_{AC} component of oscillating electrical forces, providing V_{CPD} between the tip and the sample surface. Detailed information was provided in our previous work [23-25]. In our case, the local contact potential difference (LCPD) voltage can be determined with a feedback loop using KPFM.

Sample preparation

The NiAl(110) surface was prepared with cycles of Ar ion sputtering and annealing at 1000 °C. The alumina thin film was obtained by exposing NiAl(110) to 1000 L of O₂ followed by annealing at 380 °C [26, 27]. Palladium was evaporated onto the alumina thin film surfaces using an electron beam evaporator (Omicron EFM 3) at room temperature. The Pd flux was calibrated and verified by AFM measurements on the Pd-exposed NiAl(110) crystal. The evaporator deposition rate was 6.4×10^{17} atoms/cm²·s (about 0.13 ML/min) [28]. CO molecules (purity 99.9%) was exposed to the scanning

chamber at different background pressure. An Ir-coated Si cantilever (NANOSENDORS) was excited to vibration at its resonance frequency of 1.12 MHz.

Calculation

Our calculations were performed in slab geometry under 3D periodic boundary conditions. The surface was modeled using a NiAl substrate with an Al₂O₃ monolayer. In the z direction, slabs were separated from their periodic images by a 15 Å vacuum gap. Wave functions were expanded in plane waves with a kinetic energy cutoff of 400 eV as implemented in the VASP code. Ionic forces were converged to an accuracy higher than 0.01 eV/Å.

6.3 Results and discussion

6.3.1 Identification of CO molecule by force spectroscopy

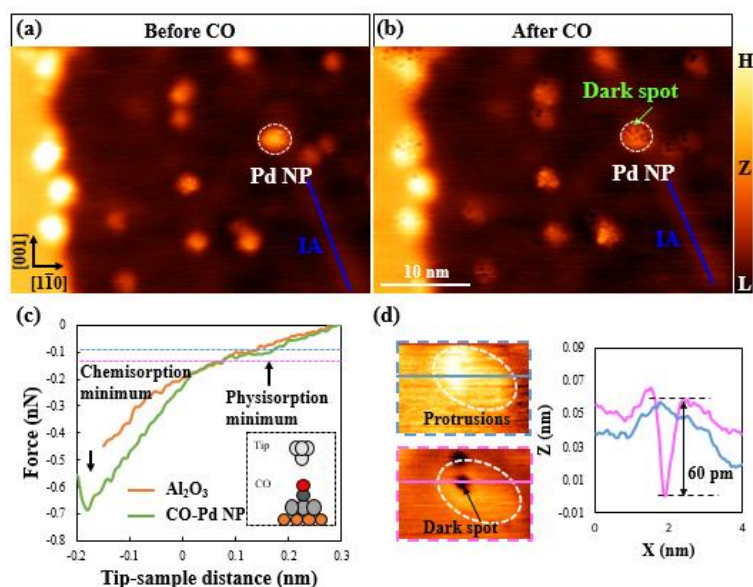


Figure 6.1 NC-AFM images of Pd NPs/Al₂O₃/NiAl(110) catalytic system following exposure to CO gas at room temperature. (a) Pd NPs with bright contrast under high vacuum condition. (b) CO molecule (blue arrow) adsorbed on one represent Pd NP (white dot circle) at CO pressure 3.8×10^{-8} Torr, and 1.6×10^{-6} Torr. (c) Model of Pd NPs/Al₂O₃/NiAl(110) catalytic system performing the Z spectroscopy, and experimental force versus tip-sample distance on top of Pd NP (orange) and CO molecule (green). (d) The AFM contrast of CO on Pd NP at different tip-sample distance in the (c) as blue and pink color. Imaging parameters: constant- Δf mode, $f_0 = 1.12$ MHz, $Q = 3304$, $V_{\text{bias}} = 0$ V, $A_{\text{mp}} = 800$ pm.

To investigate the CO molecule reactivity on the catalytic system, the real time imaging was

performed. In Figure 6.1(a) and (b) show the NC-AFM image of Pd NPs on the line defects and step of $\text{Al}_2\text{O}_3/\text{NiAl}(110)$ surface and after dosing 120 L CO molecule. The dark and bright spot could be distinguished clearly on the Pd NPs by the AFM images, which attribute to the CO molecule adsorption at RT. To support this assumption, the force curves versus tip-sample distance were obtained on top of the CO molecule and surface and provided the interaction between tip and local surface, as shown in Figure 6.1(c). The CO molecule force curve show two minimum at variation of tip-sample distance compared with surface, which can be assigned to the physisorption minimum and chemisorption minimum, characterized by previous results and theory. Thereby, this feature represents the interaction between O-terminated CO and metal atoms and can be used to distinguished the CO molecule. The force was derived by the method shown in chapter 2.3.3. The minimum force is 0.68 nN, which may be related to the coordination number of the investigated CO molecule. Additionally, the protrusion and dark contrast of CO on the Pd NP and surface can be imaged at different tip-sample distance as expected, which shown in the Figure 6.1(d). The bond length of the CO on the Pd NPs is around 60 pm, which is smaller than that 110 pm in gas phase [20]. This result may therefore indicate CO bond with Pd NPs on defect sites. According to the theory, the CO molecule bond with metal with the C atom side. Therefore, our results support the CO bond with Pd NPs at room temperature.

6.3.2 Investigations of charge transfer of CO molecule on Pd NPs by KPFM

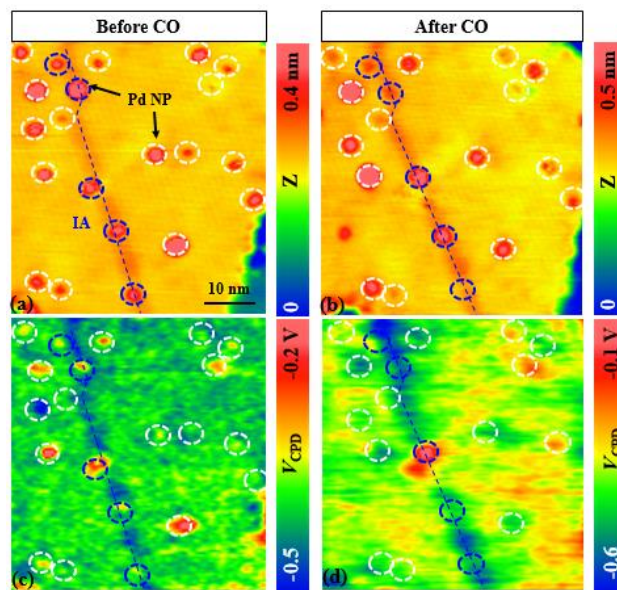


Figure 6.2 (a, b) Topographic and V_{CPD} images of Pd NPs/ $\text{Al}_2\text{O}_3/\text{NiAl}(110)$ surface under high vacuum. (c, d) Topographic image and V_{CPD} images of Pd NPs/ $\text{Al}_2\text{O}_3/\text{NiAl}(110)$ surface after saturated

120 L CO molecule. (e, f) Line profiles of height and V_{CPD} of Pd NPs on IA (blue) in (a) and (b), respectively. (g, h) Line profiles of height and V_{CPD} of Pd NPs on surface in (c) and (d), respectively. Imaging parameters: constant- Δf mode, $f_0 = 1.12$ MHz, $Q = 3304$, $A_{mp} = 800$ pm, size = 30×60 nm².

The electronic properties of CO on Pd NPs on the line defects of support were investigated by KPFM. The AFM images shown in the Figure 6.2 (a) and (b) represent the Pd NPs on IA line defects and with CO saturate, respectively. The corresponding line profiles across the Pd NPs and CO on Pd NPs were shown in the Figure 6.2 (e) and (g). The height of the NPs decreased after CO exposure can be attribute the CO adsorption, and maybe because the CO was dark contrast as shown in Figure 6.1 (b) and (d). KPFM measurements were performed during AFM imaging in the constant frequency shift mode. The dark or bright contrast in the KPFM images was used to detect the local charge state of the surface or adsorbed metal clusters. The two KPFM images in Figure 6.2 (b) and (d) were recorded simultaneously with the images in Figure 6.2 (a) and (c). The bright contrast of the Pd NPs in the CPD images indicating work function increase and negative charge, which is consistent with our previous results in chapter 5 [29]. The work function of NPs decreased upon the CO exposure that can be distinguished by the small CPD contrast and correspondingly line profiles Figure 6.2 (f) and (h). To test the correlation, we adapt the concept that change of local contact potential difference δV_{LCPD} in the following in case of the tip apex change.

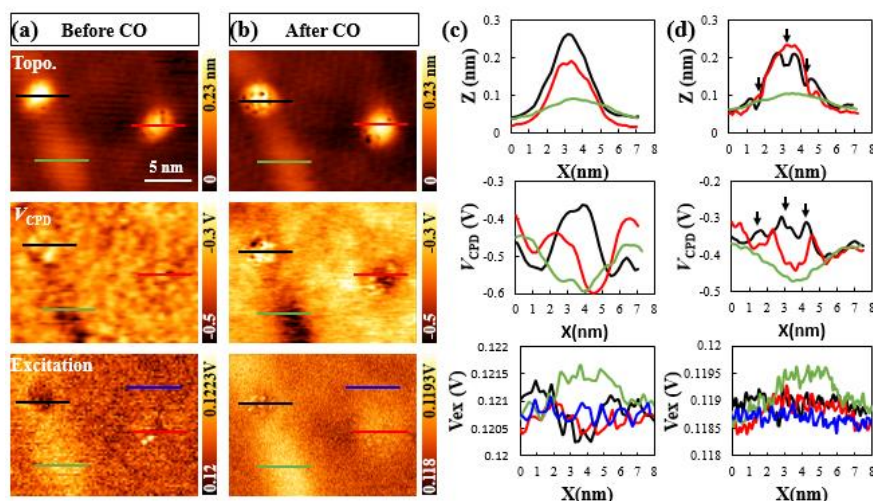


Figure 6.3 (a) Topographic, V_{CPD} and excitation images of Pd NPs/ Al_2O_3 /NiAl(110) surface under high vacuum. (b) Topographic image, V_{CPD} and excitation images of Pd NPs/ Al_2O_3 /NiAl(110) surface after saturated 120 L CO molecule. (c, d) Line profiles of height and V_{CPD} , V_{Ex} in (a) and (b), respectively.

Imaging parameters: constant- Δf mode, $f_0 = 1.12$ MHz, $Q = 3304$, $A_{mp} = 800$ pm, size = 20×15 nm² (a) $\Delta f = -46$ Hz, (b) $\Delta f = -99$ Hz.

In order to get insight of the electron transfer behaviors qualitatively and quantitatively, the KPFM measurement with subatomic resolution was performed. As shown in the Figure 6.3 (a), the Pd adsorbed on the IA and surface were negatively charged. After saturated 120 L CO molecule, the CO molecule was detected as the dark contrast on the Pd NPs as indicated by the black arrow in the Figure 6.3 (d). We also found that the most preferable adsorption site is on the Pd NP at the line defects. In addition, the change of LCPD (δV_{LCPD}) on top of NPs became small, comparing the Figure 6.3 (c) and (d), which could be explained by the electron shared between Pd atom and CO molecule. The charge state of NP on the surface even shows the positive charge obviously by the KPFM contrast, maybe indicating the less electron storage or transfer that could be used for binding with CO molecule.

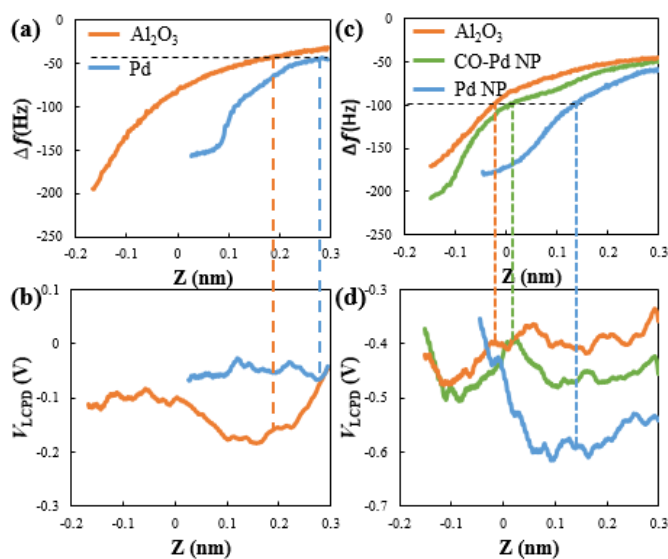


Figure 6.4 (a, b) Distance-dependent variation of the frequency shift and V_{LCPD} on top of Pd NP and bare alumina surface. (a, d) Distance-dependent variation of the frequency shift and V_{LCPD} on top of CO molecule, Pd NP and bare alumina surface.

In order to understand the LCPD with tip-sample distance and charge transfer, we perform the z spectroscopy with KPFM on Pd atom and alumina surface in Figure 6.4 (a). Meanwhile, we perform the z spectroscopy with KPFM on CO molecule, Pd atom and alumina surface Figure 6.5 (b), respectively. The zero point of the experimental Z axis defines the starting approach point of spectra

measurements, V_{LCPD} of Pd and surface slightly decreased with decreasing z , which attributed to averaging effects. The black dot line in Figure 6.4 (a) and (c) indicate the imaging frequency shift maintained for Figure 6.2 and Figure 6.3, respectively. Before CO molecule exposure, we obtained the same LCPD contrast: $V_{LCPD-Pd} > V_{LCPD-surface}$, while the LCPD contrast: $V_{LCPD-surface} > V_{LCPD-CO} > V_{LCPD-Pd}$ after CO molecule. In addition, the bias spectroscopy is performed at this regime, which doesn't show the electron transfer between tip and the CO molecule. Therefore, an appropriate way to interpret different LCPD contrast on CO molecule is that the charge redistribution.

To exclude the tip dipole moment effects, we consider mechanism of imaging. When forming the chemical bond, the Pd was completely occupied state that increase the local work function. If it is HOMO CO molecule, the local work function could be decreased, which is consistent with the experimental results. Therefore, the LOMO CO molecule in this system is suitable, which increased the local work function, to explain the higher LCPD of CO on Pd NPs.

It is difficult to interpret the KPFM measurement when it comes to the smaller tip sample distance, because of the dipole moment or induced dipole moment. Therefore, we consider to support the KPFM results from analysis of the dissipation energy of the NPs at the smaller imaging tip sample distance. The dissipation energy was calculated by the following equation:

$$Q = 2\pi \frac{E_0}{\Delta E_0} \quad (6.1)$$

$$E_0 = \frac{kA^2}{2} \quad (6.2)$$

$$\Delta E_0 = \alpha V_0 \quad (6.3)$$

$E_0, \Delta E_0, Q, A, V_0$ represent energy of cantilever, the dissipation energy of one cycle in free vibration, quality factor, oscillation amplitude, dissipated voltage signal in free vibration (displayed on the PLL). Then the α could be deduced by combining equation 6.1, 6.2 and 6.3, in the follow:

$$\alpha = \frac{\pi k A^2}{Q V_0} \quad (6.4)$$

$$\Delta E_{ts} = \alpha (V_{dis} - V_0) \quad (6.5)$$

Where V_{dis} is dissipated voltage signal obtained from the dissipated image. So that the dissipation energy ΔE_{ts} can be deduced.

Q value of the cantilever should not be much higher than the ratio $2\pi E_0 / \Delta E_{ts}$ to maintain a constant amplitude [30]. According to the dissipative image in the Figure 6.3 (b), Q value is 3 times smaller than

$2\pi E_0/\Delta E_{ts}$. Additionally, we calculated the dissipation energy for the NP on IA defect equal to 0.2812 V, which were 2.4 time larger than the dissipated voltage signal in free vibration (0.115 V), and dissipation energy variation is slight compared with the dissipation energy of surface (0.2775 V). Therefore, it indicated the dissipation interaction between tip and sample is not that large.

Furthermore, we consider the Ir-coated Si tip apex is neutral or positive, and the line defects are positive charged because the line defects always shown as the dark contrast in the KPFM images either before or after CO expose. In this regard, we consider the tip apex polarity didn't affect the KPFM contrast. As the FM-KPFM was used in this research, the AC modulation voltage intrigue the cross-talk especially in the atomic resolution KPFM images. The Sadewasser group compared the KPFM and bias-spectroscopy imaging method to conclude the V_{ac} wouldn't cause the artifact of atomic resolution, but will diminish the KPFM contrast. People may consider that topographic cross-talk when the probe moves in constant frequency-shift mode across the frontier atom of the CO and Pd. Lift-up KPFM scanning is better choice, but we can get the contrast information from the Z spectroscopy, which show the consistency at relatively large tip sample distance. Therefore, the KPFM contrast we measured could provide the physical phenomena, such as electron transfer, in the catalyst system. In conclude, we tentatively attribute the atomic KPFM contrast origin from the short-range electrostatic interaction between the tip and local sample static charge.

6.3.3 CO molecules adsorption on Pd NCs with atomic resolution

Reactant adsorption sites of novel metal catalysts are difficult to characterize precisely, which is vital for understanding heterogeneous reactions and designing efficient catalytic systems. However, even at cryogenic temperatures, a complete atomic understanding of catalytic reaction sites remains elusive, such as the variation in reactant molecule adsorption sites on metal nanoclusters (NCs). Here, we studied CO adsorption on the Pd NC of an $\text{Al}_2\text{O}_3/\text{NiAl}(110)$ surface with atomic resolution by noncontact atomic force microscopy and Kelvin probe force microscopy at room temperature. We found that CO molecules are preferentially adsorbed, saturated, and desorbed on the Pd NC on line defects compared with that of terrace. We investigated the consecutive scanning topographic AFM images of CO molecules on the Pd/ Al_2O_3 /NiAl surface and found the adsorption sites of CO molecules, which are supported by density functional theory (DFT) calculations. This result reveals that the electronic and geometric properties of Pd NCs and CO molecules are expected to provide insight into the mechanism

of Pd-based heterogeneous catalysis.

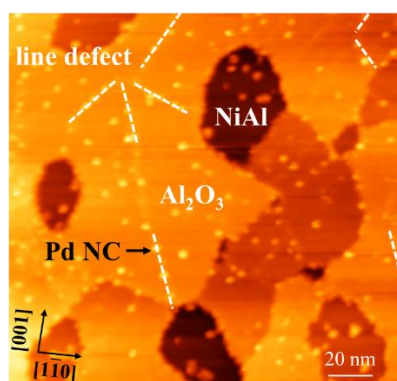


Figure 6.5 Topographic AFM image of Pd/Al₂O₃/NiAl surface at room temperature. Bright dot: Pd nanoclusters. Dashed line: line defect. Parameters: constant- Δf mode, $f_0 = 1.12$ MHz, $Q = 3304$, $A = 800$ pm, and size: 180×180 nm²

Figure 6.5 shows a large-area NC-AFM image of Pd NCs deposited on an Al₂O₃/NiAl surface, which contains a series of line defects. The line defects are nucleation sites and act as the electron transfer pathway of the Al₂O₃/NiAl(110) surface at RT [27,29]. Here, bright spots indicate Pd nanoclusters, dashed lines indicate line defects, and the dark contrast indicates the NiAl substrate; the others are Al₂O₃ domains. Next, we exposed CO molecules and investigated their adsorption behavior at the same area.

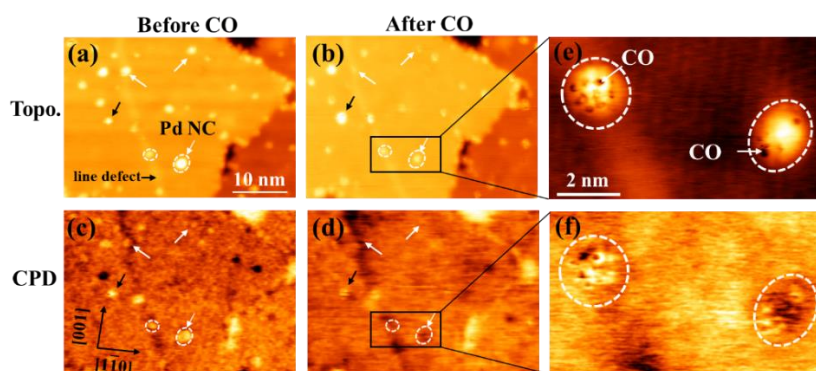


Figure 6.6 Topographic AFM and CPD images of Pd/Al₂O₃/NiAl surface. Topographic AFM images obtained (a) before and (b) after CO adsorption. CPD images obtained (c) before and (d) after CO adsorption. (e) and (f) Enlarger images of rectangles in (b) and (d), respectively. Note that after CO molecule adsorption, the Pd NCs become small as indicated by the white arrows in (a) and (b), and the CPD contrast of the Pd NCs becomes dark in (c) and (d). On the other hand, the Pd NCs become large

as indicated by the black arrow and the CPD contrast of the Pd NCs becomes bright. CO molecules as dark spots indicate preferential adsorption on line defects rather than on terraces as shown in (e). Parameters: constant- Δf mode, $f_0 = 1.12$ MHz, $Q = 3304$. Size: 85×58 nm². Enlarger size: 8.8×5 nm²

Figure 6.6 shows topographic AFM and CPD images simultaneously on Pd/Al₂O₃/NiAl surface. Figure 6.6 (a) and 6.6(b) show before and after CO adsorption, and figures 6.6(c) and 6.6(d) show CPD images corresponding to figure 6.6(a) and 6.6(b). After CO molecule adsorption, the Pd NCs become small as indicated by white arrows in figure 6.6(a) and 6.6(b), and the CPD contrast of the Pd NCs become dark in figure 6.6(c) and 6.6(d). On the other hand, the Pd NCs become large as indicated by black arrow owing to cohesion at RT and the CPD contrast of the Pd NCs becomes bright. Pd NCs adsorbed on the line defect and terrace are bright contrast in CPD images, which are negatively charged consistent with precious results [29]. To obtain insight into the adsorption activity after CO exposure to Pd/Al₂O₃/NiAl, the enlarger images were taken and are shown in figures 6.6(e) and 6.6(f). We found that more CO molecules adsorb on top of the Pd NC on line defects than on terraces, which are shown as dark contrast on the topographic images and bright contrast on the CPD image. CO molecules are preferentially adsorbed on line defects than on terraces. Moreover, the charge distribution on line defects is more negative than that on terraces owing to the adsorbed CO molecules as shown in Figure 6.6(f).

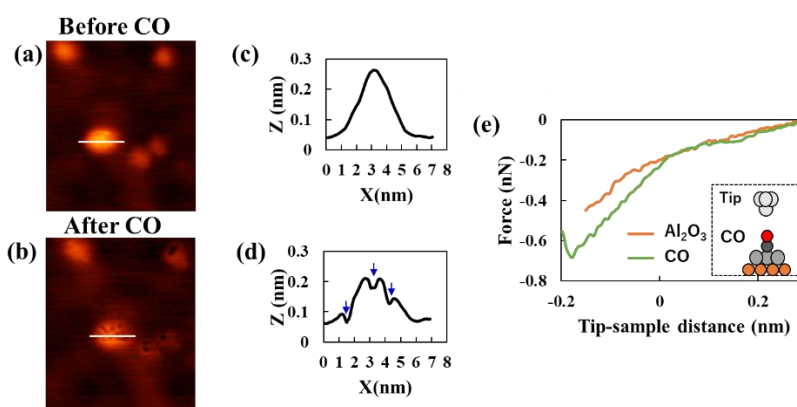


Figure 6.7 Topographic AFM images obtained before (a) and after (b) CO adsorption on Pd/Al₂O₃/NiAl surface. (c) and (d) Line profiles corresponding to (a) and (b), respectively. (e) Force curves on sites of CO and Al₂O₃.

Figure 6.7(a) and 6.7 (b) show the topographic AFM images of Pd NCs on the line defects of the

Al₂O₃/NiAl(110) surface, obtained before and after CO molecule adsorption. The line profiles were measured across the Pd NCs and CO molecule on Pd NCs as shown in Figure 6.7 (c) and 6.7 (d). It is indicated that the height of the Pd NCs decreased after the CO adsorption marked by blue arrows. The bond length of CO on the Pd NCs is around 60 pm, which is smaller than that in the gas phase [20]. In addition, the force curves were obtained on top of the CO molecule and Al₂O₃ surface as shown in Figure 6.7 (e), the inset indicates the interaction model between the tip and the CO molecule according to the previous theory [33]. The force curve of the CO molecule shows two minima at various tip sample distance compared with surface, which can be assigned to the physisorption and chemisorption minima, as shown by previous results and the theory [21]. Thus, this feature represents the interaction between O-terminated CO and metal atoms, which can be used to distinguish the CO molecule. The force deconvolution method was proposed by Sadler [34]. The minimum force is 0.68 nN, which related to the coordination number of the investigated CO molecule. Additionally, the protrusion and dark contrast of CO on the Pd NP and surface can be imaged at different tip sample distances.

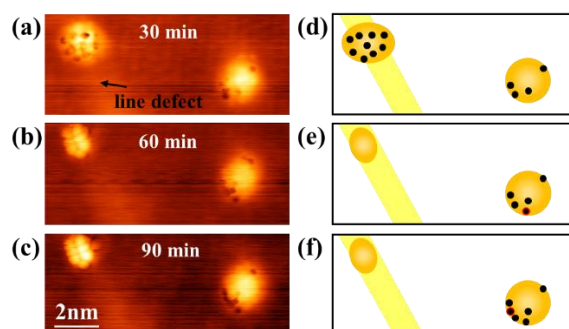


Figure 6.8 Topographic AFM images obtained after CO adsorption on Pd/Al₂O₃/NiAl surface at different time. CO adsorption at (a) 30, (b) 60, and (c) 90 min. (d-f) Schematic images of (a-c). The black and red dots represent the CO molecule. Parameter: 1800 L CO (1×10^{-6} torr).

The properties of CO molecule adsorption on the Pd/Al₂O₃/NiAl(110) surface were investigated and the results are shown in Figures 4(a-c). The Pd NC on the line defect has a higher catalytic activity for CO molecule adsorption, resulting in saturated adsorption for a certain number of CO molecules. After CO saturated adsorption on the Pd NC of the line defect, CO gradually adsorbs on the Pd NC of the terrace, as shown in Figure 6.8 (b) – 6.8(c). The number of adsorbed CO molecules affects the electronic properties of the Pd NC, which can be interpreted from the CPD images in Figure 6.6 (f), leading to the

geometry structure transformation of the Pd NC. Additionally, the Pd NC is oriented along the line defect on the $\text{Al}_2\text{O}_3/\text{NiAl}(110)$ surface. Since the adsorption of CO molecules is more stable on the Pd NC of the terrace than on that of the line defect, we will investigate the adsorption of CO molecules on the Pd NC of the terrace.

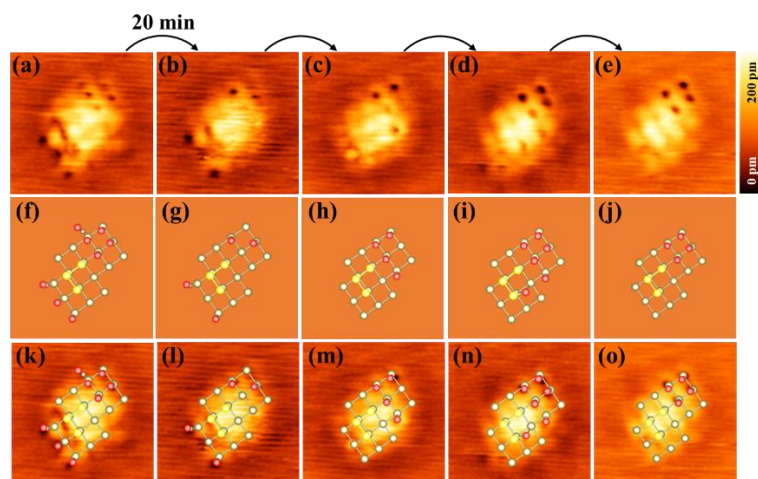


Figure 6.9 (a-e) Consecutive scanning topographic AFM images of CO molecules on Pd/ Al_2O_3 /NiAl surface after the adsorption of 120 L CO molecule at RT. (f-j) Schematic models of CO adsorption on two layers of Pd NC. (k-o) AFM images with models. Red ball: CO; gray ball: Pd atoms in the first layer; yellow ball: Pd atoms in the second layer. Imaging parameters: constant- Δf mode, $f_0 = 1.12$ MHz, $Q = 3304$, and size: 4×4 nm².

Figure 6.9(a-e) are consecutive topographic images recorded every 20 min in the constant-frequency mode. The adsorption and desorption of CO molecules on the Pd NC can be found with scanning times. Here, CO molecules are imaged as a depression contrast on different sites of the Pd NC in the AFM images, owing to the repulsive interaction with the tip apex. Figure 6.9(f-j) are schematic models of CO adsorption on two layers of the Pd NC, according to experimental results. Figure 6.9(k-o) show the AFM images with the models which match each other well. Furthermore, we calculate and assign the adsorption sites of the CO molecule as shown below.

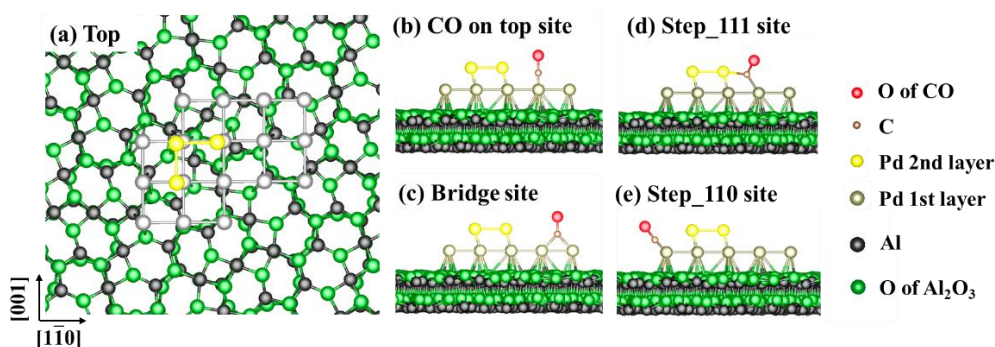


Figure 6.10 Model of Pd NC on Al_2O_3 surface. (a) Corresponding schematic model of top view of Pd NPs on Al_2O_3 surface. Side views of CO molecule on top site (b), bridge site (c), step_111 site (d), and step_110 site (e).

The CO adsorption model of the Pd NC on the Al_2O_3 surface was proposed on the basis of DFT calculations in Figure 6.10. Figure 6.10 (a) is the top view of two layers of Pd NCs adsorbed on the Al_2O_3 surface. Figures 6.10(b-e) are the side views of the CO molecule adsorbed on the top site, bridge site, step_111 site, and step_110 site on the Pd NC, respectively, and the carbon atom attaches to the Pd atom to form O termination [34,35]. In the calculation model, the O atoms and C atoms of CO molecules are indicated in red and brown balls, the first and second-layer Pd atoms are indicated by grey and yellow balls, and the Al and O atoms of Al_2O_3 the surface are indicated by black and green balls, respectively. Combining with the experimental results shown in Figure 6.9, we concluded that the adsorption of CO molecules is distributed on the top, step_110, and step_111 sites of the Pd NC. This result indicated that the adsorption energy of CO molecules is the smallest at these sites.

6.4 Conclusion

In conclusion, we have investigated the variation of LCPD after CO molecules adsorbed on Pd NPs by AFM and KPFM. We found that LCPD decreases on the Pd NPs site and it increases on CO site, which could be attributed to the CO bond with Pd NPs accompany the electron transfer from Pd NPs to the CO molecule, therefore reorganize the local charge landscape. Furthermore, compared with Pd NC of the line defects, we found that CO molecules are more stable on Pd NC of the terrace. Moreover, the Pd NCs become small with CO adsorption, whereas they become large owing to cohesion. Furthermore, from the CPD result, we found that the Pd NC is more negatively charged after CO

adsorption. Combing experimental results with the DFT calculations, we concluded that the adsorption of CO molecules on the Pd NC of terraces is preferred on the top, step_110, and step_111 sites. This result reveals that the electronic and geometric properties of Pd NCs and CO molecules are expected to provide insight into the mechanism of Pd-based heterogeneous catalysis.

Chapter 7 Oxygen-adsorption-induced Charge State Change of Pd NCs on Al₂O₃/NiAl(110) Surface

7.1 Introduction

It is generally accepted that metal nanoparticles supported on a nonreducible oxide surface catalyze CO oxidation via Langmuir-Hinshelwood (L-H) mechanisms, where O₂ and CO coadsorb onto the catalyst [1,2]. The coarsening, structure evolution and reduction/oxidation of catalytically active metal clusters are often accelerated by the presence of gases [3-5]. In a previous study, it was shown that the enhanced sintering of alumina-supported Pt clusters in an oxidizing atmosphere could be explained by a thermodynamic preference for the detachment of the PtO₂ volatile oxide instead of Pt atoms [6]. The CO-induced coalescence of Pd adatoms supported on the Fe₃O₄(001) surface at room temperature has been fully investigated using a real-time-scale scanning tunneling microscope, and Pd-carbonyl species have been found to be responsible for mobility [7]. Despite this early success, the electronic property of the novel metal composition during an exposure of molecular oxygen has not been found on a time scale that allows specific sintering and mobility processes to be followed. The charge state of the metal nanocluster on the oxide surface during an exposure of molecular oxygen is unspecified in many studies, which enables different species recognition and the modification of the electrostatic potential energy landscape of the surface.

Kelvin probe force microscopy (KPFM) is a complementary technique of noncontact atomic force microscopy (NC-AFM), in which the electrostatic interaction caused by an AC bias voltage is compensated during topographic imaging [8-10]. This compensation voltage corresponds to the local work function difference between the sample and the tip, whereas for insulating films, it gives information about the local surface charge [11]. Therefore, KPFM is a powerful tool for investigating catalyst activity and selectivity [12-15]. Compared with the averaging of chemical shifts over the catalyst by X-ray photoelectron spectroscopy, KPFM allows us to follow the individual size and shape of metal catalysts that are adsorbed at different sites of the support, for example, terraces, steps, or kinks, and to distinguish the charge state and composition of adsorbed species [16]. When the charge transfer

between Pd nanoclusters and the substrate can be determined on each nano-catalyst in a gas environment, much progress can be made in catalyst characterization.

7.2 Methods

The experiments were performed using a home-built combined NC-AFM and KPFM under ultrahigh vacuum (UHV) at room temperature (RT). The NC-AFM system was operated in the frequency-modulation detection method with constant oscillation amplitude (800 pm). All images were obtained in the constant-frequency mode. As our KPFM setup applies an AC voltage (V_{AC}) at frequency ω as well as a DC voltage (V_{DC}) to the sample, V_{DC} nullifies the f_{AC} component of oscillating electrical forces, providing V_{CPD} between the tip and the sample surface. Detailed information was provided in our previous work [17-19]. In our case, the local contact potential difference (LCPD) voltage can be determined with a feedback loop using KPFM.

The NiAl(110) surface was prepared with repeated cycles of Ar ion sputtering and annealing at 1000 °C. The alumina thin film was obtained by exposing NiAl(110) to 1000 L of O₂ followed by annealing at 380 °C [20, 21]. Palladium was evaporated onto the alumina thin film surfaces using an electron beam evaporator (Omicron EFM 3) at room temperature. The Pd flux was calibrated and verified by AFM measurements on the Pd-exposed NiAl(110) crystal. The evaporator deposition rate was 6.4×10^{17} atoms/cm²·s (about 0.13 ML/min) [22]. Molecular oxygen (purity 99.9%) was exposed to the scanning chamber at different background pressures. An Ir-coated Si cantilever (NANOSENDORS) was excited to vibrate at its resonance frequency of 1.12 MHz.

7.3 Results

7.3.1 Investigation of oxygen-adsorption-induced sintering

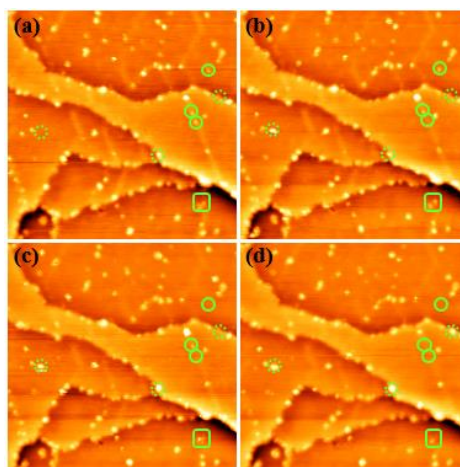


Figure 7.1 Consecutive NC-AFM images of the Pd/Al₂O₃ system acquired of the same surface region at RT after exposure to 6 L of molecular oxygen. The time intervals following the introduction of the molecular oxygen were (a) 0 min, (b) 28 min, (c) 72 min, (d) 116 min. Examples of Pd nanoclusters that grow/decay are marked with dotted/solid circles, respectively. Sintering of Pd nanoclusters are marked with rectangles. Imaging parameters: constant- Δf mode, $V_{AC}=500$ mV, $f_{AC}=190$ Hz, size 120×120 nm².

The catalytic system Pd/Al₂O₃/NiAl(110) was studied at low O₂ exposure (6 Langmuir (L), $1\text{ L} = 10^{-6}$ Torr/s). The morphology of Pd nanoclusters (0.13 ML) on an Al₂O₃/NiAl(110) surface is shown in Figure 1. Alumina thin film contains line defects such as antiphase domain boundaries (APDBs) on the A/B domain and reflection domain boundaries (RDBs) (between A/A, B/B and A/B domains) that appear as bright lines on AFM images [23, 24]. Atomic-scale AFM images of the APDBs show an oxygen-deficient structure along the midline and diagonal of the minimum unit cell of the Al₁₀O₁₃ thin film [24, 25]. This unusual structure favors the adsorption of metal and large molecules [26, 27]. As shown in our results, the preferential adsorption sites are step edges and domain boundaries. Note that the adsorption behavior of Pd nanoclusters to APDBs is driven by thermal kinetic energy, indicating that nanoclusters can be thermally stable at 300 K [28]. Figure 1a shows that Pd nanoclusters were immobile for more than 2 h under UHV conditions. Pd nanoclusters begin to grow, decay, and sintering immediately upon the introduction of O₂. Consecutive images were then acquired on the same surface

area as a function of time, as shown in Figure 1b-d. As captured in the series of images, some Pd nanoclusters (green circle) gradually decayed, whereas some nucleated and grew (dot circle). In one example, the sintering process began at 72 min and hopping occurred at 116 min (see Figure 7.2). These behaviors are consistent with particle migration, which is affected by temperature, and the detachment of metal atoms (or metal complexes), and diffusion of these species over the support [29].

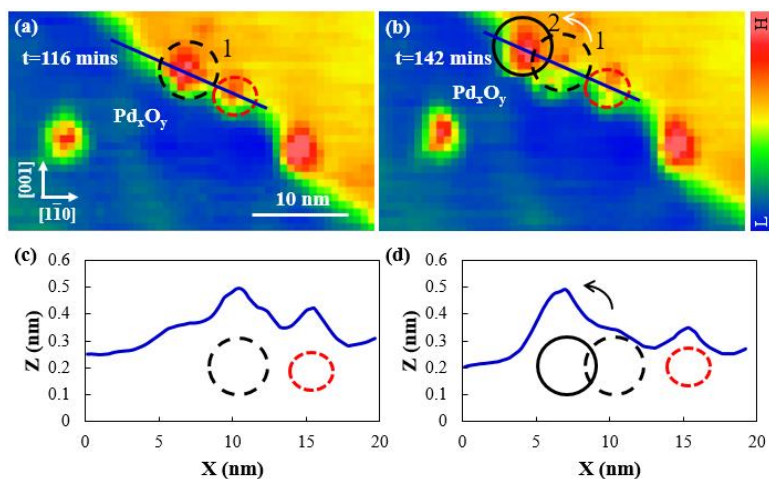


Figure 7.2 O₂ induced hopping of Pd_xO_y nanocluster. (a, b) Time-labeled images depicted from same sample area as Figure 2 and 3. (c, d) Corresponding line profiles of as indicated in panel (a) and (b).

These data show Pd_xO_y nanoclusters hopping from position 1 to 2, which supports the assumption that Pd nanoclusters are activated by the oxygen.

7.3.2 Oxygen-adsorption-induced charge state change

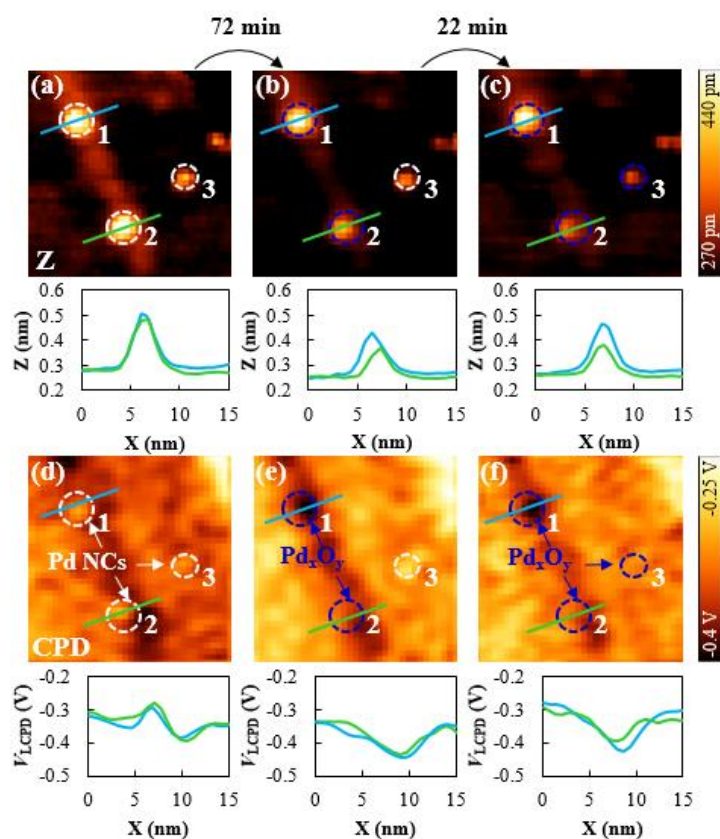


Figure 7.3 O₂-induced charge state change of Pd nanoclusters. Consecutive NC-AFM and KPFM images of the Pd/ Al₂O₃ system at RT after exposure to 6 L of molecular oxygen. Three images (a-c) are selected from a longer AFM movie acquired over the same sample area at 0 min, 72 min and 94 min. Imaging parameters: constant- Δf mode, $V_{AC} = 500$ mV, $f_{AC} = 190$ Hz, size of 30×30 nm².

Figure 7.3(a-c) show small cutouts from the much larger area (50×50 nm²) in the AFM movie. The corresponding LCPD images are presented in Figure 7.3(d-f). Figure 7.3(a) shows the as-prepared Pd nanocluster before oxygen exposure. The image series in Figure 7.3(b, c) shows the same area successively recorded after exposure to molecular oxygen at room temperature. After the time of the image in Figure 7.3(a), the scanning UHV chamber is backfilled with molecular oxygen (oxygen pressure $P_{O_2} = 1 \times 10^{-9}$ Torr, dosage ~ 6 L).

The diameter of Pd nanoclusters 1 and 2 are almost the same, subsequently, Pd nanoclusters 2 and 3 decreased in diameter with time. A negatively charge state can be found for three Pd nanoclusters, caused by electron tunneling from the substrate. Note that the relatively charge state refers to the charge state compared with alumina surface. A positively charged state can be found for the line defects, which

is due to the oxygen-deficiency structure. A LCPD contrast reversal occurs for nanocluster 1, which means that a negatively charged Pd nanocluster 1 becomes positively charged after 72 min of molecular oxygen exposure. Pd nanocluster 3 changed its charge state after 22 min. As explained further below, the charge state change can be assigned to a new species, Pd_xO_y . Note that the small height variation of the cluster in Figure 7.3 (a, b) could be caused by a dull tip apex.

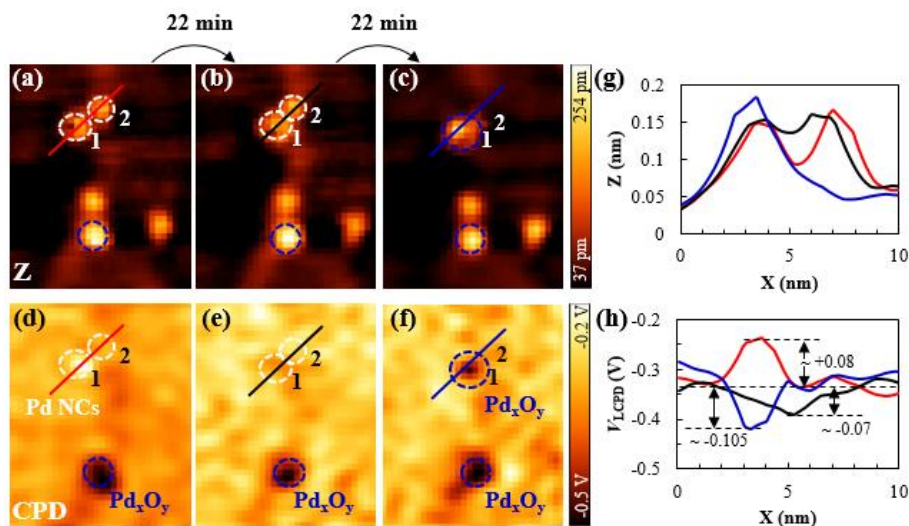


Figure 7.4 O_2 -induced sintering of Pd nanoclusters. The three images (a-c) are selected from a longer AFM movie acquired over the same sample area at 28 min, 50 min, and 72 min after exposure to 6 L of molecular oxygen. Corresponding line profiles of Z and V_{LCPD} are taken through the center of nanocluster sites. Imaging parameters: constant- Δf mode, $V_{\text{AC}} = 500$ mV, $f_{\text{AC}} = 190$ Hz, size of 120×90 nm^2 .

Because the oxidation reaction does not occur synchronously, despite the fast interaction process of nanoclusters, some sintering with charge state change is observed at RT. The AFM and KPFM images in Figure 3 show selected frames from a series of images of a different area from those in Figure 7.3. Pd nanoclusters 1 and 2 adsorb on the alumina surface with a distance of 3.5 nm from each other, as shown in Figure 7.4(a). Then, nanocluster 2 approaches nanocluster 1 in Figure 3(b), and in Figure 3(c), nanocluster 1 is replaced by a bright feather with an apparently larger diameter. In the vicinity of nanoclusters 1 and 2, this is the only change that indicates the process of O_2 -induced sintering of nanoclusters.

The corresponding LCPD images are presented in Figure 3(d-f). Nanocluster 1 is negatively charged, whereas nanocluster 2 is neutral. When nanocluster migration causes the two initially separated clusters

to come into contact with each other, they lose the contrast of the LCPD, as shown in Figure 7.3(e). The product of sintering has a positive charge and is inert to the further oxygen exposure. We propose that sintering occurs by “easy” detachment and terrace diffusion of a Pd_xO_y species, as discussed further below.

The positively charged species are believed to be Pd_xO_y species formed on the alumina surface during molecular oxygen exposure. The oxygen-adsorption-induced charge state change of nanoclusters can be observed on the line defects of the alumina surface. This is attributed to the possibility of transferring the electron of the line defects. The sintering of nanoclusters is greatly influenced by the molecular oxygen density.

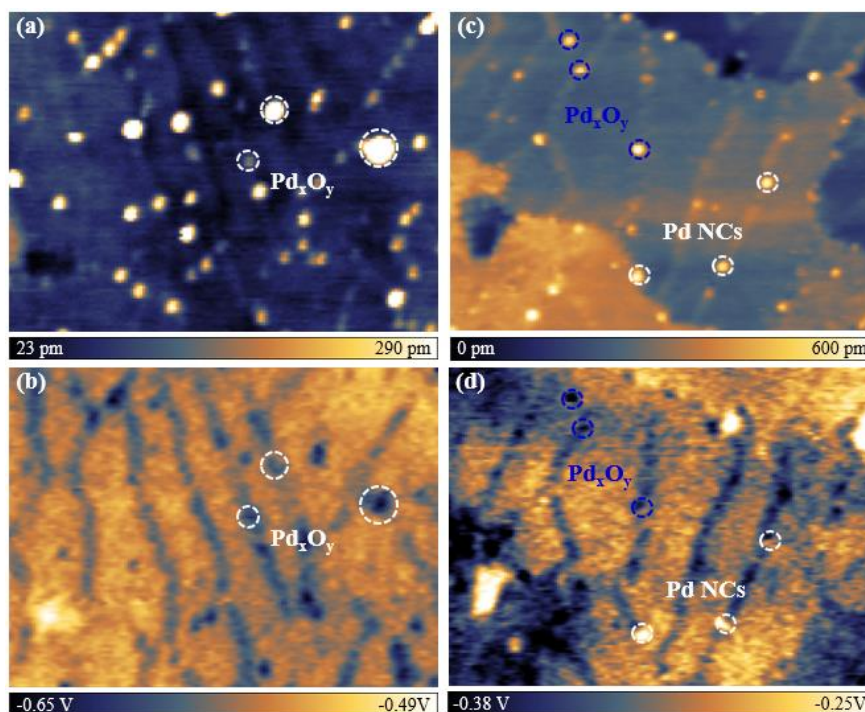


Figure 7.5 (a) NC-AFM and (b) KPFM images of $\text{Al}_2\text{O}_3/\text{NiAl}(110)$ surface following deposition of 0.13 ML Pd at RT after exposure to 360 L of molecular oxygen. (c) NC-AFM and (d) KPFM images after sample annealing at 250 °C. Imaging parameters: constant- Δf mode, $V_{AC} = 500$ mV, $f_{AC} = 190$ Hz, size of 120×90 nm².

After dosing a higher amount of O_2 into the chamber (360 L), the majority of the species observed in KPFM images are positively charged, as shown in Figure 7.5(b). The average diameter of nanoclusters increased with increasing oxygen pressure, which can be attributed to the formation of metal complexes.

The metal complex influences particle adsorption stability by reducing the complex detachment barrier or via desorption of volatile metal complexes.

As shown in Figure 7.5(c), the apparent diameter and density of the Pd_xO_y nanoclusters decrease after heating the surface to 250 °C. Note that thermal energy helps the sintering of nanoclusters, but the nanocluster diameter was reduced, suggesting desorption of the weakly binding oxygen or oxygen-induced structural change of the Pd_xO_y nanoclusters. In addition, the charge state of 18% of nanoclusters adsorbed on the line defects and step edge of the surface becomes negative, as shown in Figure 7.5(d). This opens up the possibility of the Pd nanocluster reappearing after the desorption of the weakly binding oxygen of Pd_xO_y nanoclusters.

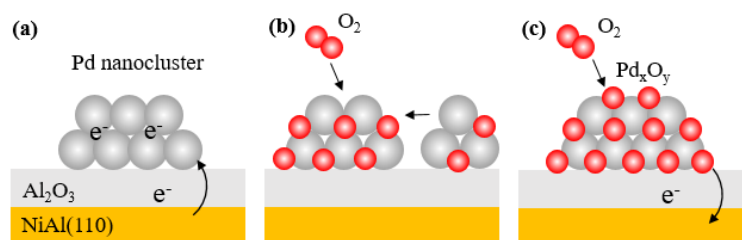


Figure 7.6 Oxidation mechanism of Pd nanoclusters on $\text{Al}_2\text{O}_3/\text{NiAl}(110)$ in molecular oxygen.

The present Pd/ Al_2O_3 -catalyzed oxidation may thus proceed via the mechanism proposed above and shown in Figure 7.6. The chemical adsorption of oxygen preferentially occurs on the negatively charged nanocluster. At higher temperature and pressure (470 K and 10^{-4} Pa), a surface oxide can form [30]. In our results, the observation of the negligible change in the charge state suggests the experimental scenario for the formation of oxidized Pd nanocluster catalyst (Pd_xO_y). We found that the sintering of nanoclusters occurs by the diffusion of a Pd_xO_y species.

7.4 Discussion

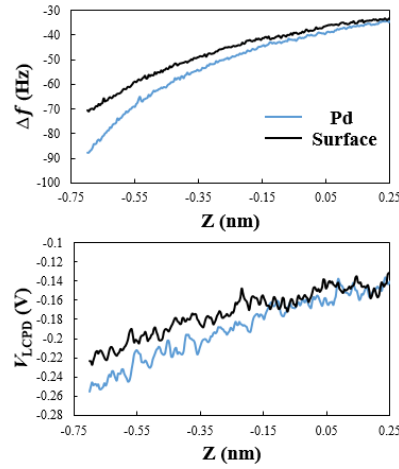


Figure 7.7 Distance-dependent variation of the frequency shift and V_{LCPD} on top of the positively charged Pd and bare alumina surface.

Tip-sample distance-dependent variation of the frequency shift and V_{LCPD} over positively charged nanocluster and bare alumina surface by performing Z spectroscopy with KPFM on. We found that V_{LCPD} of nanocluster is smaller than the alumina surface in all force range. There is no contrast reverse for the V_{LCPD} at even short-range force range. All the images in the main text were taken at $\Delta f = -52$ Hz.

In our experiment, we performed KPFM measurement at the large tip-sample interaction regimes, where the measurement of the local charge distribution without a tip induced dipole. As shown Figure 7.7, we observe a decrease in the LCPD of Pd_xO_y nanoclusters, which can be distinguished from the substrate in a wide range of tip-sample distance. This reduction in the LCPD can be interpreted in terms of charge transfer to the substrate. In standard topography model, the tip-surface convolution affects the height and diameter measurement of the cluster, but especially the height. Therefore, we have performed the detuning imaging method to measure the nanocluster, and the diameter was found to be around 2 nm with subatomic resolution, as shown in Figure 7.8. This value is almost equal to the diameter measured in the constant frequency mode without high resolution, as shown in Figure 7.8. Therefore, a sharp tip enabled the nanocluster diameter to be measured with less tip-sample convolution in our experiment.

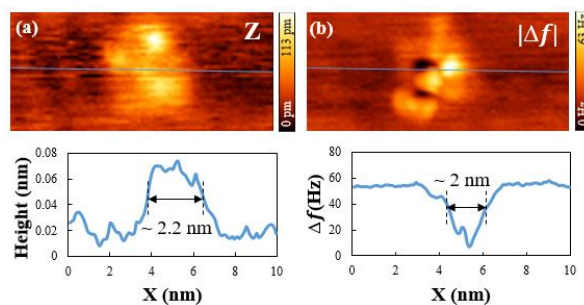


Figure 7.8. (a) NC-AFM images in constant- Δf mode, $\Delta f = -40$ Hz, size 10×4.5 nm². (b) Detuning imaging at $\Delta f = -48$ Hz, size of 10×4.5 nm².

In constant- Δf mode, Δf is kept constant by the distance control loop. In the detuning imaging mode, the scanning direction is changed until it is parallel to the surface, a less negative value is chosen for the Δf , which is far away from the surface and the tip is put at a safe distance [1]. The diameter was defined from the full width at half maximum (FWHM) [2].

The LCPD acquired by KPFM show the same qualitative contrast for all functionalized tip terminations. This contrast resembled the contrast of the electrostatic field of the sample [31]. Although the surface potential is dependent on the electrostatic signature of neutral, charged, and polar tips, the LCPD contrast can represent the charge distribution with less tip influence [32]. Thus, the tip apex may influence the topographic images, especially at the atomic resolution, while the effects to LCPD contrast can be neglected in the simple model. In addition, the change in the charge state of individual nanoclusters (see Figure 7.3) and the partial change in the charge state of the nanocluster observed after annealing (see Figure 7.5) also suggest that change of charge state of nanocluster is not tip-induced. It is reasonable to conclude that the change in the LCPD contrast of nanoclusters is caused by the chemical interactions.

O₂ dissociation on the Pd surface was extensively studied at different temperatures [33], by temperature-programmed desorption (TPD), STM, and DFT as well as KPFM [14, 34-36]. Oxygen adsorption accompanies significant electron transfer to O₂, creating a surface dipole toward the surface or the formation of superoxo species [14, 37]. However, in our results, we observed a positively charged nanocluster, which does not fit either of the above case. Oxygen molecule bound to a Pd nanocluster may exist, which occurs with a positive charge of the metal nanocluster or at low temperature, but we measured a negatively charged Pd nanocluster and performed the experiment at room temperature. Thus,

it can be assumed that the stability of the oxidized Pd_xO_y nanocluster depends on its interaction with the surface and the pressure of molecular oxygen. The oxidized Pd_xO_y can be regarded as a semiconductor particle that has a band gap rather than a metallic Pd nanocluster. We speculate that the oxidized Pd nanoclusters participated in the CO oxidation through the L-H or Eley-Rideal mechanism, which is being investigated in ongoing experiments [38, 39].

7.5 Conclusion

We investigated the change in the charge state of Pd nanocatalysts on a model system, Pd/Al₂O₃/NiAl(110), on a real-time scale during an exposure of molecular oxygen using NC-AFM and KPFM. By following the evolution of individual species, we found that the Pd nanocluster can be oxidized by O₂ at room temperature, leading to the formation of metal complex Pd_xO_y nanoclusters. The Pd_xO_y shows a positive charge in KPFM images, and its stability depends on the interaction with surface and the pressure of molecular oxygen. It is the major sintering species in contrast with the stable Pd nanocluster on the alumina surface. In addition, Pd_xO_y contains weakly binding oxygen that can be removed after annealing at a higher temperature. Hence, the change in the charge state of the oxidized nanocluster can be reversed by annealing, providing a cyclic oxidation process and possible support for the concept of conversion from carbon monoxide to carbon dioxide. However, a lack of atomic resolution makes it difficult to demonstrate the structure of the oxidized nanocluster and the charge redistribution within. Using KPFM to elucidate the chemical reaction is still challenging.

Chapter 8 Summary and outlook

8.1 Summary

In my research, I focused on investigating the charge state of Pd NPs on Al₂O₃/NiAl(110) on catalyzed oxidation of CO by noncontact atomic force microscopy (AFM) and Kelvin probe force microscopy (KPFM) at room temperature (RT). The KPFM detects electrostatic forces between tip and surface and compensates them by applying a dc bias voltage that is adjusted by feedback control. KPFM images could give the charge landscape of the Pd NPs on Al₂O₃/NiAl(110) with high accuracy. The classical electrostatic theory is combined with KPFM to extract the charge state of the Pd NPs in this catalytic system.

Firstly, we deduced the size dependence of charge state of the Pd NPs by measuring the local contact potential difference (LCPD) of Pd NPs on the alumina surface through KPFM and classical electrostatic model for the spheres. The Pd NPs are negatively charged on the Al₂O₃/NiAl(110) surface, which is not attainable in previous study. The charge state of Pd NPs is increased with increasing the size. The electron in the Pd NPs tunneling from the substrate.

Secondly, we deduced the size dependence of the charge state of the CO molecule on Pd NPs by measuring the LCPD of Pd NPs on the alumina surface through KPFM. The general charge state of CO molecule on Pd NPs decreased compared with the charge state of Pd NPs. In addition, we found that the charge state decreases on the Pd NPs site and it increases on the CO site, which could be attributed to the CO bond with Pd NPs accompanying the electron transfer from Pd NPs to the CO molecule, therefore reorganizing the local charge landscape. Furthermore, comparing with Pd nanocluster (NC) of the line defects, we found that CO molecules are more stable on Pd NC of the terrace. Moreover, the Pd NCs becomes small with CO adsorption, whereas it becomes large due to cohesion. Combined experimental results with DFT calculations, we concluded that the adsorption sites of CO molecules on Pd NC of the terrace are preferred on top, step₁₁₀, and step₁₁₁ sites. This result reveals that the electronic and geometric properties of Pd NCs and CO molecules are expected to provide insight into the mechanism of Pd-based heterogeneous catalysis.

Thirdly, we have investigated that charge state evolution of the Pd NPs is studied during exposure of molecular oxygen. We speculated that the Pd NPs could be oxidized by oxygen molecules, leading to Pd_xO_y , which shows a positive charge on the alumina surface.

Our results can provide a good starting point for understanding size sensitive for a catalytic reaction by investigating size related electronic and geometric properties of the Pd NPs or Pd NPs with CO and O_2 in the nanoscale.

8.2 Outlook

It is significant to produce the optimal size distribution of particles instead of a wide range of sizes, which could increase the active sites ratio, by analyzing the charge state and even introducing the quantum size effect. Therefore, specialized size nanoparticles should be designed to catalyze a specific reaction in the future. Based on our results and high-resolution nano-technique, we believe our final goal could be realized.

References

Chapter 1

1. Panwar, N. L., Kaushik, S. C. Kothari, S. Role of renewable energy sources in environmental protection: A review. *Renew. Sust. Energ. Rev.* **2011**, *15*, 1513-1524.
2. Anastas, P. T., Bartlett, L. B., Kirchoff, M. M., Williamson, T. C. The role of catalysis in the design, development, and implementation of green chemistry. *Catal. Today.* **2000**, *55*, 11-22.
3. Chowdhury, N., Hossain, C. A., Longo, M., Yaïci, W. Optimization of solar energy system for the electric vehicle at university campus in Dhaka, Bangladesh. *Energies* **2018**, *11*, 2433.
4. Televan, A. Pros and cons of electric cars. **2020**.
5. Kašpar, J., Fornasiero, P. Hickey, N. Automotive catalytic converters: current status and some perspectives. *Catalysis today*, 2003, *77*, 419-449.
6. Rood S, Eslava S, Manigrasso A. Recent advances in gasoline three-way catalyst formulation: A review. *Proc. Inst. Mech. Eng. D: J. Automob. Eng.* **2020**, *234*: 936-949.
7. Czepkiewicz, M., Heinonen, J., Ottelin, J. Why do urbanites travel more than do others? A review of associations between urban form and long-distance leisure travel. *Environ. Res. Lett.* **2018**, *13* 073001.
8. Maurer, F., Gänzler, A., Lott, P., Betz, B., Votsmeier, M., Loridant, S., Grunwaldt, J. D. Spatiotemporal Investigation of the Temperature and Structure of a Pt/CeO₂ Oxidation Catalyst for CO and Hydrocarbon Oxidation during Pulse Activation. *Ind. Eng. Chem. Res.* **2021**, *60*, 6662-6675.
9. Damyanova, S., Bueno, J. M. C. Effect of CeO₂ loading on the surface and catalytic behaviors of CeO₂-Al₂O₃-supported Pt catalysts. *Appl. Catal. A: Gen.* **2003**, *253*, 135-150.
10. Jones, J. C. P., Roberts, J. B., Bernard, P., & Jackson, R. A. *A simplified model for the dynamics of a three-way catalytic converter* (No. 2000-01-0652). *SAE Tech. Pap.* **2000**.
11. Jaeger, R. M., Kühlenbeck, H., Freund, H. J., Wuttig, M., Hoffmann, W., Franchy, R., Ibach, H. Formation of a well-ordered aluminium oxide overlayer by oxidation of NiAl (110). *Surf. Sci.* **1991**, *259*, 235-252.
12. Hammer, B., Morikawa, Y., Nørskov, J. K. CO chemisorption at metal surfaces and

- overlayers. *Phys. Rev. Lett.* **1996**, *76*, 2141.
13. Nilius, N., Ganduglia-Pirovano, M. V., Brázdová, V., Kulawik, M., Sauer, J. Freund, H. J. Counting electrons transferred through a thin alumina film into Au chains. *Phys. Rev. Lett.* **2008**, *100*, 096802.
 14. Nilius, N., Ganduglia-Pirovano, M. V., Brázdová, V., Kulawik, M., Sauer, J. Freund, H. J. Electronic properties and charge state of gold monomers and chains adsorbed on alumina thin films on NiAl (110). *Phys. Rev. B* **2010**, *81*, 045422.
 15. Bäumer, M., Frank, M., Heemeier, M., Kühnemuth, R., Stempel, S., Freund, H. J. Nucleation and growth of transition metals on a thin alumina film. *Surf. Sci.* **2000**, *454*, 957-962.
 16. Beniya, A., Higashi, S., Ohba, N., Jinnouchi, R., Hirata, H., & Watanabe, Y. CO oxidation activity of non-reducible oxide-supported mass-selected few-atom Pt single-clusters. *Nat. Commun.* **2020**, *11*, 1-10.
 17. Bartels, L.; Meyer, G.; Rieder, K. H. Basic steps involved in the lateral manipulation of single CO molecules and rows of CO molecules. *Chem. Phys. Lett.* **1997**, *273*, 371-375.
 18. Lin, X.; Yang, B.; Benia, H. M.; Myrach, P.; Yulikov, M.; Aumer, A.; Rocker, J. Charge-mediated adsorption behavior of CO on MgO-supported Au clusters. *J. Am. Chem. Soc.* **2010**, *132*, 7745-7749.
 19. Ternes, M.; Lutz, C. P.; Hirjibehedin, C. F.; Giessibl, F. J.; Heinrich, A. J. The force needed to move an atom on a surface. *Science* **2008**, *319*, 1066-1069.
 20. Sun, Z; Boneschanscher, M. P; Swart, I. Quantitative atomic force microscopy with carbon monoxide terminated tips. *Phys. Rev. Lett.* **2011**, *106*, 046104.
 21. Schwarz, A.; Köhler, A., Grenz, J.; Wiesendanger, R. Detecting the dipole moment of a single carbon monoxide molecule. *Appl. Phys. Lett.* **2014**, *105*, 011606.
 22. Huber, F.; Berwanger, J.; Polesya, S., Mankovsky, S.; Ebert, H.; Giessibl, F. J. Chemical bond formation showing a transition from physisorption to chemisorption. *Science* **2019**, *366*, 235-238.
 23. Parkinson, G. S., Novotny, Z., Argentero, G., Schmid, M., Pavelec, J., Kosak, R., Diebold, U. Carbon monoxide-induced adatom sintering in a Pd-Fe₃O₄ model catalyst. *Nat. Mater.* **2013**, *12*, 724-728.

24. Berwanger, J., Polesya, S., Mankovsky, S., Ebert, H., Giessibl, F. J. Atomically resolved chemical reactivity of small Fe clusters. *Phys. Rev. Lett.* **2020**, *124*(9), 096001.
25. Hulva, J., Meier, M., Bliem, R., Jakub, Z., Kraushofer, F., Schmid, M., Parkinson, G. S. Unraveling CO adsorption on model single-atom catalysts. *Science* **2021**, *371*, 375-379.
26. Ryan, P. T. P., Meier, M., Jakub, Z., Balajka, J., Hulva, J., Payne, D. J., Duncan, D. A. Probing structural changes upon carbon monoxide coordination to single metal adatoms. *J. Chem. Phys.* **2020**, *152*, 051102.
27. Jakub, Z., Hulva, J., Ryan, P. T., Duncan, D. A., Payne, D. J., Bliem, R., Parkinson, G. S. Adsorbate-induced structural evolution changes the mechanism of CO oxidation on a Rh/Fe₃O₄(001) model catalyst. *Nanoscale* **2020**, *12*, 5866-5875.
28. Graham, M. D., Kevrekidis, I. G., Asakura, K., Lauterbach, J., Krischer, K., Rotermund, H. H., Ertl, G. Effects of boundaries on pattern formation: Catalytic oxidation of CO on platinum. *Science* **1994**, *264*, 80-82.
29. Krok, F., Sajewicz, K., Konior, J., Goryl, M., Piatkowski, P., Szymonski, M. Lateral resolution and potential sensitivity in Kelvin probe force microscopy: Towards understanding of the sub-nanometer resolution. *Phys. Rev. B* **2008**, *77*, 235427.
30. Arai, T., Tomitori, M. Observation of electronic states on Si (111)-(7×7) through short-range attractive force with noncontact atomic force spectroscopy. *Phys. Rev. Lett.* **2004**, *93*, 256101.
31. Okamoto, K., Yoshimoto, K., Sugawara, Y., Morita, S. KPFM imaging of Si (1 1 1) 53×53-Sb surface for atom distinction using NC-AFM. *Appl. Surf. Sci.* **2003**, *210*, 128-133.
32. Yurtsever, A., Fernández-Torre, D., Onoda, J., Abe, M., Morita, S., Sugimoto, Y., Pérez, R. The local electronic properties of individual Pt atoms adsorbed on TiO₂ (110) studied by Kelvin probe force microscopy and first-principles simulations. *Nanoscale*, **2017**, *9*, 5812-5821.
33. Sasahara, A., Uetsuka, H., Onishi, H., Onishi, H. Individual Na Adatoms on TiO₂ (110)-(1×1) Surface Observed Using Kelvin Probe Force Microscope. *Jpn. J. Appl. Phys.* 2004, *43*, 4647.
34. Kitamura, S. I., Suzuki, K., Iwatsuki, M., Mooney, C. B. Atomic-scale variations in contact potential difference on Au/Si (111) 7×7 surface in ultrahigh vacuum. *Appl. Surf. Sci.* 2000, *157*, 222-227.
35. Barth, C., Henry, C. R. Kelvin probe force microscopy on MgO (001) surfaces and supported

- Pd nanoclusters. *J. Phys. Chem. C* **2009**, *113*, 247-253.
36. Barth, C., Henry, C. R. Gold nanoclusters on alkali halide surfaces: charging and tunneling. *Appl. Phys. Lett.* **2006**, *89*, 252119.
 37. Gross, L., Mohn, F., Liljeroth, P., Repp, J., Giessibl, F. J., Meyer, G. Measuring the charge state of an adatom with noncontact atomic force microscopy. *Science*, **2009**, *324*, 1428-1431.
 38. Meyer, G., Amer, N. M. Simultaneous measurement of lateral and normal forces with an optical-beam-deflection atomic force microscope. *Appl. Phys. Lett.* **1990**, *57*, 2089-2091.

Chapter 2

1. Binnig, G.; Quate, C. F. and Gerber, C. *Phys. Rev. Lett.* **1986**, *56*, 930.
2. C. Argento and R. H. French, *J. Appl. Phys* **1996**, *80*, 6081.
3. S. Hudlet, M. Saint Jeana, C. Guthmann, and J. Berger, *Eur. Phys. J. B* **1998**, *2*, 5-10
4. M. Guggisberg, M. Bammerlin, Ch. Loppacher, O. Pfeiffer, A. Abdurixit, V. Barwich, R. Bennewitz, A. Baratoff, *Phys. Rev. B* **2000**, *61*, 11151.
5. Giessibl, F. J. Advances in atomic force microscopy. *Reviews of modern physics* **2003**, *75*, 949.
6. Sader, J. E. and Jarvis, S.P. *Appl. Phys. Lett.* **2004**, *84*, 1801-1803.
7. N. D. Lang and W. Kohn, *Phys. Rev. B* **1970**, *1*, 4555.
8. Cardona, M. and Ley, L. *Springer-Verlag Berlin Heidelberg New York*, **1978**, 26.
9. S. Hudlet, M. Saint Jeana, C. Guthmann, and J. Berger, *Eur. Phys. J. B* **1998**, *2*, 5-10
10. Fukuma, T.; Kobayashi, K.; Yamada, H. and Matsushige, K. *Rev. Sci. Instrum.* **2004**, *75*, 4589.
11. Sascha Sadewasser, Pavel Jelinek, Chung-Kai Fang, Oscar Custance, Yusaku Yamada, Yoshiaki Sugimoto, Masayuki Abe, and Seizo Morita, *Phys. Rev. Lett.* **2009**, *103*, 266103.
12. Laurent Nony, Adam S. Foster, Franck Bocquet, and Christian Loppacher, *Phys. Rev. Lett.* **2009**, **103**, 036802
13. Leo Gross, Fabian Mohn, Peter Liljeroth, Jascha Repp, Franz J. Giessibl, Gerhard Meyer, *Science* **2009**, *324*, 1428-1431.
14. Hong Jing Chung, Ayhan Yurtsever, Yoshiaki Sugimoto, Masayuki Abe and Seizo Morita, *Appl. Phys. Lett.* **2011**, *99*, 123102
15. Ryohei Kokawa, Masahiro Ohta, Akira Sasahara and Hiroshi Onishi, *Chem. Asian J.* **2012**, *7*, 1251-1255.

16. BingKai Yuan, PengCheng Chen, Jun Zhang, ZhiHai Cheng, XiaoHui Qiu, Chen Wang, *Chin Sci Bull*, **2013**, *58*, 3630-3635.
17. Fabian Mohn, Leo Gross, Nikolaj Moll and Gerhard Meyer, *Nat. Nanotechnology*. **2012**, *7*, 227-231
18. Bruno Schuler, Shi-Xia Liu, Yan Geng, Silvio Decurtins, Gerhard Meyer, and Leo Gross, *Nano Lett.* **2014**, *14*, 3342-3346.

Chapter 3

1. Darby, A. P. and Pellegrino, S. *J. Intell. Mater. Syst. Struct.*, **1997**, *8*, 1001.
2. Watanabe, S. and Fujii, T. *Rev. Sci. Instrum.* **1996**, *67*, 3898-3903.
3. Giessibl, J. and Trafas, B. M. *Rev. Sci. Instrum.* **1994**, *65*, 1923-1929.
4. Meyer, G. and Amer., N. M. *Appl. Phys. Lett.* **1990**, *51*, 2089-2091.
5. Yokoyama, K.; Ochi, T.; Uchihashi, T.; Ashino, M.; Sugawara, Y.; Suehira N.; and Morita, S. *Rev. Sci. Instrum.* **2000**, *71*, 128.
6. Fukuma, T.; Kimura, M.; Kobayashi, K.; Matsushige, K.; Yamada, H. *Rev. Sci. Inst.* **2005**, *76*, 053704.
7. Fukuma, T. and Jarvis, S. P. *Rev. Sci. Inst.* **2006**, *77*, 043701.
8. Moreno-Flores, S.; Toca-Herrera, J. L. *CRC Press*. **2012**.
9. Li, Y. J.; Brndiar, J.; Naitoh, Y.; Sugawara, Y.; Štich, I. *Nanotechnology*. **2015**, *26*, 505704.
10. EFM 3 - Scienta Omicron

Chapter 4

1. Kresse, G., Schmid, M., Napetschnig, E., Shishkin, M., Köhler, L., Varga, P. Structure of the ultrathin aluminum oxide film on NiAl (110). *Science*. **2005** *308*, 1440-1442.
2. Simon, G. H., König, T., Rust, H. P., Heyde, M., Freund, H. J. Atomic structure of the ultrathin alumina on NiAl (110) and its antiphase domain boundaries as seen by frequency modulation dynamic force microscopy. *New J. Phys.* **2009**, *11*, 093009.
3. Li, Y. J.; Brndiar, J.; Naitoh, Y.; Sugawara, Y.; Štich, I. Atomic force microscopy identification of Al-sites on ultrathin aluminum oxide film on NiAl (110). *Nanotechnology*. **2015**, *26*, 505704.
4. Nilius, N., Wallis, T. M., Ho, W. Influence of a Heterogeneous Al₂O₃ Surface on the Electronic Properties of Single Pd Atoms. *Phys. Rev. Lett.* **2003**, *90*, 046808.

5. Schmid, M., Shishkin, M., Kresse, G., Napetschnig, E., Varga, P., Kulawik, M., Freund, H. J. Oxygen-deficient line defects in an ultrathin aluminum oxide film. *Phys. Rev. Lett.* **2006**, *97*, 046101.
6. Heinke, L., Lichtenstein, L., Simon, G. H., König, T., Heyde, M., Freund, H. J. Structure and electronic properties of step edges in the aluminum oxide film on NiAl (110). *Phys. Rev. B* **2010**, *82*, 075430.
7. Nilius, N., Ganduglia-Pirovano, M. V., Brázdová, V., Kulawik, M., Sauer, J., Freund, H. J. Electronic properties and charge state of gold monomers and chains adsorbed on alumina thin films on NiAl (110). *Phys. Rev. B* **2010**, *81*, 045422.
8. Simon, G. H., Heyde, M., Freund, H. J. Imaging and manipulation of adatoms on an alumina surface by noncontact atomic force microscopy. *Journal of Physics: Condensed Matter* **2012** *24*, 084007.
9. Lopez, N., Janssens, T. V. W., Clausen, B. S., Xu, Y., Mavrikakis, M., Bligaard, T., & Nørskov, J. K. On the origin of the catalytic activity of gold nanoparticles for low-temperature CO oxidation. *Journal of Catalysis* **2004**, *223*, 232-235.
10. Beniya, A.; Higashi, S.; Ohba, N.; Jinnouchi, R.; Hirata, H.; Watanabe, Y. CO oxidation activity of non-reducible oxide-supported mass-selected few-atom Pt single-clusters. *Nat. Commun.* **2020**, *11*, 1-10.
11. Barth, C., Henry, C. R. Kelvin probe force microscopy on MgO (001) surfaces and supported Pd nanoclusters. *J. Phys. Chem. C* **2009**, *113*, 247-253.
12. Long, L. H., Walsh, A. D. Remarks on the structure of carbon monoxide. *J. Chem. Soc., Faraday trans.* **1947**, *43*, 342-351.
13. Jaffé, H. H., Orchin, M. Hybridization in carbon monoxide. *Tetrahedron* **1960**, *10*, 212-214.
14. Yoon, B., Häkkinen, H., Landman, U., Wörz, A. S., Antonietti, J. M., Abbet, S., Heiz, U. Charging effects on bonding and catalyzed oxidation of CO on Au₈ clusters on MgO. *Science* **2005** *307*, 403-407.
15. Grönbeck, H., Barth, C. Oxygen Adsorption on Graphene-Encapsulated Palladium Nanoparticles Imaged by Kelvin Probe Force Microscopy. *J. Phys. Chem. C*, **2019**, *123*, 24615-24625.

16. Montemore, M. M., van Spronsen, M. A., Madix, R. J., Friend, C. M. O₂ activation by metal surfaces: implications for bonding and reactivity on heterogeneous catalysts. *Chem. Rev.* **2017**, *118*, 2816-2862.

Chapter 5

1. Yoon, B.; Häkkinen, H.; Landman, U.; Wörz, A. S.; Antonietti, J. M.; Abbet, S.; Heiz, U. *Science*, **2005**, *307*, 403-407.
2. Beniya, A.; Higashi, S.; Ohba, N.; Jinnouchi, R.; Hirata, H.; Watanabe, Y. CO oxidation activity of non-reducible oxide-supported mass-selected few-atom Pt single-clusters. *Nat. Commun.* **2020**, *11*, 1-10.
3. Wu, T.; Kaden, W. E.; Kunkel, W. A.; Anderson, S. L. Size-dependent oxidation of Pd_n (n ≤ 13) on alumina/NiAl (110): Correlation with Pd core level binding energies. *Surf. Sci.* **2009**, *603*, 2764-2770.
4. Yamauchi, T.; Tabuchi, M.; Nakamura, A. Size dependence of the work function in InAs quantum dots on GaAs (001) as studied by Kelvin force probe microscopy. *Appl. Phys. Lett.* **2004**, *84*, 3834-3836.
5. Kaden, W. E.; Wu, T.; Kunkel, W. A.; Anderson, S. L. Electronic structure controls reactivity of size-selected Pd clusters adsorbed on TiO₂ surfaces. *Science*, **2009**, *326*, 826-829.
6. Cargnello, M.; Doan-Nguyen, V. V.; Gordon, T. R.; Diaz, R. E.; Stach, E. A.; Gorte, R. J.; Murray, C. B. Control of metal nanocrystal size reveals metal-support interface role for ceria catalysts. *Science*, **2013**, *341*, 771-773.
7. Allian, A. D.; Takanabe, K.; Furdala, K. L.; Hao, X.; Truex, T. J.; Cai, J.; Iglesia, E. Chemisorption of CO and mechanism of CO oxidation on supported platinum nanoclusters. *J. Am. Chem. Soc.* **2011**, *133*, 4498-4517.
8. Cui, Y.; Stiehler, C.; Nilus, N.; Freund, H. J. Probing the electronic properties and charge state of gold nanoparticles on ultrathin MgO versus thick doped CaO films. *Phys. Rev. B.* **2015**, *92*, 075444.
9. Libuda, J.; Winkelmann, F.; Bäumer, M.; Freund, H. J.; Bertrams, T.; Neddermeyer, H.; Müller, K. Structure and defects of an ordered alumina film on NiAl (110). *Surf. Sci.* **1994**, *318*, 61-73.
10. Kresse, G.; Schmid, M.; Napetschnig, E.; Shishkin, M.; Köhler, L.; Varga, P. Structure of the

- ultrathin aluminum oxide film on NiAl (110). *Science*. **2005**, *308*, 1440-1442.
11. Schmid, M.; Shishkin, M.; Kresse, G.; Napetschnig, E.; Varga, P.; Kulawik, M.; Freund, H. J. Oxygen-deficient line defects in an ultrathin aluminum oxide film. *Phys. Rev. Lett.* **2006**, *97*, 046101.
 12. Heemeier, M.; Stempel, S.; Shaikhutdinov, S. K.; Libuda, J.; Bäumer, M.; Oldman, R. J.; Freund, H. J. On the thermal stability of metal particles supported on a thin alumina film. *Surf. Sci.* **2003**, *523*, 103-110.
 13. Wang, Y. G.; Yoon, Y.; Glezakou, V. A.; Li, J.; Rousseau, R. The role of reducible oxide-metal cluster charge transfer in catalytic processes: new insights on the catalytic mechanism of CO oxidation on Au/TiO₂ from ab initio molecular dynamics. *J. Am. Chem. Soc.* **2013**, *135*, 10673-10683.
 14. Repp, J.; Meyer, G.; Olsson, F. E.; Persson, M. Controlling the charge state of individual gold adatoms. *Science* **2004**, *305*, 493-495.
 15. Steurer, W.; Repp, J.; Gross, L.; Scivetti, I.; Persson, M.; Meyer, G. Manipulation of the charge state of single Au atoms on insulating multilayer films. *Phys. Rev. Lett.* **2015**, *114*, 036801.
 16. Gross, L.; Mohn, F.; Liljeroth, P.; Repp, J.; Giessibl, F. J.; Meyer, G. Measuring the charge state of an adatom with noncontact atomic force microscopy. *Science*. **2009**, *324*, 1428-1431.
 17. Zhang, Q.; Li, Y. J.; Wen, H. F.; Adachi, Y.; Miyazaki, M.; Sugawara, Y.; Štich, I. Measurement and Manipulation of the Charge State of an Adsorbed Oxygen Adatom on the Rutile TiO₂(110)-1×1 Surface by nc-AFM and KPFM. *J. Am. Chem. Soc.* **2018**, *140*, 15668-15674.
 18. Adachi, Y.; Wen, H. F.; Zhang, Q.; Miyazaki, M.; Sugawara, Y.; Sang, H.; Li, Y. J. Tip-induced control of charge and molecular bonding of oxygen atoms on the rutile TiO₂(110) surface with atomic force microscopy. *ACS Nano*. **2019**, *13*, 6917-6924.
 19. Barth, C.; Henry, C. R. Kelvin probe force microscopy on MgO (001) surfaces and supported Pd nanoclusters. *J. Phys. Chem. C*, **2009**, *113*, 247-253.
 20. König, T.; Simon, G. H.; Rust, H. P.; Pacchioni, G.; Heyde, M.; Freund, H. J. Measuring the charge state of point defects on MgO/Ag (001). *J. Am. Chem. Soc.* **2009**, *131*, 17544-17545.
 21. Garcia, R.; Perez, R. Dynamic atomic force microscopy methods. *Surf. Sci. Rep.* **2002**, *47*, 197-301.

22. Miyazaki, M.; Wen, H. F.; Zhang, Q.; Adachi, Y.; Brndiar, J.; Štich, I.; Sugawara, Y. Imaging the surface potential at the steps on the rutile TiO₂ (110) surface by Kelvin probe force microscopy. *Beilstein J. Nanotechnology*. **2019**, *10*, 1228-1236.
23. Li, Y. J.; Brndiar, J.; Naitoh, Y.; Sugawara, Y.; Štich, I. Atomic force microscopy identification of Al-sites on ultrathin aluminum oxide film on NiAl (110). *Nanotechnology* **2015**, *26*, 505704.
24. Bäumer, M.; Frank, M.; Heemeier, M.; Kühnemuth, R.; Stempel, S.; Freund, H. J. Nucleation and growth of transition metals on a thin alumina film. *Surf. Sci.* **2000**, *454*, 957-962.
25. Napetschnig, E.; Schmid, M.; Varga, P. Pd, Co and Co–Pd clusters on the ordered alumina film on NiAl (110): Contact angle, surface structure and composition. *Surf. Sci.* **2007**, *601*, 3233-3245.
26. Zhang, Y.; Pluchery, O.; Caillard, L.; Lamic-Humblot, A. F.; Casale, S.; Chabal, Y. J.; Salmeron, M. Sensing the charge state of single gold nanoparticles via work function measurements. *Nano Lett.* **2015**, *15*, 51-55.
27. Simon, G. H.; König, T.; Rust, H. P.; Heyde, M.; Freund, H. J. Atomic structure of the ultrathin alumina on NiAl (110) and its antiphase domain boundaries as seen by frequency modulation dynamic force microscopy. *New J. Phys.* **2009**, *11*, 093009.
28. Nilius, N.; Kulawik, M.; Rust, H. P.; Freund, H. J. Defect-induced gap states in Al₂O₃ thin films on NiAl (110). *Phys. Rev. B.* **2004**, *69*, 121401.
29. Beniya, A.; Isomura, N.; Hirata, H.; Watanabe, Y. Lateral displacement in soft-landing process and electronic properties of size-selected Pt₇ clusters on the aluminum oxide film on NiAl (110). *Chem. Phys. Lett.* **2013**, *576*, 49-54.
30. Nilius, N.; Wallis, T. M.; Ho, W. Influence of a Heterogeneous Al₂O₃ Surface on the Electronic Properties of Single Pd Atoms. *Phys. Rev. Lett.* **2003**, *90*, 046808.
31. Song, W.; Yoshitake, M. A work function study of ultra-thin alumina formation on NiAl (110) surface. *Appl. Surf. Sci.* **2005**, *251*, 14-18.
32. Halder, A.; Curtiss, L. A.; Fortunelli, A.; Vajda, S. Perspective: Size selected clusters for catalysis and electrochemistry. *J. Chem. Phys.* **2018**, *148*, 110901.
33. Napetschnig, E.; Schmid, M.; Varga, P. Pd, Co and Co–Pd clusters on the ordered alumina film on NiAl(110): Contact angle, surface structure and composition. *Surf. Sci.* **2007**, *601*, 3233-

3245.

34. Kim, J.; Qin, S.; Yao, W.; Niu, Q.; Chou, M. Y.; Shih, C. K. Quantum size effects on the work function of metallic thin film nanostructures. *Proc. Natl. Acad. Sci. U.S.A.* **2010**, *107*, 12761-12765
35. Wagner, C.; Green, M. F.; Leinen, P.; Deilmann, T.; Krüger, P.; Rohlfing, M.; Tautz, F. S. Scanning quantum dot microscopy. *Phys. Rev. Lett.* **2015**, *115*, 026101.

Chapter 6

1. Schloegl, R. Heterogeneous catalysis. *Angew. Chem. Int. Ed.* **2015**, *54*, 3465-3520.
2. Rothenberg, G. Catalysis: concepts and green applications. *John Wiley & Sons.* **2017**.
3. Kunz, L., Maier, L., Tischer, S., Deutschmann, O. Modeling the rate of heterogeneous reactions. *ChemInform*, **2012**, *43*.
4. Klaewkla, R.; Arend, M.; Hoelderich, W. F. A review of mass transfer controlling the reaction rate in heterogeneous catalytic systems. *London: INTECH Open Access Publisher* **2011**. *5*.
5. Lin, X.; Nilius, N.; Sterrer, M.; Koskinen, P.; Häkkinen, H.; Freund, H. J. Characterizing low-coordinated atoms at the periphery of MgO-supported Au islands using scanning tunneling microscopy and electronic structure calculations. *Physical Review B.* **2010**, *81*, 153406.
6. Gotterbarm, K.; Späth, F.; Bauer, U.; Bronnbauer, C.; Steinrück, H. P.; Papp, C. Reactivity of graphene-supported Pt nanocluster arrays. *ACS catalysis.* **2015**, *5*, 2397-2403.
7. Yoon, B.; Häkkinen, H.; Landman, U.; Wörz, A. S.; Antonietti, J. M.; Abbet, S.; Heiz, U. Charging effects on bonding and catalyzed oxidation of CO on Au₈ clusters on MgO. *Science.* **2005**, *307*, 403-407.
8. Beniya, A.; Higashi, S.; Ohba, N.; Jinnouchi, R.; Hirata, H.; Watanabe, Y. CO oxidation activity of non-reducible oxide-supported mass-selected few-atom Pt single-clusters. *Nat. Commun.* **2020**, *11*, 1-10.
9. Reşitoğlu, İ. A.; Altinişik, K.; Keskin, A. The pollutant emissions from diesel-engine vehicles and exhaust after treatment systems. *Clean Technol. Environ. Policy.* **2015** *17*, 15-27.
10. Van Vaerenbergh, B.; Lauwaert, J.; Vermeir, P.; Thybaut, J. W.; De Clercq, J. Towards high-performance heterogeneous palladium nanoparticle catalysts for sustainable liquid-phase reactions. *React. Chem. Eng.* **2020**, *5*, 1556-1618.

11. Kunz, S.; Schweinberger, F. F.; Habibpour, V.; Röttgen, M.; Harding, C.; Arenz, M.; Heiz, U. Temperature Dependent CO Oxidation Mechanisms on Size-Selected Clusters. *J. Phys. Chem. C*. **2010**, *114*, 1651-1654.
12. Mistry, H.; Reske, R.; Zeng, Z.; Zhao, Z. J.; Greeley, J.; Strasser, P.; Cuenya, B. R. Exceptional Size-Dependent Activity Enhancement in the Electroreduction of CO₂ over Au Nanoparticles. *J. Am. Chem. Soc.* **2014**, *136*, 16473-16476.
13. Hadjiivanov, K. I.; Vayssilov, G. N. Characterization of oxide surfaces and zeolites by carbon monoxide as an IR probe molecule. *Adv. Catal.* **2002**, *47*, 305-511.
14. Jakub, Z.; Hulva, J.; Ryan, P. T.; Duncan, D. A.; Payne, D. J.; Bliem, R.; Schmid, M. Adsorbate-induced structural evolution changes the mechanism of CO oxidation on a Rh/Fe₃O₄(001) model catalyst. *Nanoscale*, **2020**, *12*, 5866-5875.
15. Wolter, K.; Seiferth, O.; Kuhlenbeck, H.; Bäumer, M.; Freund, H. J. Infrared spectroscopic investigation of CO adsorbed on Pd aggregates deposited on an alumina model support. *Surf. Sci.* **1998**, *399*, 190-198.
16. Bartels, L.; Meyer, G.; Rieder, K. H. Basic steps involved in the lateral manipulation of single CO molecules and rows of CO molecules. *Chem. Phys. Lett.* **1997**, *273*, 371-375.
17. Lin, X.; Yang, B.; Benia, H. M.; Myrach, P.; Yulikov, M.; Aumer, A.; Rocker, J. Charge-mediated adsorption behavior of CO on MgO-supported Au clusters. *J. Am. Chem. Soc.* **2010**, *132*, 7745-7749.
18. Ternes, M.; Lutz, C. P.; Hirjibehedin, C. F.; Giessibl, F. J.; Heinrich, A. J. The force needed to move an atom on a surface. *Science*, **2008**, *319*, 1066-1069.
19. Sun, Z.; Boneschanscher, M. P.; Swart, I. Quantitative atomic force microscopy with carbon monoxide terminated tips. *Phys. Rev. Lett.* **2011**, *106*, 046104.
20. Schwarz, A.; Köhler, A.; Grenz, J.; Wiesendanger, R. Detecting the dipole moment of a single carbon monoxide molecule. *Appl. Phys. Lett.* **2014**, *105*, 011606.
21. Huber, F.; Berwanger, J.; Polesya, S.; Mankovsky, S.; Ebert, H.; Giessibl, F. J. Chemical bond formation showing a transition from physisorption to chemisorption. *Science*, **2019**, *366*, 235-238.
22. Berwanger, J.; Polesya, S.; Mankovsky, S.; Ebert, H.; Giessibl, F. J. Atomically resolved

- chemical reactivity of small Fe clusters. *Phys. Rev. Lett.* **2020**, *124*, 096001.
23. Miyazaki, M.; Wen, H. F.; Zhang, Q.; Adachi, Y.; Brndiar, J.; Štich, I.; Sugawara, Y. Imaging the surface potential at the steps on the rutile TiO₂ (110) surface by Kelvin probe force microscopy. *Beilstein J. Nanotechnol.* **2019**, *10*, 1228-1236.
 24. Adachi, Y.; Wen, H. F.; Zhang, Q.; Miyazaki, M.; Sugawara, Y.; Li, Y. J. Elucidating the charge state of an Au nanocluster on the oxidized/reduced rutile TiO₂(110) surface using non-contact atomic force microscopy and Kelvin probe force microscopy. *Nanoscale Adv.* **2020**, *2*, 2371-2375.
 25. Zhang, Q.; Li, Y. J.; Wen, H. F.; Adachi, Y.; Miyazaki, M.; Sugawara, Y.; Štich, I. Measurement and Manipulation of the Charge State of an Adsorbed Oxygen Adatom on the Rutile TiO₂(110)-1×1 Surface by nc-AFM and KPFM. *J. Am. Chem. Soc.* **2018**, *140*, 15668-15674.
 26. Bäumer, M.; Frank, M., Heemeier, M.; Kühnemuth, R.; Stempel, S.; Freund, H. J. Nucleation and growth of transition metals on a thin alumina film. *Surf. Sci.* **2000**, *454*, 957-962.
 27. Li, Y. J.; Brndiar, J.; Naitoh, Y.; Sugawara, Y.; Štich, I. Atomic force microscopy identification of Al-sites on ultrathin aluminum oxide film on NiAl (110). *Nanotechnology*, **2015**, *26*, 505704.
 28. Napetschnig, E.; Schmid, M.; Varga, P. Pd, Co and Co–Pd clusters on the ordered alumina film on NiAl (110): Contact angle, surface structure and composition. *Surf. Sci.* **2007**, *601*, 3233-3245.
 29. Zou, S.; Yokoyama, H.; Sugawara, Y.; Li, Y. J. Size Dependence of Charge State of Pd Nanoparticles on Al₂O₃/NiAl (110) Surface by Kelvin Probe Force Microscopy. *J. Phys. Chem. C.* **2020**. *124*, 21641-21645.
 30. Giessibl F J. Advances in atomic force microscopy. *Rev. Mod. Phys.* **2003**, *75*, 949.
 31. Gameel, K. M., Sharafeldin, I. M., Abourayya, A. U., Biby, A. H., & Allam, N. K. Unveiling CO adsorption on Cu surfaces: new insights from molecular orbital principles. *Phys. Chem. Chem. Phys.* **2018**, *20*, 25892-25900.
 32. Broden, G.; Rhodin, T. N.; Brucker, C.; Benbow, R.; Hurych, Z. Synchrotron radiation study of chemisorptive bonding of CO on transition metals-Polarization effect on Ir (100). *Surf. Sci.* **1976**, *59*, 593-611.
 33. Sung, S. S. Hoffmann, R. How carbon monoxide bonds to metal surfaces. *J. Am. Chem. Soc.*

1985, 107, 578-584.

34. Sader, J.E. and Jarvis, S.P. Accurate formulas for interaction force and energy in frequency modulation force spectroscopy. *Appl. Phys. Lett.* **2004**, 84, 1801-1803.

Chapter 7

1. Beniya, A.; Higashi, S.; Ohba, N.; Jinnouchi, R.; Hirata, H.; Watanabe, Y. CO oxidation activity of non-reducible oxide-supported mass-selected few-atom Pt single-clusters. *Nat. Commun.* **2020**, 11, 1-10.
2. Kale, M. J.; Christopher, P. Utilizing quantitative in situ FTIR spectroscopy to identify well-coordinated Pt atoms as the active site for CO oxidation on Al₂O₃-supported Pt catalysts. *ACS Catal.* **2016**, 6, 5599-5609.
3. Bartholomew, C. H. Mechanisms of catalyst deactivation. *Applied Catalysis A: General*, **2001**, 212, 17-60.
4. Campbell, C. T.; Parker, S. C.; Starr, D. E. The effect of size-dependent nanoparticle energetics on catalyst sintering. *Science*, **2002**, 298, 811-814.
5. Moulijn, J. A.; Van Diepen, A. E.; Kapteijn, F. Catalyst deactivation: is it predictable?: What to do? *Applied Catalysis A: General*, **2001**, 212, 3-16.
6. Harris, P. J. F. Growth and structure of supported metal catalyst particles. *Int. Mater. Rev.* **1995**, 40, 97-115.
7. Parkinson, G. S.; Novotny, Z.; Argentero, G.; Schmid, M.; Pavelec, J.; Kosak, R.; Diebold, U. Carbon monoxide-induced adatom sintering in a Pd-Fe₃O₄ model catalyst. *Nat. Mater.* **2013**, 12, 724-728.
8. Melitz, W.; Shen, J.; Kummel, A. C.; Lee, S. Kelvin probe force microscopy and its application. *Surf. Sci. Rep.* **2011**, 66, 1-27.
9. Kou, L.; Li, Y. J.; Kamijyo, T.; Naitoh, Y.; Sugawara, Y. Investigation of the surface potential of TiO₂ (110) by frequency-modulation Kelvin probe force microscopy. *Nanotechnology*, **2016**, 27, 505704.
10. Enevoldsen, G. H.; Glatzel, T.; Christensen, M. C.; Lauritsen, J. V.; Besenbacher, F. Atomic scale Kelvin probe force microscopy studies of the surface potential variations on the TiO₂(110) surface. *Phys. Rev. Lett.* **2008**, 100, 236104.

11. Sadewasser, S.; Jelinek, P.; Fang, C. K.; Custance, O.; Yamada, Y.; Sugimoto, Y.; Morita, S. New insights on atomic-resolution frequency-modulation Kelvin-probe force-microscopy imaging of semiconductors. *Phys. Rev. Lett.* **2009**, *103*, 266103.
12. Barth, C.; Henry, C. R. Kelvin probe force microscopy on MgO (001) surfaces and supported Pd nanoclusters. *J. Phys. Chem. C*, **2009**, *113*, 247-253.
13. Baris, B.; Alchaar, M.; Prasad, J.; Gauthier, S.; Dujardin, E.; Martrou, D. Controlling the electric charge of gold nanoplatelets on an insulator by field emission nc-AFM. *Appl. Phys. Lett.* **2018**, *112*, 113101.
14. Grönbeck, H.; Barth, C. Oxygen Adsorption on Graphene-Encapsulated Palladium Nanoparticles Imaged by Kelvin Probe Force Microscopy. *J. Phys. Chem. C*, **2019**, *123*, 24615-24625.
15. Grönbeck, H.; Barth, C. Revealing carbon phenomena at palladium nanoparticles by analyzing the work function. *J. Phys. Chem. C*, **2019**, *123*, 4360-4370.
16. Kokawa, R.; Ohta, M.; Sasahara, A.; Onishi, H. Kelvin probe force microscopy study of a Pt/TiO₂ catalyst model placed in an atmospheric pressure of N₂ environment. *Chem.: Asian J.* **2012**, *7*, 1251-1255.
17. Miyazaki, M.; Wen, H. F.; Zhang, Q.; Adachi, Y.; Brndiar, J.; Štich, I.; Li, Y. J.; Sugawara, Y. Imaging the surface potential at the steps on the rutile TiO₂ (110) surface by Kelvin probe force microscopy. *Beilstein J. Nanotechnol.* **2019**, *10*, 1228-1236.
18. Adachi, Y.; Wen, H. F.; Zhang, Q.; Miyazaki, M.; Sugawara, Y.; Li, Y. J. Elucidating the charge state of an Au nanocluster on the oxidized/reduced rutile TiO₂(110) surface using non-contact atomic force microscopy and Kelvin probe force microscopy. *Royal Society of Chemistry, Nanoscale Advances*, **2020**, *2*, 2371-2375.
19. Zhang, Q.; Li, Y. J.; Wen, H. F.; Adachi, Y.; Miyazaki, M.; Sugawara, Y.; Štich, I. Measurement and Manipulation of the Charge State of an Adsorbed Oxygen Adatom on the Rutile TiO₂(110)-1×1 Surface by nc-AFM and KPFM. *J. Am. Chem. Soc.* **2018**, *140*, 15668-15674.
20. Li, Y. J.; Brndiar, J.; Naitoh, Y.; Sugawara, Y.; Štich, I. Atomic force microscopy identification of Al-sites on ultrathin aluminum oxide film on NiAl (110). *Nanotechnology* **2015**, *26*, 505704.
21. Bäumer, M.; Frank, M.; Heemeier, M.; Kühnemuth, R.; Stempel, S.; Freund, H. J. Nucleation

- and growth of transition metals on a thin alumina film. *Surf. Sci.* **2000**, *454*, 957-962.
22. Napetschnig, E.; Schmid, M.; Varga, P. Pd, Co and Co–Pd clusters on the ordered alumina film on NiAl (110): Contact angle, surface structure and composition. *Surf. Sci.* **2007**, *601*, 3233-3245.
 23. Simon, G. H.; König, T.; Rust, H. P.; Heyde, M.; Freund, H. J. Atomic structure of the ultrathin alumina on NiAl (110) and its antiphase domain boundaries as seen by frequency modulation dynamic force microscopy. *New J. Phys.* **2009**, *11*, 093009.
 24. Nilius, N.; Kulawik, M.; Rust, H. P.; Freund, H. J. Defect-induced gap states in Al₂O₃ thin films on NiAl (110). *Phys. Rev. B.* **2004**, *69*, 121401.
 25. Kresse, G.; Schmid, M.; Napetschnig, E.; Shishkin, M.; Köhler, L.; Varga, P. Structure of the ultrathin aluminum oxide film on NiAl (110). *Science*, **2005**, *308*, 1440-1442.
 26. Beniya, A.; Isomura, N.; Hirata, H.; Watanabe, Y. Morphology and chemical states of size-selected Ptn clusters on an aluminium oxide film on NiAl (110). *Phys. Chem. Chem. Phys.* **2014**, *16*, 26485-26492.
 27. Simon, G. H.; Heyde, M.; Freund, H. J. Imaging and manipulation of adatoms on an alumina surface by noncontact atomic force microscopy. *J. Phys. Condens. Matter.* **2012**, *24*, 084007.
 28. Beniya, A.; Isomura, N.; Hirata, H.; Watanabe, Y. Lateral displacement in soft-landing process and electronic properties of size-selected Pt₇ clusters on the aluminum oxide film on NiAl (110). *Chem. Phys. Lett.* **2013**, *576*, 49-54.
 29. Layson, A. R.; Evans, J. W.; Thiel, P. A. Additive-enhanced coarsening and smoothing of metal films: Complex mass-flow dynamics underlying nanostructure evolution. *Phys. Rev. B* **2002**, *65*, 193409.
 30. Voogt, E. H.; Mens, A. J. M.; Gijzeman, O. L. J.; Geus, J. W. Adsorption of Oxygen and Surface Oxide Formation on Pd(111) and Pd Foil Studied with Ellipsometry, LEED, AES and XPS. *Surf. Sci.* **1997**, *373*, 210-220.
 31. Mohn, F.; Gross, L.; Moll, N.; Meyer, G. Imaging the charge distribution within a single molecule. *Nat. Nanotechnology.* **2012**, *7*, 227-231.
 32. Barth, C.; Hynninen, T.; Bielecki, M.; Henry, C. R.; Foster, A. S.; Esch, F.; Heiz, U. AFM tip characterization by Kelvin probe force microscopy. *New J. Phys.* **2010**, *12*, 093024.

33. Nolan, P. D.; Lutz, B. R.; Tanaka, P. L.; Mullins, C. B. Direct Verification of a High-Translational-Energy Molecular Precursor to Oxygen Dissociation on Pd(111). *Surf. Sci.* **1998**, 419, L107-L113.
34. Kolasinski, K. W.; Cemic, F.; Hasselbrink, E. O₂/Pd(111). Clarification of the Correspondence between Thermal Desorption Features and Chemisorption States. *Chem. Phys. Lett.* **1994**, 219, 113-117.
35. Zheng, G.; Altman, E. I. The oxidation of Pd (111). *Surf. Sci.* **2000**, 462, 151-168.
36. Todorova, M.; Reuter, K.; Scheffler, M. Oxygen overlayers on Pd (111) studied by density functional theory. *J. Phys. Chem. B*, **2004**, 108, 14477-14483.
37. Jakub, Z.; Hulva, J.; Ryan, P. T.; Duncan, D. A.; Payne, D. J.; Bliem, R.; Schmid, M. Adsorbate-induced structural evolution changes the mechanism of CO oxidation on a Rh/Fe₃O₄(001) model catalyst. *Nanoscale*, **2020**, 12, 5866-5875.
38. Van Spronsen, M. A.; Frenken, J. W.; Groot, I. M. Surface science under reaction conditions: CO oxidation on Pt and Pd model catalysts. *Chem. Soc. Rev.* **2017**, 46, 4347-4374.
39. Shaikhutdinov, S.; Heemeier, M.; Hoffmann, J.; Meusel, I.; Richter, B.; Bäumer, M.; Jackson, S. D. Interaction of oxygen with palladium deposited on a thin alumina film. *Surf. Sci.* **2002**, 501, 270-281.

Publications

1. **Shanrong Zou**, Yasuhiro Sugawara and Yan Jun Li. Size Dependence of Charge State of Pd Nanoparticles on the Al₂O₃/NiAl (110) Surface by Kelvin Probe Force Microscopy. *J. Phys. Chem. C*, 124(39), 21641-21645 (2020).
2. **Shanrong Zou**, Yasuhiro Sugawara, and Yan Jun Li. Oxygen-Adsorption-Induced Charge State Change of a Pd Nanocluster on the Al₂O₃/NiAl(110) Surface. *J. Phys. Chem. C*, 125 (1), 446-451 (2021).
3. **Shanrong Zou**, Jiuyan Wei, Qiang Zhu, Hongqian Sang, Yasuhiro Sugawara and Yan Jun Li. Study of CO Molecules on Pd/Al₂O₃/NiAl(110) Surface by Atomic Force Microscopy and Kelvin Probe Force Microscopy. (*submitted*)

Presentations

1. **Shanrong Zou**, Yasuhiro Sugawara and Yan Jun Li. “Influence of electron tunneling in the nucleation and growth behavior of Pd nanoparticles on Al₂O₃/NiAl(110)”,
The 4th international symposium “Elucidation of Property of Next Generation Functional Materials and Surface/Interface”, Osaka, Japan, 12.09-12.10(2019). (Oral)
2. **Shanrong Zou**, Kodai Miyoki, Yasuhiro Sugawara and Yan Jun Li. “Study of surface potential at antiphase domain boundaries on Al₂O₃/NiAl(110) by NC-AFM and KPFM”,
The 80th JSAP Autumn Meeting, Sapporo, Japan, 09.18-09.21 (2019). (Poster)
3. **Shanrong Zou**, Katsuharu Matsumoto, Kodai Miyoki, Yasuhiro Sugawara and Yan Jun Li. “Study of contact potential difference of Pd nanoclusters adsorbed on Al₂O₃/NiAl(110) by NC-AFM and KPFM at RT”,
The 22nd international conference on Non-Contact Atomic Force Microscopy, Regensburg, Germany, 07.29-08.02 (2019). (Poster)
4. **Shanrong Zou**, Kodai Miyoki, Yasuhiro Sugawara and Yan Jun Li. “Study of surface potential at antiphase domain boundaries on Al₂O₃/NiAl(110) by NC-AFM and KPFM”,
The 66th JSAP Spring Meeting, Tokyo, Japan, 03.09-03.12(2019). (Poster)
5. **Shanrong Zou**, Huan Fei Wen, Yoshitaka Naitoh, Yasuhiro Sugawara and Yan Jun Li. “Investigation of CO adsorption mechanism on Pd-Al₂O₃/NiAl(110) surface by NC-AFM and KPFM”,
ACSIN-14 and ICSPM26, Sendai, Japan, 10.21-10.25 (2018). (Poster)
6. **Shanrong Zou**, Yoshitaka Naitoh, Yasuhiro Sugawara and Yan Jun Li. “Investigation of CO oxidation mechanism on Pd-Al₂O₃/NiAl(110) catalysts by NC-AFM and KPFM”,
The 6th Japan-China Symposium on Nanomedicine, Matsue, Japan, 05.26-05.28(2018). (Poster)

Acknowledgment

I would like to thank my supervisor Associate Professor Yan Jun Li. She gave me this opportunity to work on this research in Osaka University. I got to learn a lot from my research about surface science and high vacuum knowledge under the instructions and exceptional support.

I would like to thank Professor Yasuhiro Sugawara for helping me overcome equipment problems in my research and give me advice to improve my presentation. I would like to thank to assistant professor Yoshitaka Naitoh for giving me a valuable advice regarding the experiments in Japan.

I would also like to thank all the doctoral committee members for review and improve my doctoral dissertation.

I'd like to show my appreciation to our lab members of Huan Fei Wen and Quanzhen Zhang, who taught me the knowledge of experimental equipment and gave me lots of help in life in Japan. I also give many thanks to other lab members of Ryo Izumi, Masato Miyazaki, Tatsuya Yamamoto, Zhang Qu, Qiang Zhu, and Jiuyan Wei. I also thank the secretaries of Kyoko Nakagawa and Hinata Yamashita for helping me a lot in the lab life. I would also like to express my thanks to all my friends, who helped me a lot during my study in Japan.

I appreciate my parents and all the families who support me and give selfless love.